# 14. Noble Metals and Noble Metal Alloys

Günther Schlamp



The properties of metallic materials depend sensitively not only on their chemical composition and on the electronic and crystal structure of the phases formed, but also to a large degree on their microstructure, including the kinds and distribution of lattice defects. The phase composition and microstructure of metallic materials are strongly dependent, in turn, on the thermal and mechanical treatments, which are applied under well-controlled conditions to achieve the desired properties.

The noble metals are characterized by their high densities, high melting temperatures, high vapor pressures, high electrical and thermal conductivities, optical reflectivities and catalytic properties. They are comparatively soft and ductile, and their hardness increases in the order Rh < Ir < Ru < Os. Solid solution and dispersion hardening strengthen the alloys, while corrosion resistance against various agents decreases in the order Ir > Ru > Rh > Os > Au > Pt > Pd > Ag. Being key materials in electronics and electrical engineering, the pure elements and their alloys serve as materials to manufacture high-strength, corrosion-resistant, high-temperature, and highly oxidation-resistant structural parts. The platinum group metals silver and gold are effective heterogeneous or homogeneous catalysts for a wide variety of chemical reactions. Traditional applications of noble metals and their alloys are in dentistry and jewelry, as well as in coins and medals.




W. Martienssen, H. Warlimont (Eds.), *Springer Handbook of Materials Data*, https://doi.org/10.1007/978-3-319-69743-7_14

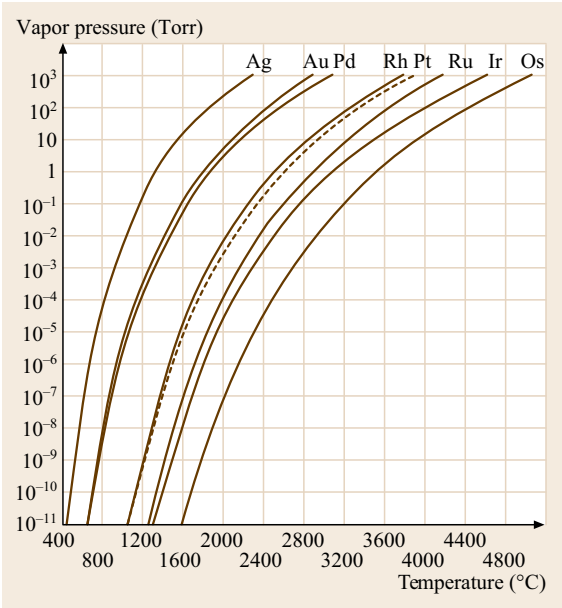


**Fig. 14.1** Vapor pressures of the noble metals (after [14.1])

The noble metals Ag, Au, Pd, Pt, Rh, Ir, Ru, and Os are characterized by their positive reduction potentials against hydrogen, high densities, high melting temperatures, high vapor pressures (Fig. 14.1), high electrical and thermal conductivities, optical reflectivity (Fig. 14.2), and catalytic properties. The electronic density of states (DOS) near the Fermi surface is nearly the same for all noble metals. Individual differences

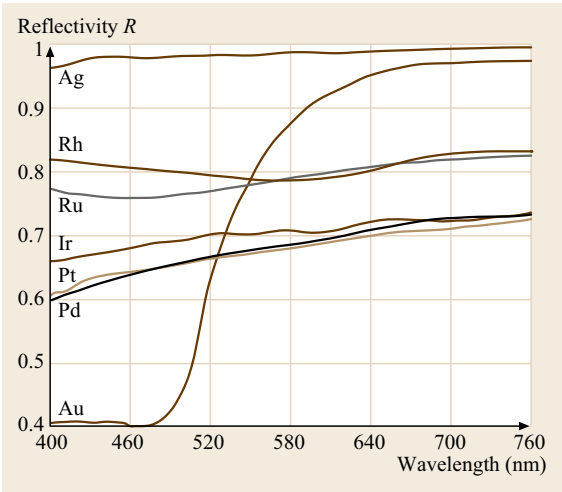


**Fig. 14.2** Optical reflectivity in the visible spectral range (after [14.2])

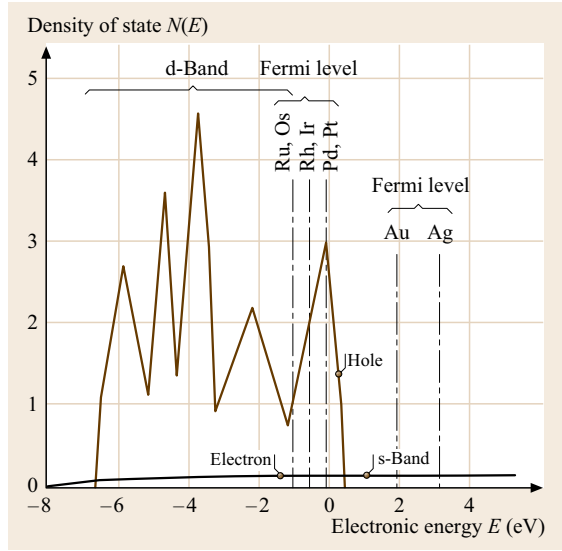


**Fig. 14.3** Schematic DOS curve of the noble metals (after [14.3])

of electrical conductivity, magnetic, and optical behavior are related to different positions of the Fermi level relative to the DOS function (Fig. 14.3). Small energy differences between their outer s and d electronic states result in multiple oxidation states.

Silver, Au, Pd, and Pt are comparatively soft and ductile. Their hardness increases in the order Rh < Ir < Ru < Os. Strengthening of the alloys is affected by solid solution and dispersion hardening. The corrosion resistance against different agents decreases in the order Ir > Ru > Rh > Os > Au > Pt > Pd > Ag.

The purity grades of the elements are standardized according to American Society for Testing and Materials (ASTM) standards from 99.8 to 99.999 wt%: Ag (B 413-69), Au (B 562-86), Pd (B 589-82), Pt (B 561-86), Rh (B 616-78), Ir (B 671-91), and Ru (B 717).

The pure elements and their alloys are key materials in electronics and electrical engineering (Ag, Au, Pd, Pt, and Ru) and serve to manufacture high strength, corrosion-resistant, high temperature, and highly oxidation-resistant structural parts (Pt, Au, Rh, and Ir). The platinum group metals, Ag, and Au in both the metallic state and in the form of chemical compounds are effective heterogeneous or homogeneous catalysts for a wide variety of chemical reactions. Traditional applications of noble metals and their alloys are in dentistry (Au, Pt, Ag, Pd, and Ir), jewelry (Au, Ag, Pt, Pd, Rh, and Ir), and in coins and medals (Au and Ag).

## 14.1 Silver and Silver Alloys

Silver and silver alloys are used for electrical contacts, connecting leads in semiconductor devices, solders and brazes, corrosion-resistant structural parts, batteries, oxidation catalysts, optical and heat reflecting mirrors, table ware, jewelry, dentistry, and coins. Silver halides are base components in photographic emulsions.

### 14.1.1 Production

Silver is extracted from ores through lead melts and precipitation with zinc by the Parkes process. Zinc is removed by distillation, while the remaining lead and base metals are removed by oxidation (cupellation) up to ≈ 99% Ag. True silver ores are extracted by cyanide leaching. High purity grades are produced by electrolysis. Bars, sheets, and wires are produced by classical metallurgical processing, powder by chemical and by electrolytic precipitation from solutions, and nano-crystalline powder grades by dispersion in organic solutions. Coatings and laminate structures are produced by cladding, by electroplating, in thick film layers by applying pastes of silver or in silver alloy powder with organic binder and glass frits onto ceramic surfaces and firing, in thin film coatings by evaporation, and by sputtering composite materials are made by powder technology, or by infiltration of liquid Ag into sintered refractory metals skeletons. Commercial grades of Ag are listed in Table 14.1. Standard purities of crystal powder and bars range from 99.9–99.999% (ASTM B 413-69) [14.2].

### 14.1.2 Phases and Phase Equilibria

Selected phase diagrams are shown in Figs. 14.4–14.9 [14.4, 5]. Silver forms continuous solid solutions with Au and Pd, with miscibility gaps occuring in alloy systems with Mn, Ni, Os, P, and Rh. Data for the solubility of oxygen are given in Table 14.2. Thermodynamic data are given in Tables 14.3–14.6. The entropy of fusion $(L/T)$ of completely disordered intermetallic phases can generally be calculated by fractional addition from those of the components. For the completely ordered state the term $-19.146\,(N_1 \log N_1 + N_2 \log N_2)$ is to be added to the calculated entropy of fusion [14.1–3, 6, 7]. The molar heat capacity of the homogeneous alloy phases and intermetallic compounds, as calculated approximately from the atomic heat capacities of the components using Neumann–Kopps' rule, is obeyed to within ±3% in the temperature range 0–500 °C in the Ag-Au, Ag-Al, Ag-Al, and Ag-Mg alloy systems. The heat capacities of heterogeneous alloys may be calculated by fractional addition from those of the components by the empirical relation $c_p = 4.1816(a + 10^{-3}bT + 10^5 cT^{-2})$ J/(K mol) to satisfactory accuracy.

For compositions and crystal structures, see Tables 14.7–14.9 [14.2, 3, 8, 9]. Primary solid solutions

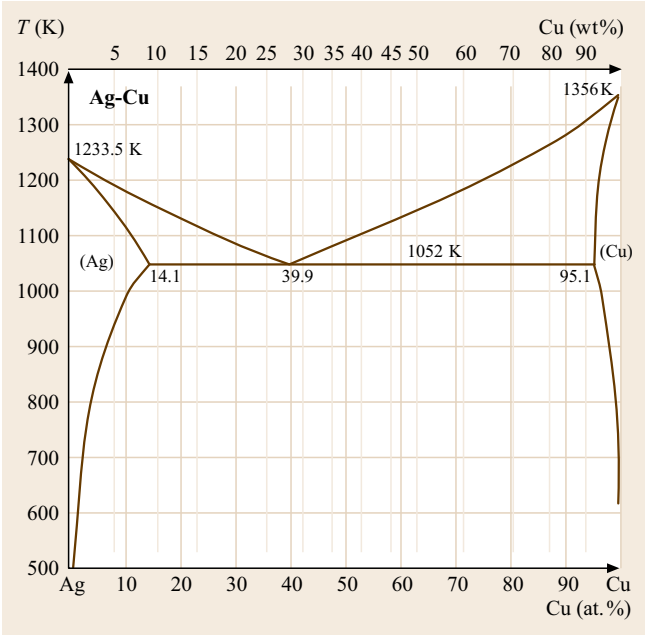


**Fig. 14.4** Binary phase diagram: Ag-Cu (after [14.4])

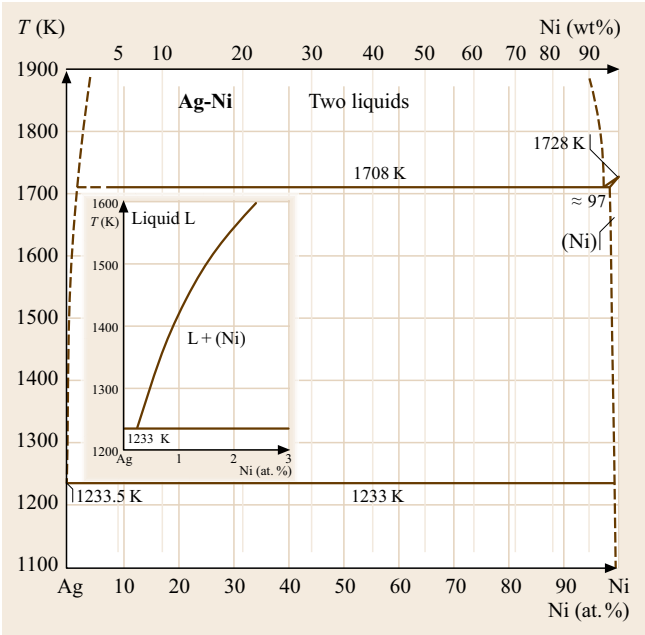


**Fig. 14.5** Binary phase diagram: Ag-Ni (after [14.4])

**Table 14.1** Specifications of fine silver grades (after [14.2])

| Designation | Grade (wt%) | Impurity | Maximum content (ppm) |
|---|---|---|---|
| *Good delivery* | > 99.9 | Any, Cu | 1000 |
| Fine silver | > 99.97 | Cu/Pb/Bi/Se/Te | 300/10/10/5/5 |
| Fine silver 999.9 | > 99.99 | Cu/Pb/Bi/Se/Te | 100/10/10/5/5 |
| Fine silver high pure | < 99.999 | Fe/Pb/Au/Cu/Cd/Bi/Se/Te | 2/1/1/1/0.5/0.5/0.5/0.5/0.5 |

**Table 14.2** Solubility $L$ of oxygen in solid and liquid Ag ($p_{O_2} = 1$ bar) (after [14.1])

| $T$ (°C) | 200 | 400 | 600 | 800 | 973 | 1000 | 1200 |
|---|---|---|---|---|---|---|---|
| $L$ (ppm) | 0.03 | 1.4 | 10.6 | 38.1 | 3050 | 3000 | 2500 |

**Table 14.3** Thermodynamic data of Ag (after [14.2])

| $T$ (K) | $c_p$ (J/(K mol)) | $S$ (J/(K mol)) | $H$ (J/mol) | $G$ (J/mol) | $p$ (at) |
|---|---|---|---|---|---|
| 298.15 | 25.397 | 42.551 | 0 | −12.687 | $1.09 \times 10^{-43}$ |
| 400 | 25.812 | 50.069 | 2.606 | −17.421 | $5.02 \times 10^{-31}$ |
| 800 | 28.279 | 68.661 | 13.392 | −41.537 | $1.45 \times 10^{-12}$ |

$T$ = temperature, $c_p$ = specific heat capacity, $S$ = entropy, $H$ = enthalpy, $G$ = free enthalpy, $p$ = partial pressure of the pure elements

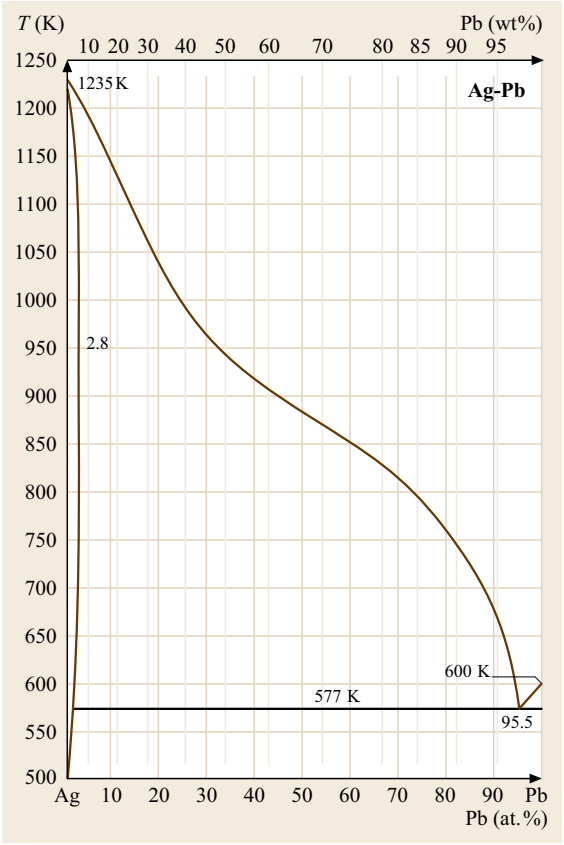


**Fig. 14.6** Binary phase diagram: Ag-Pb (after [14.4])

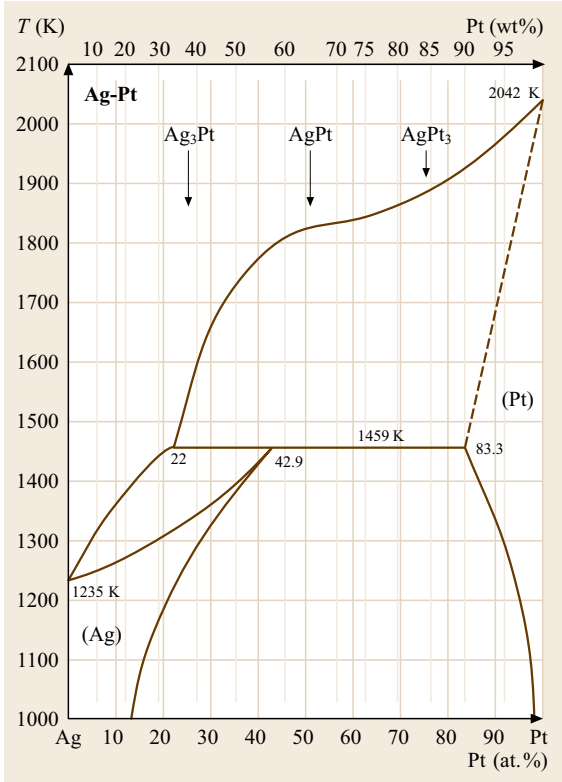


**Fig. 14.7** Binary phase diagram: Ag-Pt (after [14.4])

have the fcc structure of Ag and the lattice parameters correspond roughly to Vegard's rule with a few exceptions. Alloys with Pt, In, Mg, Cd, and Zn form superlattice phases with tetrahedral and rhombohedral symmetry. A characteristic series of structures of intermetallic phases are formed with B-metals at compositions corresponding to e/a values (valence electrons per atom) of 3/2, 21/13, and 7/4 (Hume-Rothery phases) [14.10].

**Table 14.4** Molar heat capacities of solid Ag and Au, $c_p = 4.1868\,(a + 10^{-3}bT + 10^{-5}cT^{-2})$ J/K (after [14.7])

| Element | *a* | *b* | *c* | Temperature range (K) |
|---|---|---|---|---|
| Ag | 5.09 | 2.04 | 0.36 | 298–mp[a] |
| Au | 5.66 | 1.24 | – | 298–mp[a] |

[a] mp = melting point

**Table 14.5** Latent heat and temperatures of transition of Ag and Au intermediate compounds (after [14.7])

| Phase | $N_2$ | Transition | $T_t$ (°C) | $L_t$ (kJ/g-at.) |
|---|---|---|---|---|
| $\beta$-AgCd | 50 | $\beta' \rightarrow \beta$ | 211 | 712 |
| AgZn | 50 | Order–disorder | 258 | 2449 |
| AuCu | 50 | Order–disorder | 408 | 1779 |
| $AuCu_3$ | 75 | Order–disorder | 390 | 1214 |
| $AuSb_2$ | 66.7 | $\beta \rightarrow \gamma$ | 355 | 335 |

$T_t$ = Transition temperature, $L_t$ = latent heat of transition, $N_2$ = mole fraction of the second component

**Table 14.6** Latent heat and temperatures of fusion of Ag and Au intermediate compounds (after [14.7])

| Phase | $N_2$ | $T_m$ (°C) | $L_m$ (kJ/g-at.) |
|---|---|---|---|
| $\delta$-AgCd | 67.5 | 592 | 8.46 |
| $\gamma$-AgZn | 61.8 | 664 | 7.79 |
| $\delta$-AgZn | 72.1 | 632 | 8.75 |
| AuCd | 50.0 | 627 | 8.96 |
| AuSn | 50.0 | 418 | 12.81 |
| $\beta$-AuZn | 50.0 | 760 | 12.31 |

$N_2$ = mole fraction of the second component, $T_m$ = melting point, $L_m$ = latent heat of fusion

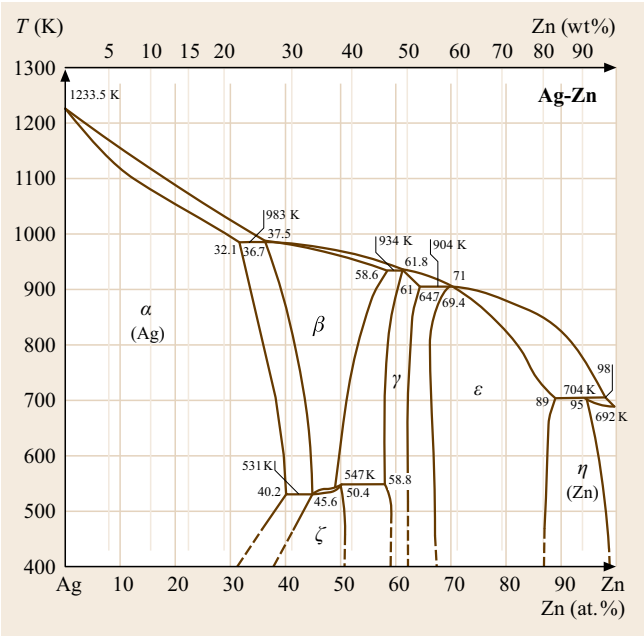


**Fig. 14.8** Binary phase diagram: Ag-Zn (after [14.4])

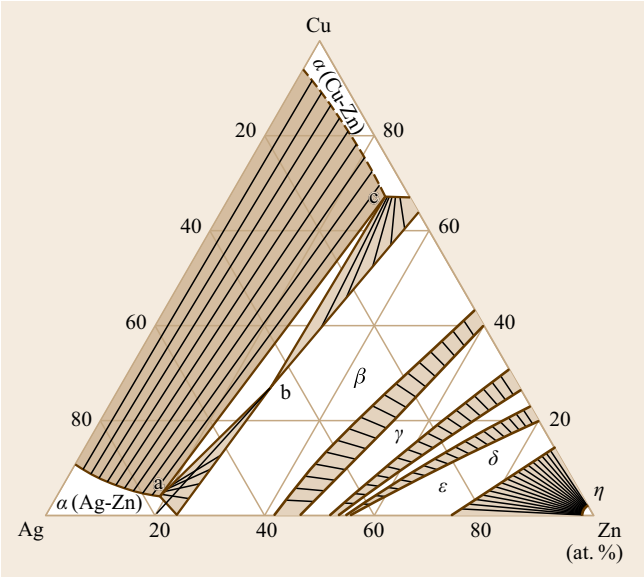


**Fig. 14.9** Ternary phase diagram: Ag-Cu-Zn (after [14.5])

**Table 14.7** Structure and lattice parameter of intermediate Ag compounds (after [14.2])

| Phase | Pearson symbol | *a* (nm) | *b* (nm) | *c* (nm) | *c*/*a* | Remarks | Concentration *x*: $A_{1-x}B_x$ |
|---|---|---|---|---|---|---|---|
| Ag-Al | *cF*4 | 0.4064 | | | | | 0.18 |
| $Ag_2Al$ | *hP*2 | 0.28777 | | 0.46223 | 1.6062 | | |
| Ag-Cd | *hP*2 | 0.2987 | | 0.553 | 1.8514 | | 0.97 |
| AgCd | *cP*2 | 0.3332 | | | | 293 K | 0.5 |
| AgCd | *hP*2 | 0.3016 | | 0.4863 | 1.6124 | 673 K | 0.5 |
| Ag-Cu | *cF*4 | 0.3603 | | | | | 0.95 |
| Ag-Mg | *cF*4 | 0.4116 | | | | | 0.26 |
| Ag-Mg | *hP*2 | 0.3197 | | 0.51838 | 1.6215 | | 0.98 |
| AgO | *cF*8 | 0.4816 | | | | | |
| AgO | *mP*8 | 0.5852 | 0.3478 | 0.5495 | | | |
| Ag-O | *cP*6 | 0.4728 | | | | | |
| Ag-O | *hP*3 | 0.3072 | | 0.4941 | 1.6084 | HP/HT | |
| Ag-Zn | *hP*2 | 0.28227 | | 0.44274 | 1.5685 | | 0.775 |
| Ag-Zn | *hP*9 | 0.7636 | | 0.28179 | 0.369 | | 0.38−0.52 |

HT = high-temperature modification, HP = high-pressure modification

**Table 14.8** Composition and structures of superlattices in noble metal alloy systems (after [14.3])

| Atomic ratio | Composition | | | | Superlattice structure | Fundamental structure |
|---|---|---|---|---|---|---|
| 3 : 1 or 1 : 3 | $Pd_3Fe$ | $PdCu_3$ | $Au_3Cu$ | $AuCu_3$ | | |
| | $Pt_3Fe$ | $PtCu_3$ | $Au_3Pd$ | | | |
| | $Pt_3Ti$ | $PtNi_3$ | $Ag_3Pt$ | | $L1_2$ | fcc |
| | | $PtMn_3$ | | | | |
| | $Rh_3Mo$ | | $Ag_3In$ | | | |
| | $Rh_3W$ | | | | $DO_{14}$ | |
| | $Ir_3Mo$ | | | | | |
| | $Ir_2W$ | | $(Au_2Mn)$ | | $DO_{22}$ | fcc |
| | $Pd_3V$ | | | | | |
| | $Pd_3Nb$ | | | | | |
| | $Pt_3V$ | | | | | |
| | | | $Au_3Cd$ | | $DO_{23}$ | fcc |
| | | | $Au_3Zn$ | | | |
| | | | $Ag_3Mg$ | | | |
| 2 : 1 | $Pd_2V$ | | | | $Ni_2Cr$ | fcc |
| | $Pt_2V$ | | | | | |
| | $Pt_2Mo$ | | | | | |
| 1 : 1 | PdFe | | AuCu | | | |
| | PtFe | | | | $L1_0$ | fcc |
| | PtV | | | | | |
| | PtNi | | | | | |
| | PtCo | | | | | |
| | PtCu | | | | | fcc |
| | PdCu | | AuMn | | $L1_1$ | bcc |
| | | | AgCd | | $L2_0$ or B2 | |
| | | | AgZn | | | |
| | RhMo | | | | | hcp |
| | IrMo | | | | B19 | |
| | PtMo | | | | | |
| | IrW | | | | | |
| | PtNb | | | | | |

**Table 14.9** Compositions and structures of e/a (Hume-Rothery) compounds (after [14.10])

| Electron : atom ratio = 3 : 2 | | | Electron : atom ratio = 21 : 13 | Electron : atom ratio = 7 : 4 |
|---|---|---|---|---|
| Body-centered cubic structure | Complex cubic ($\beta$-manganese) structure | Close-packed hexagonal structure | $\gamma$-Brass structure | Close packed hexagonal structure |
| AgMg | AgHg | AgZn | $Ag_5Zn_8$ | $AgZn_3$ |
| AgZn | $Ag_3Al$ | AgCd | $Ag_5Cd_8$ | $AgCd_3$ |
| AgCd | $Au_3Al$ | $Ag_3Al$ | $Ag_5Hg_8$ | $Ag_3Sn$ |
| $Ag_3Al$ | | $Ag_3Ga$ | $Ag_9In_4$ | $Ag_5Al_3$ |
| $Ag_3In$ | | $Ag_3In$ | $Au_3Zn_8$ | $AuZn_3$ |
| AuMg | | $Ag_5Sn$ | $Au_5Cd_8$ | $AuCd_3$ |
| AuZn | | $Ag_7Sb$ | $Au_9In_4$ | $Au_3Sn$ |
| AuCd | | $Au_3In$ | $Rh_5Zn_{21}$ | $Au_5Al_3$ |
| | | $Au_5Sn$ | $Pd_5Zn_{21}$ | |
| | | | $Pt_5Be_{21}$ | |
| | | | $Pt_5Zn_{21}$ | |

### 14.1.3 Mechanical Properties

In Tables 14.10–14.20 and Figs. 14.10–14.15 characteristic data are shown [14.2, 5, 10–14]. References for data of elastic constants of Ag alloys are given in [14.7]. Pure silver is very soft. Strengthening is affected by solid solution and by dispersion hardening [14.1, 15]. Alloying with 0.15 wt% Ni affects grain refinement and stabilizes against recrystallization. The high solubility of oxygen in silver (Table 14.2) permits the inducement of dispersion hardening by internal oxidation of Ag alloys containing Al, Cd, Sn, and/or Zr.

**Table 14.10** Modulus of elasticity of Ag in crystal directions (in GPa) (after [14.2])

| $E$ ⟨100⟩ | $E$ ⟨110⟩ | $E$ ⟨111⟩ |
|---|---|---|
| 44 | 82 | 115 |

**Table 14.11** Elastic constants of Ag (in GPa) (after [14.2])

| $T$ (°C) | $c_{11}$ | $c_{12}$ | $c_{14}$ |
|---|---|---|---|
| −273 | 131.4 | 97.3 | 51.1 |
| +20 | 124.0 | 93.4 | 46.1 |

**Table 14.13** Tensile strength $R_m$ of binary Ag alloys (after [14.2])

| Alloying elements | $R_m$ (MPa) | | | |
|---|---|---|---|---|
| | 2 wt% | 5 wt% | 10 wt% | 20 wt% |
| Au | 160 | 170 | 180 | 200 |
| Cd | 160 | 170 | 180 | 210 |
| Cu | 190 | 240 | 280 | 310 |
| Pd | 160 | 180 | 21 | |
| Sb | 190 | 240 | 300 | |
| Sn | 190 | 240 | 300 | |

**Table 14.14** Hardness of Ag-Mn alloys (after [14.11])

| MN (wt%) | 0.5 | 4.9 | 6.2 | 12.0 |
|---|---|---|---|---|
| HV (kg/mm$^2$) | 31 | 39 | 40 | 58 |

**Table 14.12** Mechanical properties of Ag (99.97%) at different temperatures (after [14.2])

| $T$ (°C) | $E$ (GPa) | $R_m$ (MPa) | $A$ (%) | $R_{p0.2}$ (MPa) | HV |
|---|---|---|---|---|---|
| 20 | 82 | 150 | 50 | 28 | 26 |
| 200 | 77 | 130 | – | 25 | 22 |
| 400 | 67 | 100 | 30 | 20 | 17 |
| 800 | 46 | 35 | – | 17 | 5 |

$A$ = elongation, $E$ = modulus of elasticity, $R_p$ = limit of proportionality, HV= Vickers hardness, $R_m$ = tensile strength

**Table 14.15** Mechanical properties of Ag-Cu-P alloys (after [14.11])

| Composition (wt%) | | | BS 1845[a] | Density (g/cm$^3$) | Melting range (°C) | Tensile strength (kg/mm$^2$) | Elongation (%) |
|---|---|---|---|---|---|---|---|
| Ag | Cu | P | | | | | |
| 15 | 80 | 5 | CP1 | 8.40 | 645–719 | 25 | 10 |
| 5 | 89 | 6 | CP4 | 8.20 | 645–750 | 25 | 5 |
| 2 | 91 | 7 | CP3 | 8.15 | 645–770 | 25 | 5 |

[a] British standard (1966–1971) designation

**Table 14.16** Mechanical properties of Ag-Cu-Zn alloys (after [14.5])

| Composition (wt%) | | | Specific weight | Tensile strength | Elongation | Electrical conductivity |
|---|---|---|---|---|---|---|
| Cu | Zn | Ag | (cast) | ($kg/mm^2$) | (%) | (% of Cu) |
| 36 | 24 | 40 | 9.11 | 40.5 | 6.2 | 19.7 |
| 25 | 15 | 60 | 9.52 | 45.0 | 7.7 | 20.5 |
| 22 | 3.0 | 75 | 10.35 | 29.3 | 5.3 | 53.4 |
| 16 | 4.0 | 80 | 10.05 | 35.1 | 16.0 | 45.8 |

**Table 14.17** Mechanical properties of Ag-Pd alloys in annealed (s) and hard (h) condition (after [14.2])

| Alloy Ag-X | HV 5 | | $R_{p0.2}$ (MPa) | | $R_{on}$ (MPa) | | $A$ (%) | |
|---|---|---|---|---|---|---|---|---|
| (wt%) | s | h | s | h | s | h | s | h |
| Pd27.5 | 55 | | 80 | | 230 | | 33 | |
| Pd27.4Cu10.5 | 140 | 310 | 320 | 940 | 510 | 950 | 31 | 3 |
| Pd39.9Zn4 | 160 | 270 | 285 | 595 | 560 | 790 | 18 | 6 |

s = soft, h = hard

**Table 14.18** Tensile strength $R_m$ and elongation $A$ of Ag alloys at different temperatures (after [14.2])

| Alloy Ag-X | $R_m$ (MPA)/$A$ (%) | | | | |
|---|---|---|---|---|---|
| (wt%) | 20 °C | 200 °C | 400 °C | 600 °C | 800 °C |
| Cd4 | 170/60 | 150/50 | – | – | – |
| Cd8 | 480/5 | 260/20 | 200/55 | – | – |
| Cu3 | 190/35 | 170/40 | 140/40 | 90/80 | 30/150 |
| Cu7.5 | 250/46 | 220/48 | 180/47 | 120/55 | 60/78 |
| Ni0.3 | 190/60 | 170/60 | 130/65 | 100/65 | 60/50 |
| Si3 | 260/39 | 220/33 | 180/35 | 90/52 | 20/55 |

**Table 14.19** Strengthening of Ag (99.975%) by cold forming as a function of reduction in cross section $V$ (after [14.2])

| $V$ (%) | $R_m$ (MPa) | $A$ (%) | HV |
|---|---|---|---|
| 0 | 150 | 50 | 26 |
| 10 | 180 | 30 | 54 |
| 30 | 260 | 5 | 70 |

**Table 14.20** Strengthening of Ag alloys by cold forming (HV 10) (after [14.2])

| Alloy Ag-X | Reduction in thickness (%) | | |
|---|---|---|---|
| (wt%) | 0 | 40 | 80 |
| Cu | 58 | 108 | 134 |
| Cu15 | 76 | 126 | 158 |
| Cu28 | 98 | 136 | 177 |
| Cu50 | 84 | 130 | 166 |
| Ni0.15 | 40 | 86 | 100 |
| Pd30 | 70 | 132 | 164 |
| Pd30Cu5 | 92 | 174 | 2165 |

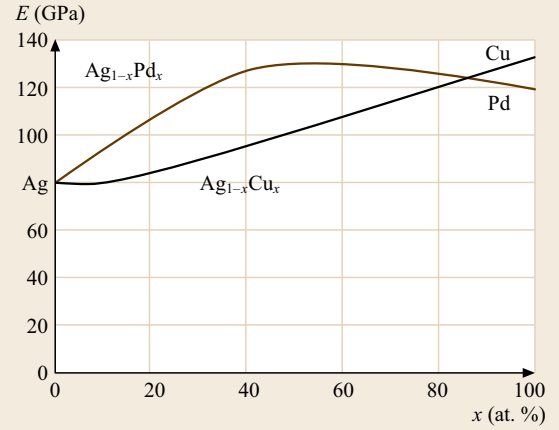


**Fig. 14.10** Modulus of elasticity $E$ of Ag-Pd and Ag-Cu alloys (after [14.2])

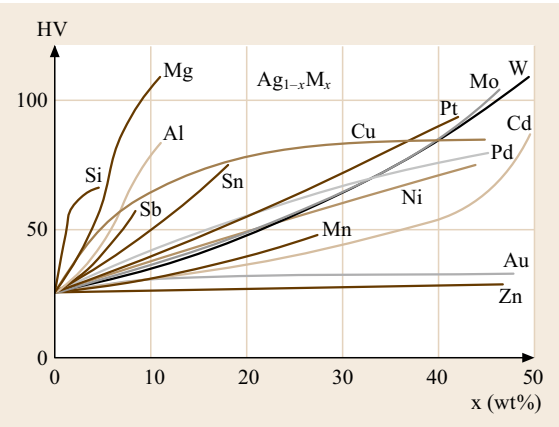


**Fig. 14.11** Influence of alloying elements on the hardness of binary Ag alloys $A_{1-x}M_x$ (after [14.2])

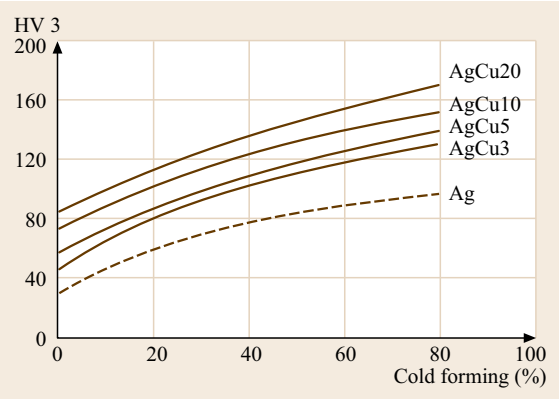


**Fig. 14.12** Hardening of Ag-Cu alloys by cold forming (after [14.2]) ◄

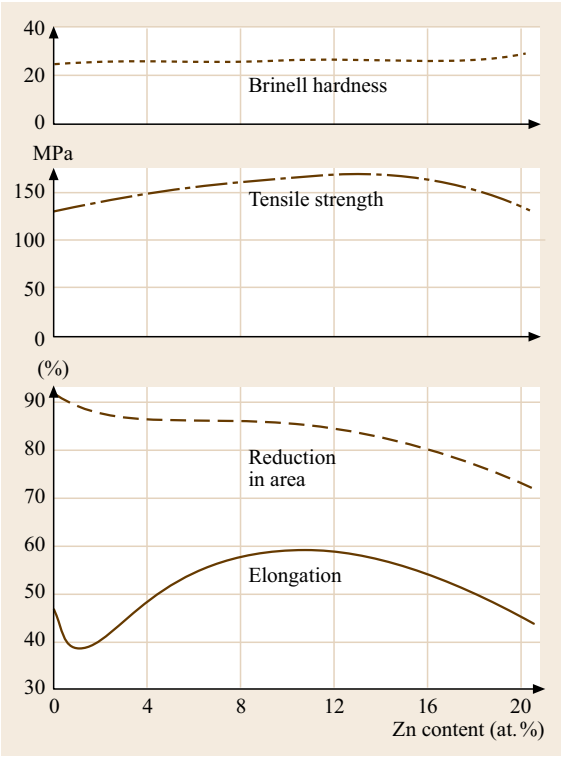


**Fig. 14.13** Plastic properties of Ag-Zn crystals (after [14.5])

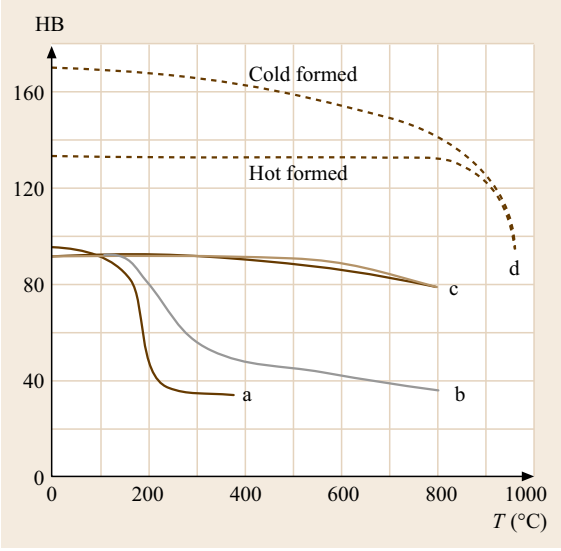


**Fig. 14.14** Hardness of fine grain and dispersion-hardened Ag (after [14.1])

### 14.1.4 Electrical Properties

Tables 14.21–14.24 and Fig. 14.16 [14.2, 16–18] show characteristic data. The residual resistivity ratio (RRR) of pure Ag ranges up to 2100. Ag alloys with Pb and Sn show superconductivity in the composition ranges: $Ag_{0.95-0.66}Pb_{0.05-0.34}$ with $T_c = 6.6-7.3$ K and $Ag_{0.72-0.52}Sn_{0.28-0.48}$ with $T_c = 3.5-3.65$ K [14.19].

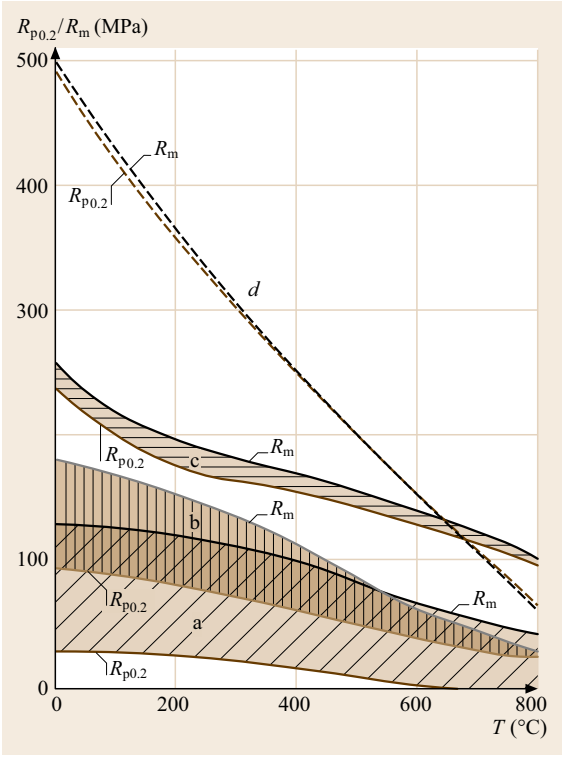


**Fig. 14.15** Tensile strength and 0.2% proof stress of silver grades at different temperatures (after [14.1])

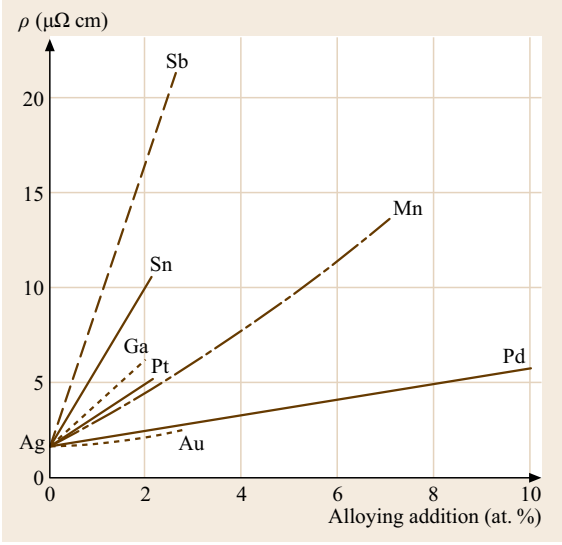


**Fig. 14.16** Influence of alloying elements on the electrical conductivity of binary Ag alloys (after [14.16])

**Table 14.21** Specific electrical resistivity $\rho(T) = \rho_0 + \rho_i(T)$ of Ag ($\rho_0 = 0.0008\,\mu\Omega$ cm) at different temperatures (after [14.2])

| $T$ (K) | $\rho(T)$ ($\mu\Omega$ cm) |
|---|---|
| 10 | 0.0001 |
| 50 | 0.1032 |
| 120 | 0.5448 |
| 273 | 1.470 |
| 500 | 2.860 |
| 700 | 4.172 |
| 900 | 5.562 |
| 1100 | 7.031 |

**Table 14.22** Increase of atomic electrical resistivity of Ag by alloying elements (after [14.2])

| Base element | $\Delta\rho/C$ ($\mu\Omega$ cm/at.%) |
|---|---|
| Ag | Al 1.87, As 8, Au 0.36, Cd 0.35, Cr 6.5, Cu 0.07, Fe 3.2, Ga 2.3, Ge 5, Hg 0.8, In 1.6, Pb 4.6, Pd 0.44, Pt 1.5, Sn 4.5, Zn 0.63 |

**Table 14.23** Specific electrical resistivity $\rho_i$ ($\mu\Omega$ cm) and coefficient of electrical resistivity (TCR) ($10^{-3}$ K$^{-1}$) of noble metal solid solution alloy phases (after [14.2])

| Base/solute-metal | Property | Solute content (at.%) | | | |
|---|---|---|---|---|---|
| | | 20 | 40 | 60 | 80 |
| Rh/Ni | $\rho_i$ | 21 | 37 | 51 | 50 |
| | TCR | 3.8 | 1.8 | < 0.1 | 3 |
| Ag/Au | $\rho_i$ | 8.3 | 11.0 | 11.0 | 8.1 |
| | TCR | 0.93 | 0.83 | 0.84 | 1.1 |
| Ag/Pd | $\rho_i$ | 11 | 22 | 41 | 34 |
| | TCR | 0.58 | 0.40 | – | 0.75 |
| Ag/Pt | $\rho_i$ | 33 | 60 | 46 | 35 |
| Au/Pd | $\rho_i$ | 9.8 | 17 | 30 | 26 |
| | TCR | 0.88 | 0.61 | 0.45 | 1.2 |
| Au/Pt | $\rho_i$ | 28 | 44 | 0.82 | 0.8 |
| | TCR | 0.28 | 0.26 | 0.82 | 0.8 |

**Table 14.24** Specific electrical resistivity $\rho_{25}$ of annealed (8 h at 550 °C) Ag-Cu wire at 25 and 100 °C ($\rho_{100}$) and temperature coefficient of resistivity (TCR) for 25–100 °C (after [14.11])

| Property | Ag content (at.%) | | | | |
|---|---|---|---|---|---|
| | 5 | 15 | 45 | 75 | 96 |
| $\rho_{25}$ ($10^{-6}$ $\mu\Omega$ cm) | 1.832 | 1.895 | 1.913 | 1.645 | 1.822 |
| $\rho_{100}$ ($10^{-6}$ $\mu\Omega$ cm) | 2.369 | 2.320 | 2.411 | 2.308 | 2.297 |
| TCR $\times 10^5$ (K$^{-1}$) | 389 | 387 | 380 | 365 | 381 |

**Table 14.25** Thermal electromotive force $E_{Ag,Pt}$ of Ag at different temperatures; reference junction at 0 °C (after [14.2])

| $T$ (°C) | −200 | −100 | −50 | +100 | +200 | +400 | +800 |
|---|---|---|---|---|---|---|---|
| $E_{Ag,Pt}$ (mV) | −0.39 | −0.21 | −0.10 | 0.74 | 1.77 | 4.57 | 13.36 |

**Table 14.26** Absolute thermoelectric power of Ag at different temperatures (after [14.1])

| Temperature (°C) | −255 | −200 | −100 | −20 | 0 | 100 | 300 | 500 | 800 |
|---|---|---|---|---|---|---|---|---|---|
| Thermoelectric power (μV/°C) | +0.62 | +0.82 | +1.00 | – | +1.4 | +1.9 | +3.0 | 4.6 | +8.3 |

## 14.1.5 Thermoelectric Properties

In Tables 14.25–14.27 and Fig. 14.17, characteristic data are shown: absolute thermoelectric power, thermoelectromotive force of pure Ag as well as Ag-Au, Ag-Pd, and Ag-Pt alloys at different temperatures against a reference junction at 0 °C [14.2, 20, 21].

## 14.1.6 Magnetic Properties

Silver is diamagnetic (Table 14.28). The magnetic susceptibility remains constant from 0 K to the melting point. Alloying with B metals causes only minor variations compared to pure Ag. In the continuous solid solution range the molar susceptibilities remain negative and the alloys are diamagnetic. Ni, Pd, and Pt dissolve up to 25 at.% diamagnetically. Cr, Fe, and Mn give rise to paramagnetism, while Co causes ferromagnetism [14.1, 2].

**Table 14.27** Thermal electromotive force of Ag-Au alloys in mV at 100 and 700 °C reference junction at 0 °C (after [14.2])

| $T$ (°C) | Composition (wt%) 0 | 20 | 40 | 60 | 80 | 100 |
|---|---|---|---|---|---|---|
| 100 | 0.74 | 0.47 | 0.42 | 0.42 | 0.49 | 0.78 |
| 700 | 10.75 | 7.7 | 6.7 | 6.8 | 7.3 | 10.15 |

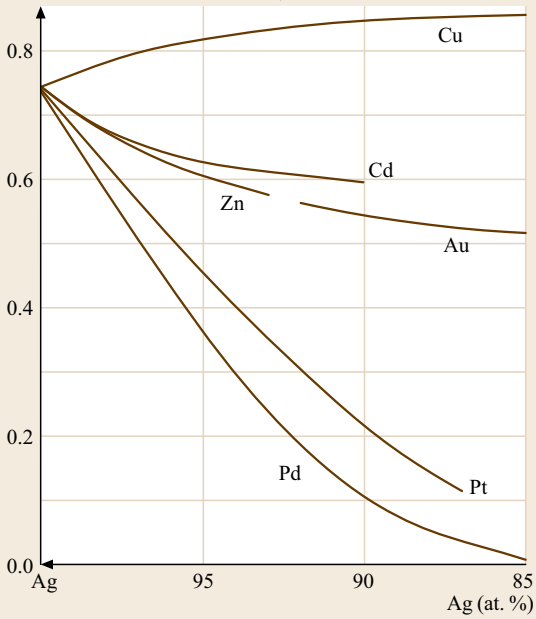


## 14.1.7 Thermal Properties

Selected data of thermal expansion, thermal conductivity, and melting temperatures of Ag alloys are given in Tables 14.29–14.35 and in Fig. 14.18 [14.1, 5].

**Table 14.28** Atom susceptibility of Ag and Au binary alloys at room temperature (after [14.1])

| Base metal | Alloying element | Base metal content (at.%) 100 | 99 | 95 | 90 | 80 |
|---|---|---|---|---|---|---|
| Ag | Au | −19 | | −20.2 | −20.8 | −22.2 |
| | Pd | −20 | | | −21 | −22 |
| Au | Cu | −26 | | −25.2 | −24.2 | −22.4 |
| | Ni | −28 | −22 | ±0 | +16 | – |
| | Pd | −28 | | | −20 | −15 |
| | Pt | −28 | | | −6 | ±0 |

**Table 14.29** Recrystallization temperatures of Ag 99.95 and 99.995% purity after different degrees of deformation $V$; annealing time 1 h (after [14.2])

| $V$ (%) | $T_{recryst.}$ (°C) Purity 99.95% | Purity 99.995% |
|---|---|---|
| 40 | 190 | 125 |
| 60 | 160 | 100 |
| 99 | 127 | 70 |

**Table 14.30** Mean coefficients of thermal expansion $\alpha$ of Ag and Au (after [14.2])

| $T$ (K) | $\alpha$ ($10^{-6}$ $K^{-1}$) Ag | Au |
|---|---|---|
| 373 | 17.9 | 13.9 |
| 473 | 19.1 | 14.8 |
| 673 | 19.9 | 15.3 |
| 873 | 21.1 | 15.7 |
| 1073 | 23.6 | 16.2 |

**Fig. 14.17** Thermal electromotive force of binary Ag alloys (after [14.1]) ◄

**Table 14.31** Mean coefficients of thermal expansion $\alpha$ ($10^{-6}$ $K^{-1}$) of Ag and Au alloys (after [14.2])

| Base metal<br>Second metal | Au<br>Ag | Au<br>Ag | Au<br>Cu | Au<br>Ni | Ag<br>Pd |
|---|---|---|---|---|---|
| Temp. range (K) | 273–373 | 293–1073 | 273–593 | 273–373 | 373–473 |
| **Second metal (wt%)** | **$\alpha$ ($10^{-6}$ $K^{-1}$)** | | | | |
| 20 | 15.5 | 17.0 | 14.9 | 14.4 | 16.2 |
| 40 | 16.5 | 18.7 | – | 13.9 | – |
| 50 | 17.0 | – | 15.7 | 14.0 | 14.7 |
| 60 | 17.5 | 20.1 | 15.8 | 13.9 | – |
| 80 | 18.2 | 20.8 | 15.9 | 13.4 | 12.4 |

**Table 14.32** Specific heat of Ag at different temperatures (after [14.5])

| $T$ (°C) | −259.46 | −240.86 | −141.93 | −67.90 | +98.7 | +249.0 | +399.5 | +652.2 |
|---|---|---|---|---|---|---|---|---|
| $c_p$ (cal/g) | 0.001177 | 0.01259 | 0.04910 | 0.05334 | 0.0569 | 0.0583 | 0.0600 | 0.0635 |

**Table 14.33** Vapor pressure of liquid Ag (after [14.5])

| $T$ (°C) | 1550 | 1611 | 1742 | 1838 | 1944 | 2152 |
|---|---|---|---|---|---|---|
| Vapor pressure (mm Hg) | 8.5 | 15.7 | 54 | 100 | 190 | 760 (extrapol.) |

**Table 14.34** Thermal conductivity $\lambda$ of Ag and Au at different temperatures (after [14.2])

| $T$<br>(K) | $\lambda$ (W/(m K))<br>Ag | Au |
|---|---|---|
| 40 | 1050 | 420 |
| 100 | 475 | 360 |
| 273 | 435 | 318 |
| 600 | 411 | 296 |
| 800 | 397 | 284 |

**Table 14.35** Melting range of Ag-Cu-Sn and Ag-Cu-In solder alloys

| Composition (wt%) | | | | Melting range |
|---|---|---|---|---|
| Ag | Cu | Sn | In | (°C) |
| 60 | 23 | 17 | | 557–592 |
| 50 | 30 | 20 | | 555–578 |
| 47 | 20 | 33 | | 472–515 |
| 50 | 10 | 40 | | 435–456 |
| 49 | 19 | | 32 | 549–556 |
| 50 | 25 | | 25 | 594–601 |
| 45 | 17 | | 38 | 534–548 |
| 25 | 45 | | 30 | 581–610 |

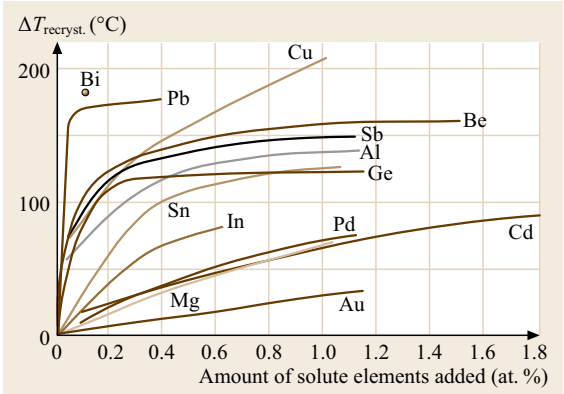


**Fig. 14.18** Increase of the recrystallization temperature of Ag by solute elements (after [14.3])

**Table 14.36** Spectral emissivity of Ag and Au at different temperatures (after [14.2])

| Element | Surface | Temperature (°C) | Spectral degree of emission |
|---|---|---|---|
| Ag | Solid | 940 | 0.044 |
| | Liquid | 1060 | 0.0722 |
| Au | Solid | 1000 | 0.154 |
| | Liquid | 1067 | 0.222 |

## 14.1.8 Optical Properties

Table 14.36 and Figs. 14.19 and 14.20 [14.22] show characteristic data of optical properties. Ag has the highest reflectivity of all noble metals. An interband transition takes place in the ultraviolet range at 3.9 eV. Ag-Al alloys between 10 and 28 at.% Ag show higher reflectance in the low wavelength range than the pure elements. In Ag-Pd alloys, the threshold energy at 3.9 eV for the interband transition remains constant up to ≈ 34 at.% Pd. Examples of colored Ag alloys are given in Table 14.37 [14.22].

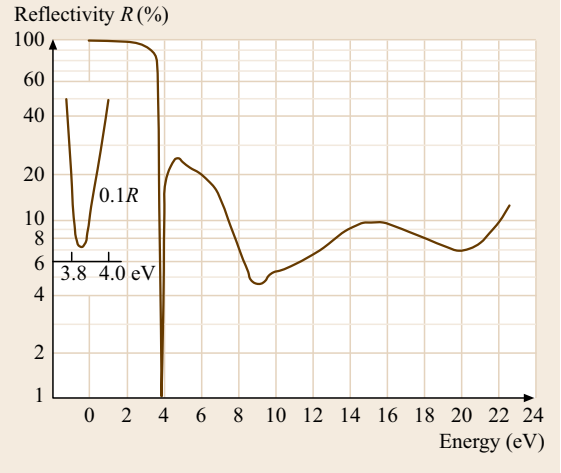


**Fig. 14.19** Reflectivity versus radiation energy of Ag (after [14.22])

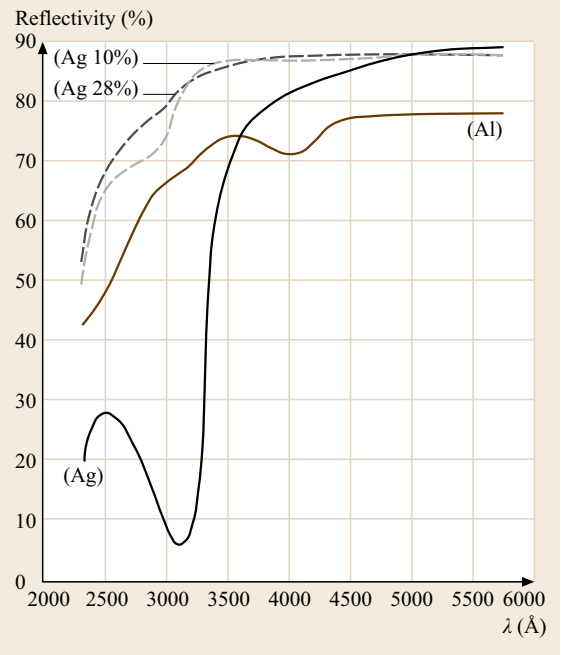


**Fig. 14.20** Reflectivity of Ag-Al alloys (after [14.5])

### 14.1.9 Diffusion

Data for self-diffusion of Ag in Ag alloys and diffusion of tracer impurity elements are shown in Tables 14.38–14.43 and Figs. 14.21–14.23. Diffusion of H and O is of importance for annealing treatments and dispersion hardening [14.2, 5, 11, 20].

**Table 14.37** Colored noble metal alloys (after [14.22])

| Alloy | Color | Remarks |
|---|---|---|
| Ag-Zn ($\beta$-phase) | Rose | |
| Ag-Au(70) | Green-yellow | |
| $Al_2Au$ | Violet | |
| $KAu_2$ | Violet | |
| Au-Zn-Cu-Ag | Green | |
| $AuIn_2$ | Blue | |
| **Zintl phases** | | |
| $Li_2AgAl$ | Yellow-rose | VEC 1.5 |
| $Li_2AgGa$ | Yellowish | VEC 1.5 |
| $Li_2AgIn$ | Gold-yellow | VEC 1.5 |
| $Li_2AgTl$ | Violet-rose | VEC 1.5 |
| $Li_2AuTl$ | Green-yellow | VEC 1.5 |
| $Li_2AgSi$ | Rose-violet | VEC 1.75 |
| $Li_2AgGe$ | Rose-violet | VEC 1.75 |
| $Li_2AgSn$ | Violet | VEC 1.75 |
| $Li_2AgPb$ | Blue-violet | VEC 1.75 |
| $Li_2AuPb$ | Violet | VEC 1.75 |

VEC = valence electron concentration

**Table 14.38** Self-diffusion in binary homogeneous Ag-Au alloys (after [14.2])

| Ag-Au ($^{110m}$Ag diffusion) | | | |
|---|---|---|---|
| **Au (at.%)** | **$\Delta T$ (K)** | **$D^0$ ($10^4$ m$^2$/s)** | **$Q$ (kJ/mol)** |
| 8 | 927–1218 | 0.52 | 187.5 |
| 17 | 908–1225 | 0.32 | 184.4 |
| 83 | 923–1284 | 0.09 | 171.7 |
| 94 | 936–1234 | 0.072 | 168.5 |
| **Ag-Au ($^{198}$Au diffusion)** | | | |
| **Au (at.%)** | **$\Delta T$ (K)** | **$D^0$ ($10^4$ m$^2$/s)** | **$Q$ (kJ/mol)** |
| 8 | 991–1213 | 0.82 | 202.2 |
| 17 | 991–1220 | 0.48 | 198.0 |
| 83 | 985–1274 | 0.12 | 180.2 |
| 94 | 991–1283 | 0.09 | 176.1 |

**Table 14.39** Self-diffusion in pure Ag and Au (frequency factor $D^0$ ($10^{-4}$ m$^2$/s)), activation energy $Q$ (kJ/mol) (after [14.2])

| | Element | $D^0$ (m$^2$/s) | $Q$ (kJ/mol) | $T$ (K) |
|---|---|---|---|---|
| Lattice | Ag | 0.278 | 181.7 | 1038–1218 |
| | Ag(s)[a] | 0.67 | 190.1 | 913–1221 |
| | Au | 0.107 | 176.9 | 623–733 |
| | Au(s)[a] | 0.027 | 165 | 603–866 |
| Surface | Ag | $1\times10^4$ | 264 | 873–1173 ($H_2$) |
| | Ag | $3\times10^{-5}$ | 49 | 580–730 (Vac.) |
| | Au(110) | $1\times10^2$ | 227 | 1138–1329 ($H_2$) |
| | Au | $8\times10^2$ | 272 | 1200–1300 (Vac.) |
| Grain-boundary | Ag | $7.24\times10^{-5}$ | 190.4 | ≈ 790–680 |
| | Au | $9.10\times10^{-6}$ | 174.6 | 625–521 |

[a] (s) = single crystal

**Table 14.40** Diffusion of Ag in Cu and Cu in Ag (after [14.11])

| | | | | | |
|---|---|---|---|---|---|
| **Ag in Cu** | | | | | |
| $T$ (°C) | 485 | 574 | 625 | 731 | 794 |
| $D_{Ag}$ (cm$^2$/s) | $4.9\times10^{-14}\pm0.1$ | $8.2\times10^{-13}\pm0.6$ | $2.91\times10^{-12}\pm0.08$ | $7.7\times10^{-11}$ | $1.65\times10^{-10}$ |
| $D = D_0\exp(-E_A/(RT))$ with $D_0 = 0.61$ cm$^2$/s, $E_A = 46.5$ kcal/(g atom) | | | | | |
| **Cu in Ag** | | | | | |
| $T$ (°C) | 498 | 597 | 760 | 800 | 895 |
| $D_{Cu}$ (cm$^2$/s) | $2.87\times10^{-13}\pm0.45$ | $5.08\times10^{-12}\pm0.54$ | $3.55\times10^{-10}$ | $5.9\times10^{-10}$ | $9.4\times10^{-10}$ |
| $D_0 = 1.23$ cm$^2$/s, $E_A = (46.1\pm0.9)$kcal/(g atom) | | | | | |

**Table 14.41** Diffusion of impurities in Ag, Au, Pt and Pd (after [14.2])

| Tracer | $D^0$ ($10^{-4}$ m$^2$/s) | $Q$ (kJ/mol) | $\Delta T$ (K) |
|---|---|---|---|
| **Matrix: Silver (Ag)** | | | |
| Cu | 1.23 | 193.0 | 990–1218 |
| | 0.029 | 164.1 | 699–897 |
| Au | 0.262 | 190.5 | 923–1223 |
| | 0.41 | 194.3 | 929–1178 |
| | 0.85 | 202.1 | 991–1198 |
| | 0.62 | 199.0 | |
| Pd | 9.57 | 237.6 | 1009–1212 |
| Pt | 6.0 | 238.2 | 923–1223 |
| | 1.9 | 235.7 | 1094–1232 |
| Ru | 180 | 275.5 | 1066–1219 |
| **Matrix: Gold (Au)** | | | |
| Pd | 0.076 | 195.1 | 973–1273 |
| Pt | 0.095 | 201.4 | 973–1273 |
| Ag | 0.072 | 168.3 | 943–1281 |
| | 0.08 | 169.1 | 1046–1312 |
| | 0.086 | 169.3 | 1004–1323 |
| Hg | 0.116 | 156.5 | 877–1300 |
| **Matrix: Platin (Pt)** | | | |
| Ag | 0.13 | 258.1 | 1473–1873 |
| Au | 0.13 | 252.0 | 850–1265 |
| **Matrix: Palladium (Pd)** | | | |
| Fe | 0.18 | 260 | 1373–1523 |

**Table 14.42** Grain boundary tracer diffusion in pure Ag (after [14.2])

| Matrix | Tracer | $D^0$ ($10^4$ m$^2$/s) | $Q$ (kJ/mol) | $T$ (K) |
|---|---|---|---|---|
| Ag | Cd | 5.04 | 176.6 | 772–557 |
| | In | 5.50 | 174.8 | 764–469 |
| | Sb | 2.34 | 163.5 | 771–471 |
| | Sn | 4.72 | 170.9 | 776–527 |
| | Te | 2.10 | 154.7 | 970–650 |

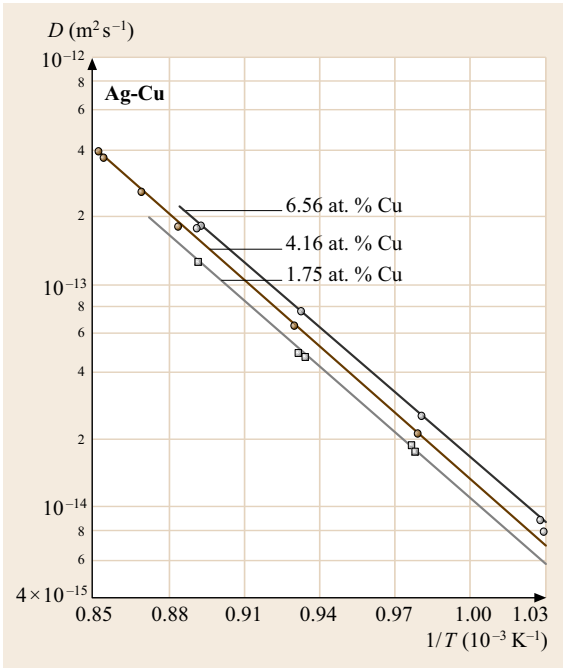


**Fig. 14.21** Self-diffusion of $^{110m}$Ag in Ag-Cu (1.75–6.56 at.% Cu) alloys (after [14.23])

**Table 14.43** Diffusion of H and O in Ag, Pd, Pt, and Au (after [14.2])

| Matrix | Gas | $D^0$ ($10^{-4}$ m$^2$/s) | $Q$ (kJ/mol) | $T$ (K) |
|---|---|---|---|---|
| Ag | H | $8.55\times10^{-3}$ | 30.11 | 947–1123 |
| Ag | O | $3.66\times10^{-3}$ | 46.1 | 680–1140 |
| Pd | H | $2.9\times10^{-3}$ | 22.19 | 473–1548 |
| | D | $1.7\times10^{-3}$ | 19.88 | 218–233 |
| | T | $7.2\times10^{-3}$ | 23.8 | 273–323 |
| Pt | H | $6\times10^{-3}$ | 24.70 | 600–900 |
| Au | H | $5.6\times10^{-4}$ | 23.61 | 773–1213 |

### 14.1.10 Chemical Properties

Silver has the reduction potential of $E_0 = +0.8$ V for $Ag/Ag^+$. It is resistant against dry oxygen, air, non-oxidizing acids, organic acids, and alkali. Water and water vapor do not attack Ag up to 600 °C. Ag is dissolved in alkaline cyanidic solutions in the presence of oxidizing agents, air, and oxygen. $H_2S$ attacks Ag readily at room temperature, forming black $Ag_2S$ layers (tarnish) [14.2].

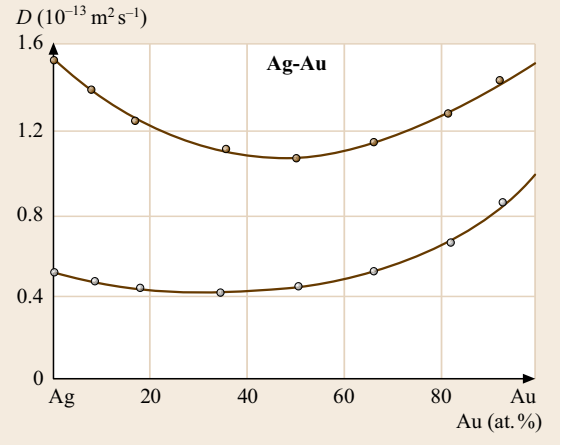


**Fig. 14.22** Self-diffusion of $^{110m}$Ag (*brown circles*) and $^{198}$Au (*gray circles*) in Ag-Au (8–94 at.%) Ag-Au alloys (after [14.23])

Metallic Ag and Ag-Au alloys are heterogeneous catalysts for oxidation processes, e.g., in the production of ethylene oxide and formaldehyde applied as grids or as powder preparations on $Al_2O_3$ or carbon substrates [14.2].

### 14.1.11 Ag-Based Materials

Binary alloys (Tables 14.44–14.46) [14.3]: Ag-Ni alloys are grain-stabilized materials usually containing 0.15 wt% Ni. Ag-Cu alloys have manifold applications in jewelry, silverware, brazes, and solders. Jewelry, silver ware alloys, and coins usually contain between 7.5 wt% Cu (*sterling silver*) and 20 wt% Cu. The material Ag–28 wt% Cu is the most common silver brazing alloy. Alloys of Ag-Mn are special solders for hard metal and refractory metals (Mo, W). The alloy Ag–1 wt% Pt is applied in thick film layers for conductor paths in passive electronic devices. Ag-Pd powder preparations containing 10–30 wt% Pd form the conductor layers in multilayer capacitors (Table 14.47) [14.2].

### 14.1.12 Ternary and Higher Alloys

Alloys of the systems Ag-Cu-Sn, Ag-Cu-Zn, and Ag-Cu-$Cu_3P$ are used as solders and brazes. Ag-Cu-P solder alloys can be applied without flux. Ti-containing

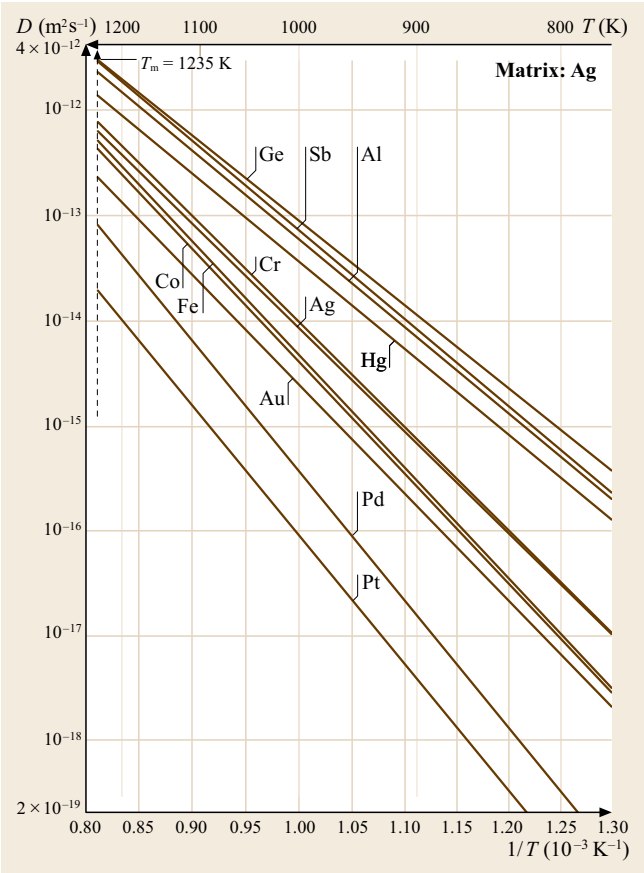


**Fig. 14.23** Diffusion of impurities in Ag (after [14.23])

solder alloys (active solders) allow direct bonding to ceramics (Table 14.47) [14.24]. Alloys of the systems Ag-Au-Cu, Ag-Au-Ni, and Ag-Cu-Pd are applied in jewelry and dentistry (Tables 14.71 and 14.72).

The oxide AgO forms the cathode of AgO/Zn button type batteries with a cell voltage of 1.55 V and with energy densities in the range of 80–250 W h/dm$^2$ [14.3, 25–27].

Composite materials with $SnO_2$, CdO, C, Ni, and refractory carbides as dispersoids are base materials of electrical contacts (Tables 14.48, 14.49, and Fig. 14.24) [14.11, 16, 28]. Extruded powder composites show preferred alignment of the dispersoid particles along the rod axes. Silver–nickel fiber composites are magnetic. Their coercivity increases with decreasing diameter of the Ni fibers [14.29].

**Table 14.44** Noble metal containing soft solders (after [14.2])

| Alloy (wt%) | Melting range (°C) | Density ($g/cm^3$) | Tensile strength ($N/mm^2$) | Elongation (%) | Elastic modulus ($N/mm^2$) | Thermal expansion ($10^{-6}\ K^{-1}$) | Electrical conductivity ($10^6$ S/m) | Thermal conductivity (W/(m K)) |
|---|---|---|---|---|---|---|---|---|
| AuSn20 | 280 | 14.57 | 275 | < 1 | 59 200 | 16 | < 5 | 57.3 |
| AuGe12 | 356 | 14.70 | 150–200 | < 1 | 69 300 | 13.4 | 7 | 44.4 |
| AuSi2 | 363–740 | 14.50 | 500–600[a] | 0.5–3[a] | | 12.6 | 33 | 50 |
| SnAg25Sb10 | 228–395 | 7.86 | 80–120 | 1–4 | 23 000 | 19 | 6.5 | 55 |
| SnAg3.5 | 221 | 7.38 | 25–35 | 20–30 | 41 100 | 27.9 | 7.5 | 57 |
| PbSn5Ag2.5 | 280 | 11.70 | 25–35 | 20–30 | 21 300 | 29 | < 5 | 44 |
| PbIn5Ag2.5 | 307 | 11.60 | 35–40 | 28–34 | 19 900 | 29 | < 5 | 42 |

[a] Hard rolled condition

**Table 14.45** Noble-metal-containing brazing alloys (after [14.2])

| Alloy(wt%) | Melting range (°C) | Density ($g/cm^3$) | Tensile strength ($N/mm^2$) | Elongation (%) | Elastic modulus ($N/mm^2$) | Thermal expansion ($10^{-6}\ K^{-1}$) | Electrical conductivity ($10^6$ S/m) | Thermal conductivity (W/(m K)) | ISO Type 3677 |
|---|---|---|---|---|---|---|---|---|---|
| AgCu28 | 779 | 10.00 | 250–350 | 20–28 | 100 000 | 19.8 | 10 | | B-Ag72-Cu780 |
| AgCu27In13 | 605–710 | 9.70 | 400–500 | 20–30 | 85 000 | 17.8 | 46.1 | 352 | B-Ag60CuIn-695/710 |
| AgCu26.6Pd5 | 807–810 | 10.10 | 370–410 | 12–20 | 120 000 | 22 | 26 | 215 | B-Ag68CuPd-807/810 |
| AgCu31.5Pd10 | 824–852 | 10.10 | 500–540 | 2–5 | 140 000 | 17.5 | 19 | 150 | B-Ag58CuPd-824/852 |
| AgCu20Pd15 | 850–900 | 10.40 | 510–550 | 5–9 | 140 000 | 22 | 15 | 100 | B-Ag65CuPd-850/900 |
| AgCu21Pd25 | 910–950 | 10.50 | 540–580 | 13–21 | 140 000 | 17.5 | 8 | 80 | B-Ag54PdCu-901-950 |
| AgPd5 | 970–1010 | 10.50 | 180–220 | 26–34 | 40 000 | 22 | 25 | 220 | B-Ag95Pd-970/1010 |
| CuPd18 | 1080–1090 | 9.40 | 380–420 | 31–39 | 135 000 | 18.9 | 9.1 | 100 | B-Cu82Pd-1080/1090 |
| AgCu28Pd20 | 879–898 | 10.30 | 580–620 | 6–10 | 100 000 | 18.6 | 9.5 | 95 | B-Ag52CuPd-879/898 |
| AuNi18 | 950 | 15.96 | 550–650 | 8 | | 14.6 | 5.9 | | B-Au82Ni-950 |

**Table 14.46** Physical properties of noble-metal-containing vacuum braze alloys (after [14.2])

| Alloy | Composition | Solidus (°C) | Liquidus (°C) |
|---|---|---|---|
| Ag-Cu | Ag40Cu19Zn21Cd20 | 595 | 630 |
| | Ag60Cu27In13 | 605 | 710 |
| | Ag44Cu30Zn26 | 675 | 735 |
| | Ag72Cu28 | 779 E[a] | |
| Ag-Mn | Ag85Mn15 | 950 | 950 |
| Ag-Pd | Ag68.4Pd5Cu26.6 | 807 | 810 |
| | Ag54Pd25Cu21 | 901 | 950 |
| | Ag75Pd20Mn5 | 100 | 1120 |
| Pd-Cu | Pd18Cu72 | 1080 | 1090 |
| Pd-Ni | Pd60Ni40 | 1237 | 1237 |
| Au-Cu | Au80Cu20 | 890 | 890 |
| | Au35Cu65 | 990 | 1010 |
| Au-Ni | Au82Ni18 | 950 | 950 |

[a] E = eutectic composition

**Table 14.47** Typical powder grades of Ag, Pd, and Ag-Pd preparations for capacitors

| Metal | Manufacturing method | Grain shape | Grain size (μm) | Tap density (g/cm$^3$) | Specific surface[a] (m$^2$/g) |
|---|---|---|---|---|---|
| Ag | Chemical reduction | Microcrystalline | 0.5–2.0 | 0.8–5.0 | 0.1–2.0 |
| | Electrolytic deposition | Dendritic | 1–200 | 4.5–4 | 0.1–0.5 |
| | | ↓ | | | |
| | Ball milling | Flakes | 2–40 | 2.5–5 | 0.2–1.8 |
| Pd | Chemical reduction | Crystalline | < 20 | 0.8 | 2.5 |
| | | ↓ | | | |
| | | Spheres | < 1.2 | 4.0 | 2.3 |
| AgPd30 | Coprecipitation | Spheres | < 1.2 | 3.3 | 2.2 |
| | | ↓ | | | |
| | | Flakes | < 9 | 3.4 | 3.3 |

[a] BET in $N_2$ adsorption

**Table 14.48** Hardness and electrical conductivity of Ag-Ni-C (contact) alloys (after [14.11])

| | | | | | |
|---|---|---|---|---|---|
| Alloy content wt% C | 3 | 2 | 2.5 | 2.5 | 2.5 |
| Alloy content wt% Ni0.5 | 0.5 | 0.5 | 1 | 5 | 10 |
| HV (kg/mm$^2$)$^{40.5}$ | 43 | 53 | 50 | 53 | 56–57 |
| Electrical conductivity in % of standard Cu | 63.7 | 74.8 | 69.8 | 67.3 | 64.5 |

**Table 14.49** Silver bearing composite contact materials (after [14.28])

| Type | Composition (at.%) | Hardness HV | Electrical conductivity (m/(Ω mm$^2$)) |
|---|---|---|---|
| Alloys | AgNi (0.15) | 100 | 58 |
| | AgCu (3) | 120 | 52 |
| | ↓ | | |
| | AgCu (20) | 150 | 49 |
| **Composites with:** | | | |
| Metals | Ag-Ni (10) | 90 | 54 |
| | ↓ | | |
| | Ag-Ni (40) | 115 | 37 |
| Oxides | Ag-CdO (10) | 80 | 48 |
| | ↓ | | |
| | Ag-CdO (15) | 115 | 45.5 |
| | Ag-ZnO (88) | 95 | 49 |
| | Ag-$SnO_2$ (8) | 92 | 51 |
| | Ag-$SnO_2$ (12) | 100 | 42 |
| Carbon | Ag-C (2) | 40 | 48 |
| | Ag-C (5) | 40 | 43.5 |
| Refractory metal compounds[a] | Ag-W (20) | 240 | 26–28 |
| | ↓ | | |
| | Ag-W (80) | 80 | 42 |
| | Ag-WC (40) | 130 | 24–30 |
| | ↓ | | |
| | Ag-WC (80) | 470 | |

[a] Composite made by infiltration of liquid silver into a tungsten skeleton

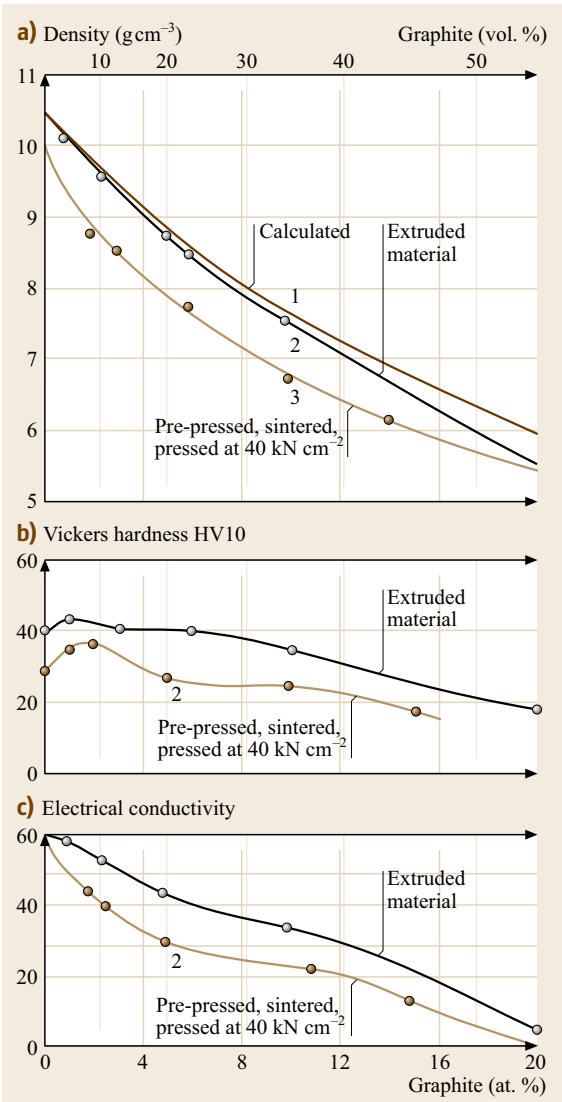


**Fig. 14.24** (a) Density, (b) hardness, and (c) electrical conductivity of Ag-C alloys (after [14.16])

## 14.2 Gold and Gold Alloys

Gold and gold alloys are used for electrical contacts, bonding wires and conductor paths in semiconductor devices, chemical and corrosion resistant materials, thin surface coatings for optical and heat reflecting mirrors, special thermocouples, and catalysts for organic chemical reactions. Classical applications are jewelry, dentistry, monetary bars, and coins. Commercial grades: Table 14.50. The purity grades of gold bars are standardized in the range of 99.9 to 99.999 wt% (ASTM B 562-86, Tables 14.50 and 14.51) [14.2].

### 14.2.1 Production

Elementary gold is extracted from ores by cyanide leaching and precipitated with zinc, and by electrolysis. Refining is achieved by application of chlorine gas up to 99.5%, and to 99.9% and higher by electrolysis. Bars, sheets and wires are made by casting, rolling and drawing; powder is formed by chemical and by electrolytic precipitation from solutions; and nanocrystalline powders are formed by dispersion in organic solutions. Coatings are produced by cladding; electroplating; and applying powder preparations followed by firing. Thin films are produced by evaporation and cathode sputtering. Very fine gold leaves are made by traditional hammering to a thickness of $\approx 0.2\,\mu m$, or by cathode sputtering.

### 14.2.2 Phases and Phase Equilibria

Selected phase diagrams are shown in Figs. 14.25–14.34 [14.4, 30]. Continuous solid solutions are formed with Ag, Co, Cu, Fe, Ni, Pd, and Pt. Miscibility gaps occur with Be, Ni, Pt, Rh, and Ru. Thermochemical data are listed in Tables 14.52 and 14.53 [14.2, 7].

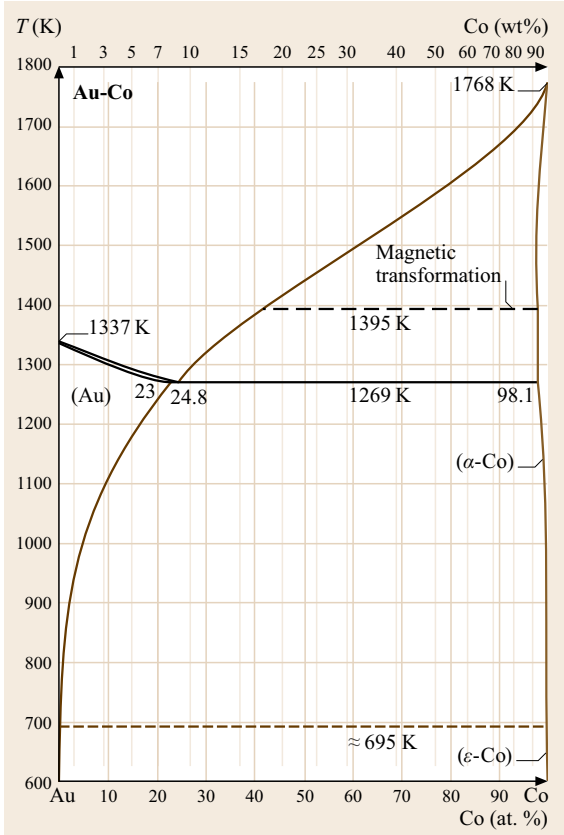


**Fig. 14.25** Binary phase diagram: Au-Co (after [14.4])

Compositions, crystal structures and lattice parameters of selected intermetallic compounds are given in Table 14.54 [14.2] and in Figs. 14.35 and 14.36 [14.4]. Primary solid solutions have the fcc structure of Au.

**Table 14.50** Specifications of fine gold (after [14.2])

| Designation | Grade (wt%) | Impurity | Maximum content (ppm) |
|---|---|---|---|
| *Good delivery* gold | 99.5 | Any, total | 5000 |
| Fine gold | 99.99 | Ag/Cu/others/total | 100/20/30/100 |
| Fine gold, chemically pure | 99.995 | Ag/others/total | 25/25/50 |
| Fine gold, high purity | 99.999 | Ag/Fe/Bi/Al/Cu/Ni/Pd + Pt/total | 3/3/2/0.5/0.5/0.5/5/10 |

**Table 14.51** Standard fineness of noble metal alloys and corresponding carat of jewelry (after [14.2])

| | Fineness (wt‰) | | | | | |
|---|---|---|---|---|---|---|
| Au | | 375 | 585 | 750 | 916.999 | |
| Ag | | | | | 800.925 999 | |
| Pd | | | 500 | | 850.900 950 999 | |
| Pt | | | 500 | | 950.999 | |
| | 333 | 375 | 585 | 750 | | 1000 |
| Karat | 8 | 9 | 14 | 18 | 22 | 24 |

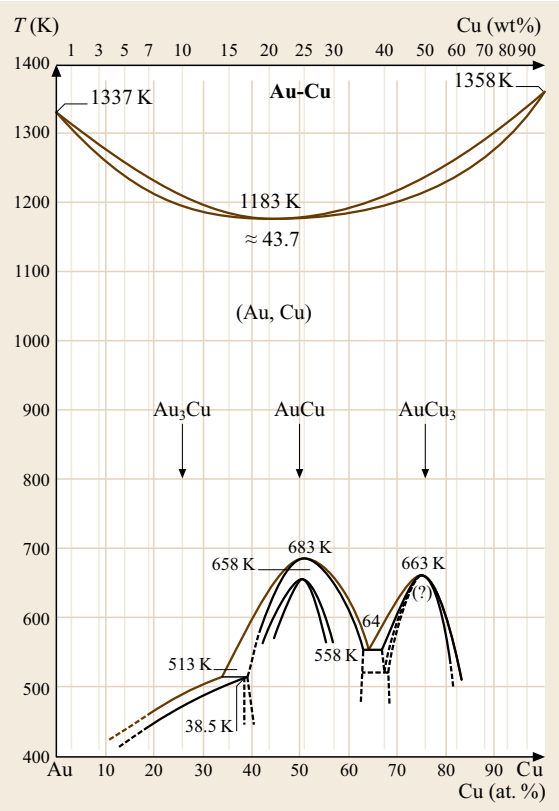


**Fig. 14.26** Binary phase diagram: Au-Cu (after [14.4])

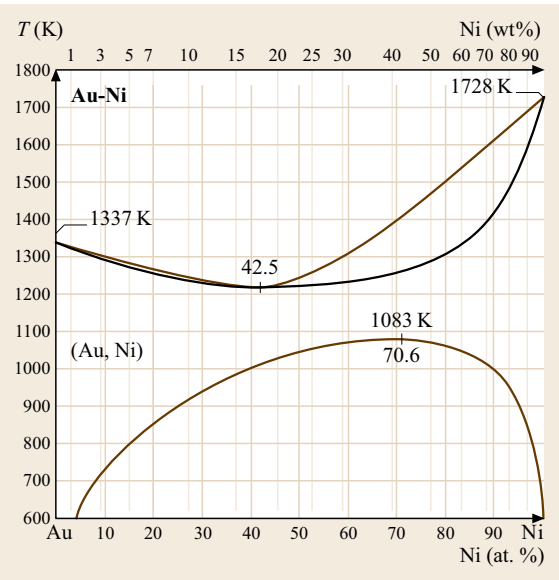


**Fig. 14.27** Binary phase diagram: Au-Ni (after [14.4]) ◄

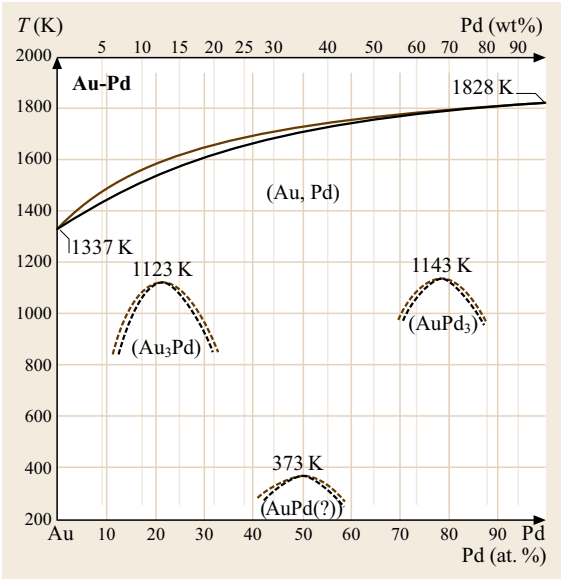


**Fig. 14.28** Binary phase diagram: Au-Pd (after [14.4])

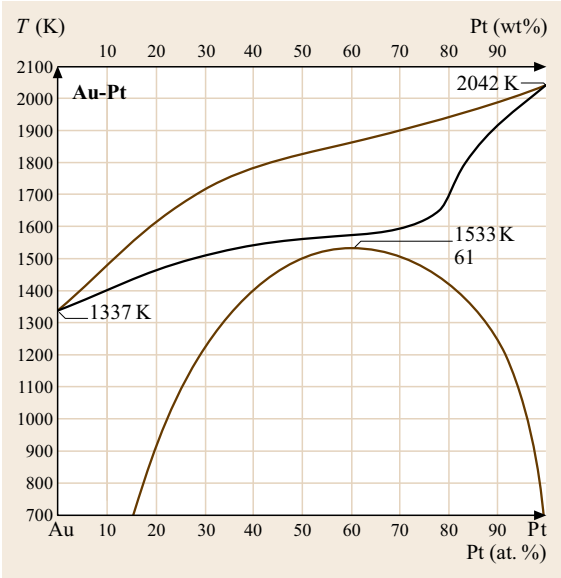


**Fig. 14.29** Binary phase diagram: Au-Pt (after [14.4])

The lattice parameters of the substitutional solid solutions correspond roughly to Vegard's law with a few exceptions [14.31].

**Table 14.52** Thermodynamic data of Au (after [14.2])

| $T$ (K) | $c_p$ (J/(K mol)) | $S$ (J/(K mol)) | $H$ (J/mol) | $G$ (J/mol) | $p$ (at) |
|---|---|---|---|---|---|
| 300 | 25.303 | 47.645 | 0.047 | −14.247 | $6.87 \times 10^{-58}$ |
| 500 | 26.158 | 60.757 | 5.188 | −25.191 | $2.82 \times 10^{-32}$ |
| 700 | 27.028 | 69.701 | 10.509 | −38.282 | $2.49 \times 10^{-21}$ |

$T$ = temperature, $c_p$ = specific heat capacity, $S$ = entropy, $H$ = enthalpy, $G$ = free enthalpy, $p$ = partial pressure of the pure elements

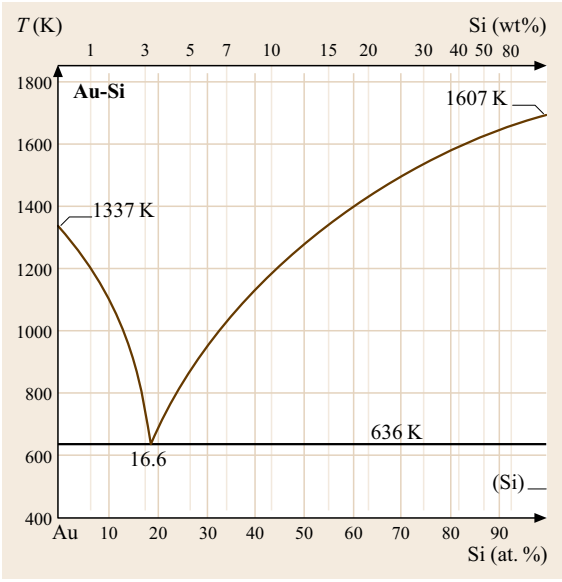


**Fig. 14.30** Binary phase diagram: Au-Si (after [14.4])

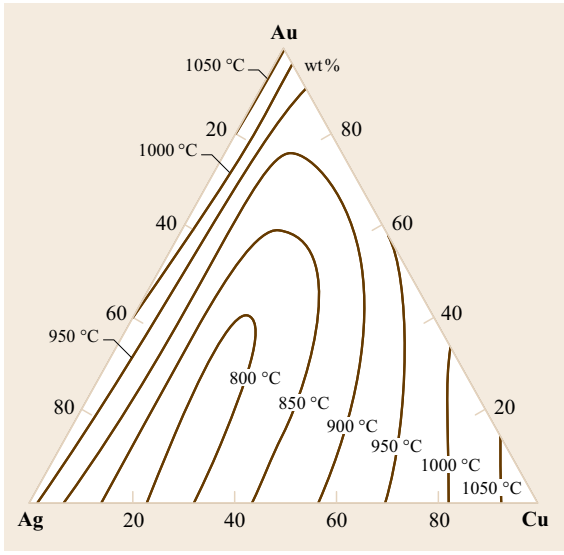


**Fig. 14.31** Liquidus sections through the miscibility gap of the Au-Ag-Cu system (after [14.30])

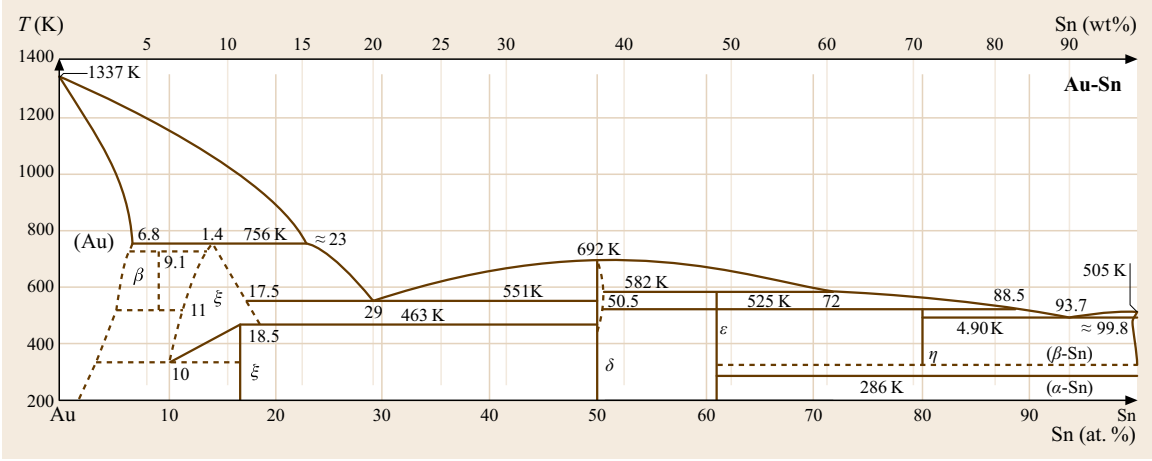


**Fig. 14.32** Binary phase diagram: Au-Sn (after [14.4])

**Table 14.53** Heats, entropies and free energies of formation of Au compounds (after [14.7])

| Phase | $N_2$ | $T$ (°C) | $H$ (J/mol) | $G$ (J/mol) | $S$ (J/K mol) |
|---|---|---|---|---|---|
| AuCu s.s. | 0.58 | 500 | 5.32 | 9.67 | 5.65 |
| $Au_3Cu$ | 0.26 | 25 | 4.03 | 4.90 | 2.97 |
| AuCu I | 0.50 | 25 | 8.96 | 8.96 | – |
| AuCu II | 0.50 | 400 | 6.03 | 8.79 | 4.10 |
| $AuCu_3$ | 0.75 | 25 | 6.87 | 7.24 | 1.26 |
| AuNi s.s. | 0.53 | 877 | −7.5 | – | 8.71 |
| AuSn | 0.50 | 25 | 14.24 | – | −0.4 |

$N_2$ = mole fraction of second compound,
$S$ = entropy of formation, s.s. = solid solution

**Table 14.54** Structure and lattice parameters of selected intermediate Au compounds (after [14.2])

| Phase | Pearson symbol | $a$ (nm) | $b$ (nm) | $c$ (nm) | $c/a$ | Remarks | Concentration $A_{1-x}B_x$ |
|---|---|---|---|---|---|---|---|
| AuAl | *mPs* | 0.6415 | 0.3331 | 0.6339 | | | |
| $Au_2Al$ | *oP*30 | 0.8801 | 1.6772 | 0.3219 | | LT | 0.664–0.667 |
| $Au_5Al$ | *cP*20 | 0.69208 | | | | LT | |
| Au-$Al_2$ | *cF*12 | 0.59973 | | | | | 0.334 |
| AuCu | *oI*40 | 0.3676 | 0.3972 | | | 773 K | |
| AuCu | *oP*8 | 0.456 | 0.892 | 0.283 | | | |
| AuCu | *tP*4 | 0.3966 | | 0.3673 | 0.9261 | | 0.46–0.54 |
| $Au_3Cu$ | *cP*4 | 0.39853 | | | | | |
| Au-Pd | *cP*4 | 0.3991 | | | | | 0.552 |
| Au-Pt | *cF*4 | 0.3996 | | | | | 0.5 |
| Au-Sn | *hP*2 | 0.29228 | | 0.47823 | 1.6329 | | 0.14 |
| AuSn | *hP*4 | 0.43218 | | 0.5523 | 1.2779 | | |
| $AuSn_4$ | *oC*20 | 0.6502 | 0.6543 | 1.1705 | | 475 K | |
| $Au_4Ti$ | *tI*10 | 0.6485 | | 0.4002 | 0.6171 | | |

LT = low-temperature modification

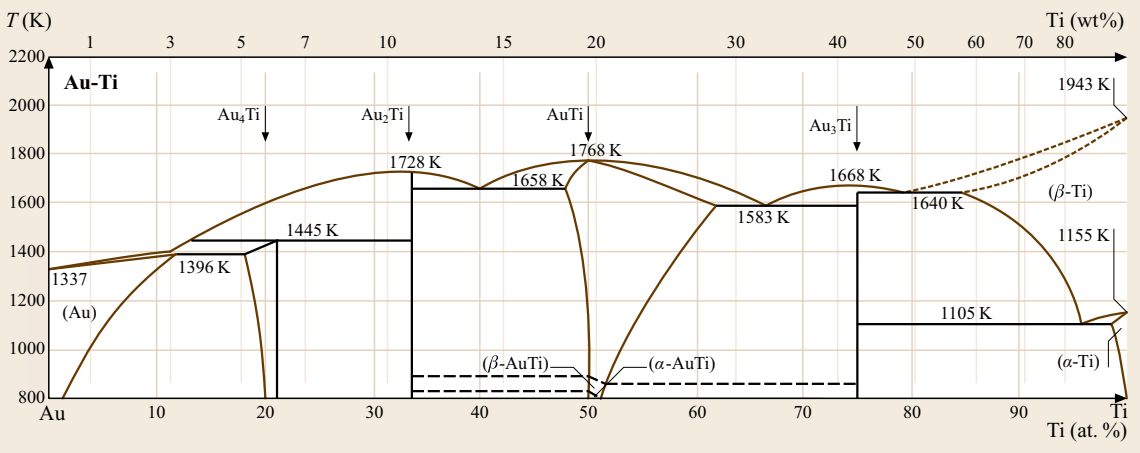


**Fig. 14.33** Binary phase diagram: Au-Ti (after [14.4])

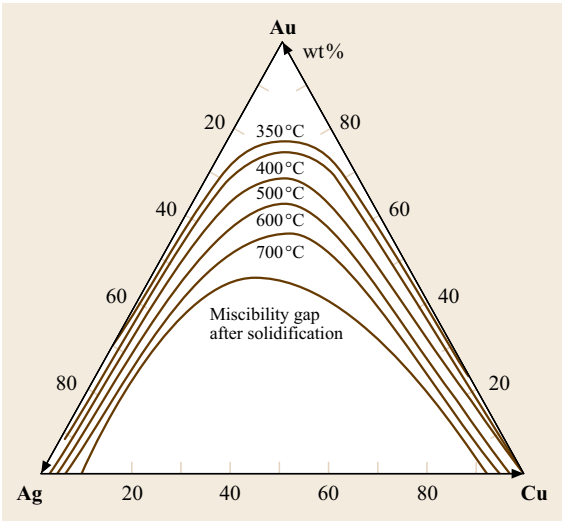


**Fig. 14.34** Isothermal sections through the miscibility gap of the Au-Ag-Cu system (after [14.30])

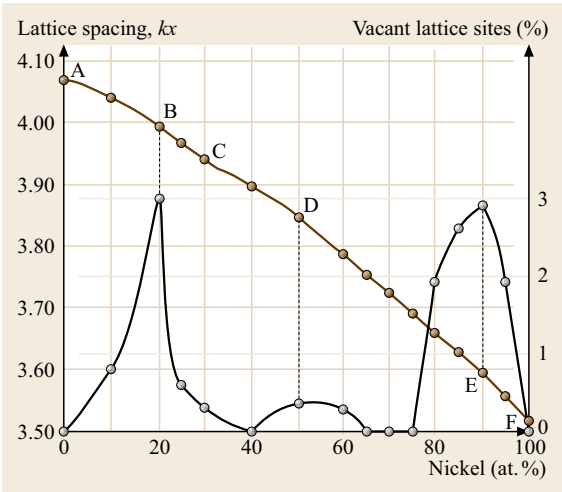


**Fig. 14.35** Vacant lattice sites in Au-Ni alloys (after [14.10])

Superlattice phases occur in alloys with Cd, Cu, Mn, Pd, Pt, Rh, Ru, and Zn. The superlattice structures have tetrahedral or rhombohedral symmetry. Typical compositions are $AB_3$ and $A_3B$ [14.3]. If they are not precipitated as second phases, superlattice phases form antiphase domains on different sublattices separated by antiphase domain boundaries. Intermetallic compounds are formed with numerous elements with different and complex crystal structures [14.10]. Metastable phases

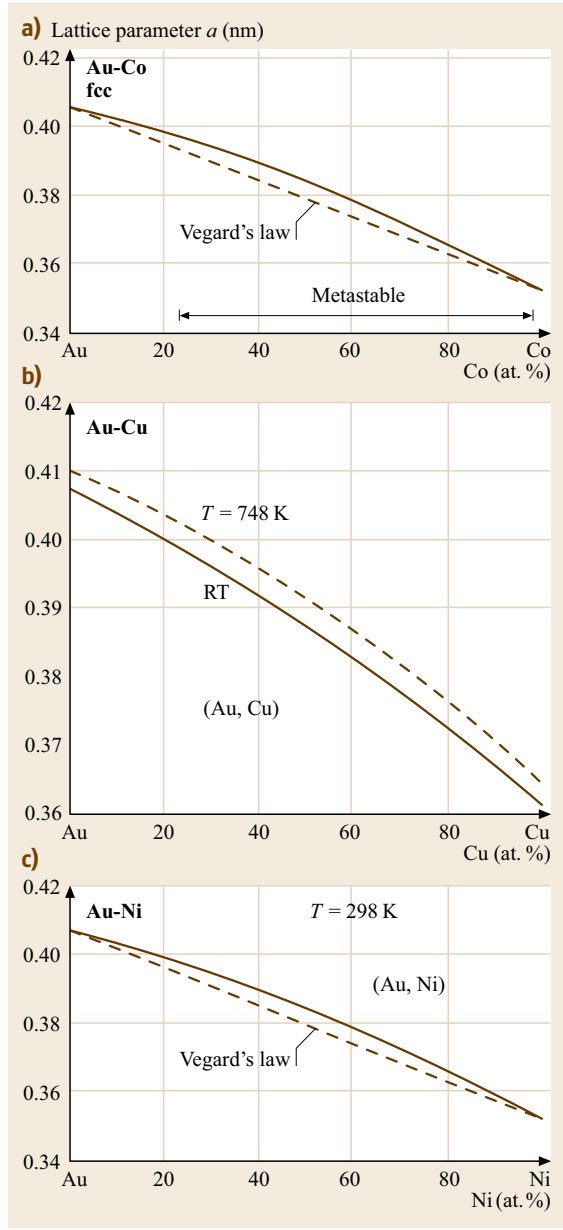


**Fig. 14.36a–c** Lattice parameter versus composition in the systems **(a)** Au-Co (fcc), **(b)** Au-Cu, and **(c)** Au-Ni (after [14.4])

exist with Ni and Pt. Alloys with B-metals form intermetallic phases at compositions corresponding to e/a values of 3/2, 21/13, and 7/4 (Hume-Rothery phases). Structural types of intermetallic compounds of gold with rare earth metals are listed in [14.32].

### 14.2.3 Mechanical Properties

The mechanical properties of gold are given in Tables 14.55–14.61 and Figs.14.37–14.48 [14.1, 2]. References for data of elastic constants of Au alloys are given in [14.2]. Pure gold is very soft. It can be cold-worked to more than 90% by rolling or drawing. Cold hard drawn wires (about 90% deformation) have predominantly ⟨111⟩ fiber texture, which is converted by annealing into ⟨100⟩ orientation [14.33]. Strengthening of pure gold is affected by alloying (solid solution hardening, precipitation hardening) or by dispersion hardening. Ternary Au-Ag-Cu alloys can be hardened by decomposition into Cu-rich Cu-Au and Ag-rich Ag-Au phases during annealing below the critical temperature of the miscibility gap and by formation of the ordered Au-Cu-phase at more than 75 wt% Au. Hardening of Au by alloying with rare-earth metals is described in detail in [14.32]. Grain refinement, applied especially to jewelry and dentistry alloys, is affected by the addition of 0.05−1 at.% of Ir, Ru, or Co [14.34, 35].

**Table 14.55** Modulus of elasticity of Au in crystal directions (GPa) (after [14.2])

| $E$ ⟨100⟩ | $E$ ⟨110⟩ | $E$ ⟨111⟩ |
|---|---|---|
| 42 | 81 | 114 |

**Table 14.56** Elastic constants of Au (GPa) (after [14.2])

| $T$ (°C) | $c_{11}$ | $c_{12}$ | $c_{14}$ |
|---|---|---|---|
| −273 | 131.4 | 97.3 | 51.1 |
| 20 | 124.0 | 93.4 | 46.1 |

**Table 14.57** Mechanical properties of Au (99.99%) at different temperatures (after [14.2])

| $T$ (°C) | $E$ (GPa) | $R_m$ (MPa) | $R_{p0.2}$ (MPa) | HV |
|---|---|---|---|---|
| 20 | 79 | 125 | 30 | 28 |
| 200 | 75 | 110 | 20 | 19 |
| 400 | 70 | 92 | – | 16 |
| 700 | 58 | 40 | – | 5 |

$E$ = modulus of elasticity, $R_m$ = tensile strength, $R_p$ = limit of proportionality, HV = Vickers hardness

**Table 14.58** Tensile strength $R_m$ (MPa) of binary Au alloys (after [14.2])

| Alloying element | Content (wt%) | | | |
|---|---|---|---|---|
| | 2 | 5 | 10 | 20 |
| Ag | 140 | 150 | 170 | 190 |
| Co | 240 | – | – | – |
| Cr | 200 | – | – | – |
| Cu | 190 | 290 | 400 | 500 |
| Fe | 190 | – | – | – |
| Ni | 220 | 350 | 470 | 680 |
| Pd | 150 | 170 | 220 | 290 |
| Pt | 150 | 189 | 240 | 370 |

**Table 14.59** Mechanical properties of Au (99.99%) as a function of the reduction $V$ in thickness by cold forming (after [14.2])

| $V$ (%) | $R_m$ (MPa) | $A$ (%) | HV |
|---|---|---|---|
| 0 | 120 | 45 | 28 |
| 10 | 140 | 22 | 55 |
| 30 | 180 | 75 | 63 |
| 50 | 220 | 4 | 65 |

$R_m$ = tensile strength, $A$ = elongation of rupture, HV = Vickers hardness

**Table 14.60** Change of hardness (HV 10) of Au alloys by cold forming (after [14.2])

| Alloying element | Degree of reduction in thickness (%) | | |
|---|---|---|---|
| | 0 | 40 | 80 |
| Ag20 | 40 | 95 | 1141 |
| Ag25Cu5 | 92 | 160 | 188 |
| Ag20Cu10 | 120 | 190 | 240 |
| Co5 | 92 | 126 | 154 |
| Ni5 | 120 | 162 | 188 |
| Pt10 | 78 | 102 | 118 |
| Pd30Cu5 | 92 | 174 | 216 |

**Table 14.61** Mechanical properties of AuPt alloys in annealed and aged condition (after [14.2])

| Alloy | $R_m$ (MPa) | $A$ (%) | HV |
|---|---|---|---|
| Pt10[a] | 250 | 38 | 42 |
| Pt30[a] | 430 | 12 | 120 |
| Pt30[b] | 740 | – | 300 |
| Pt50[a] | 900 | 3 | 240 |
| Pt50[c] | 1460 | 2 | 420 |

[a] Annealed at 1000−1150 °C and quenched, [b] stored 70 h at 500 °C, [c] stored 25 h at 500 °C

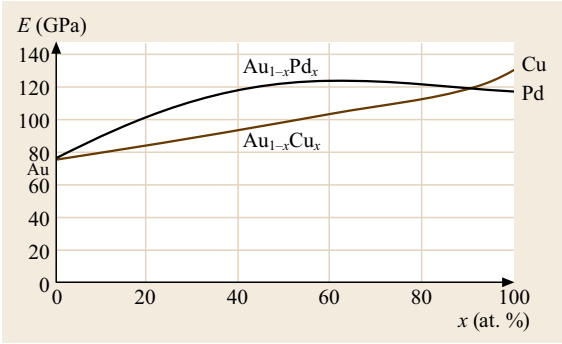


**Fig. 14.37** Modulus of elasticity of Au-Cu and Au-Pd alloys (after [14.2])

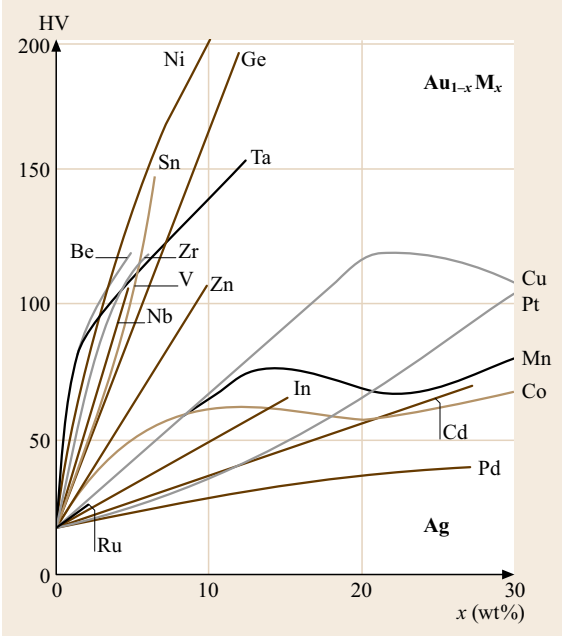


**Fig. 14.38** Influence of alloying elements on the hardness of binary Au alloys (after [14.2])

**Fig. 14.40a–c** Hardness of Au-Co alloys by annealing; **(a)** influence of time, **(b)** influence of temperature (after [14.16]) ►

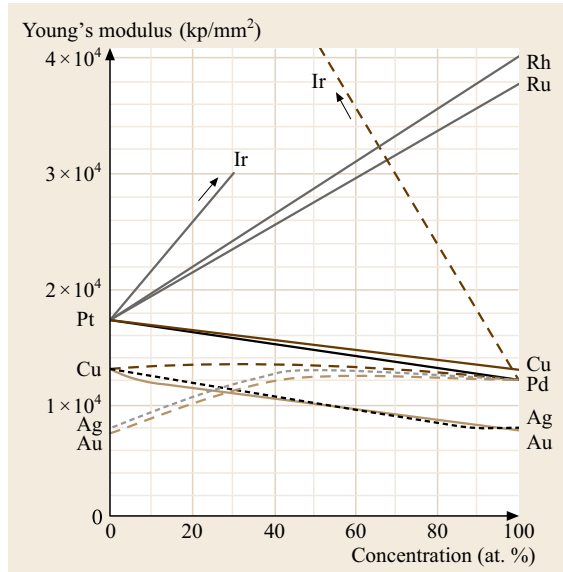


**Fig. 14.39** Modulus of elasticity versus composition of binary noble-metal alloys (after [14.1])

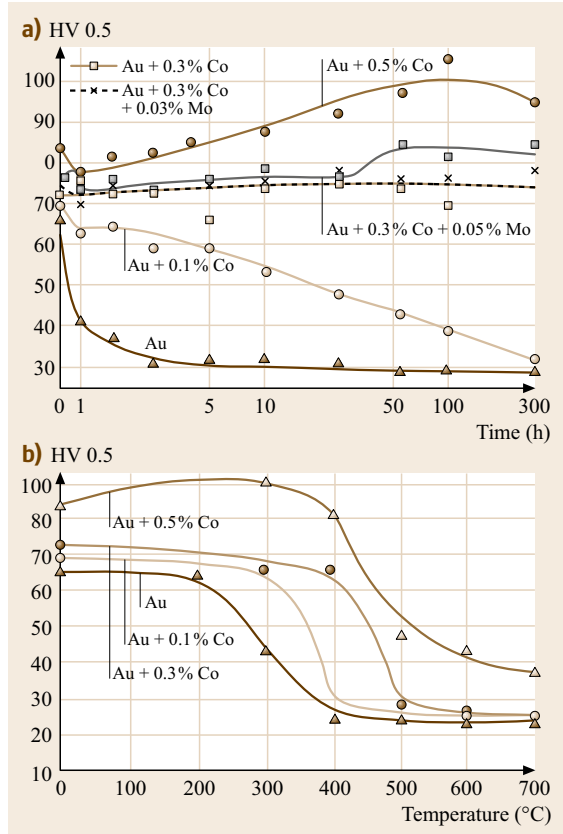

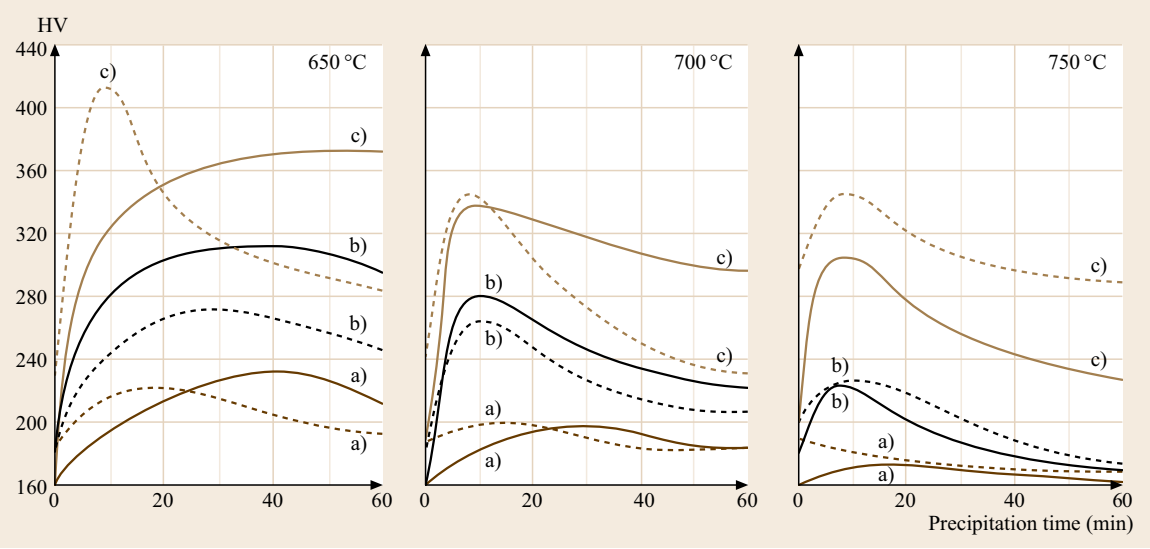


**Fig. 14.41** Precipitation hardening of Au/Pt-40 (*solid curve*) and Au/Pt-50 (*dashed curve*): solution treatment 15 min at a) 950 °C, b) 1050 °C and c) 1150 °C. Precipitation hardening performed at 650, 700, and 750 °C (after [14.3])

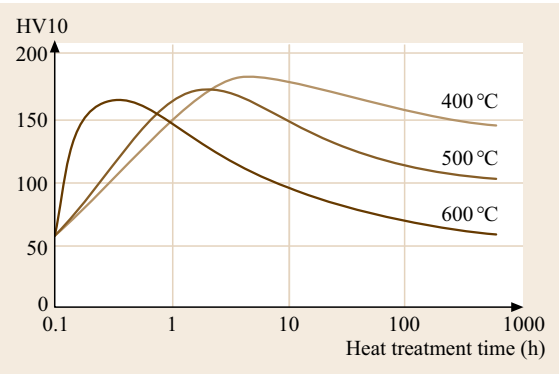


**Fig. 14.42** Precipation-hardening characteristic of Au-1% Ti alloy by annealing (after [14.36])

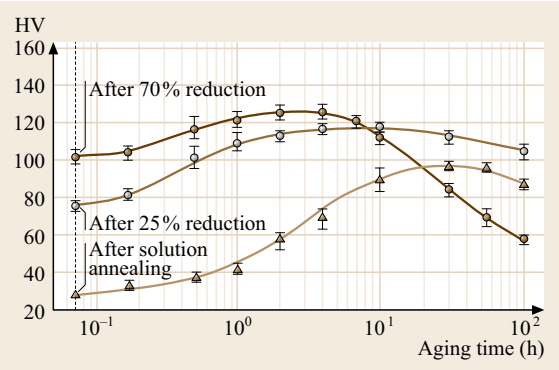


**Fig. 14.43** Hardness of the alloy AuSb0.3Co0.2 as a function of the reduction in thickness and of annealing time (after [14.38]) ◄

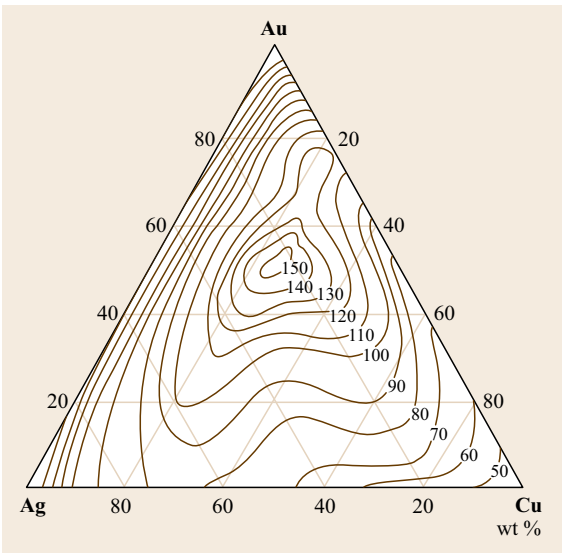


**Fig. 14.44** Hardness of annealed and quenched Au-Ag-Cu alloys (after [14.37])

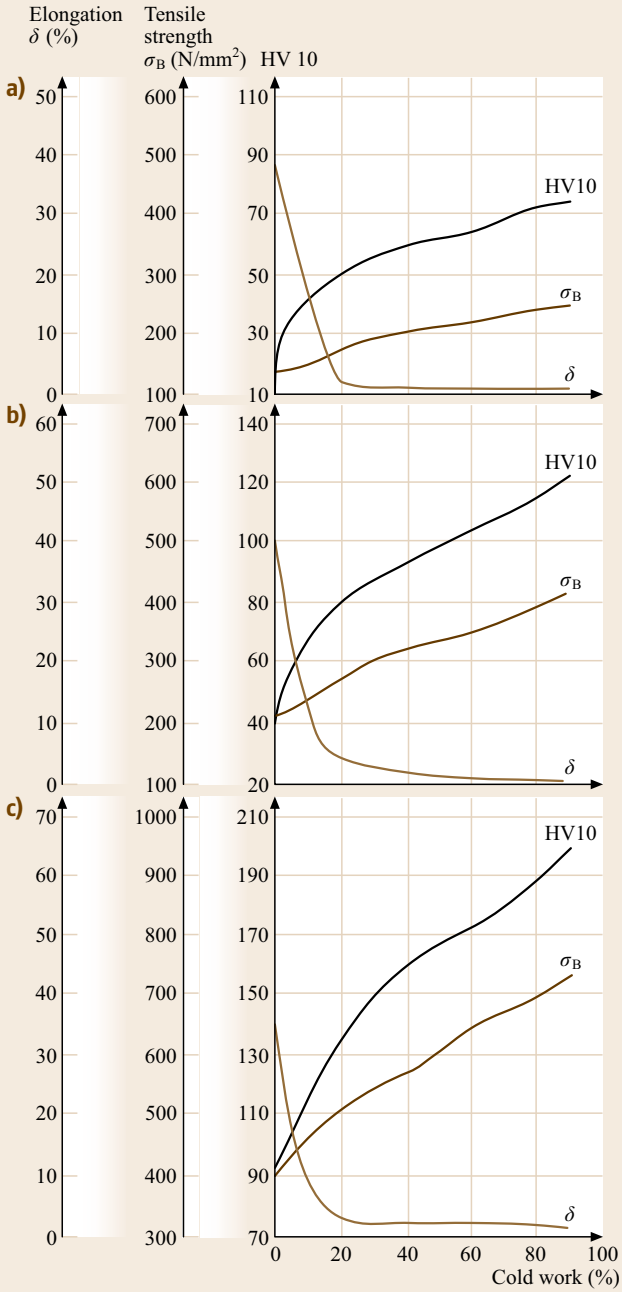


**Fig. 14.45** Mechanical properties of (a) Au, (b) AuAg30, and (c) AuAg25Cu5 as a function of the reduction in thickness (%) (after [14.16])

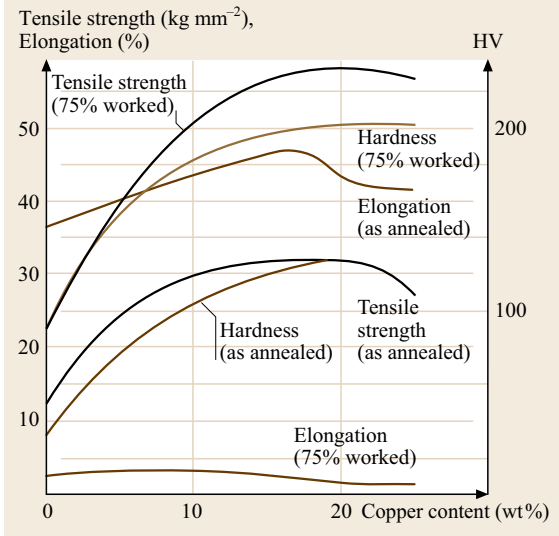


**Fig. 14.46** Tensile strength and hardness of 18 kt Au-Ag-Cu alloys as a function of Cu content (after [14.3])

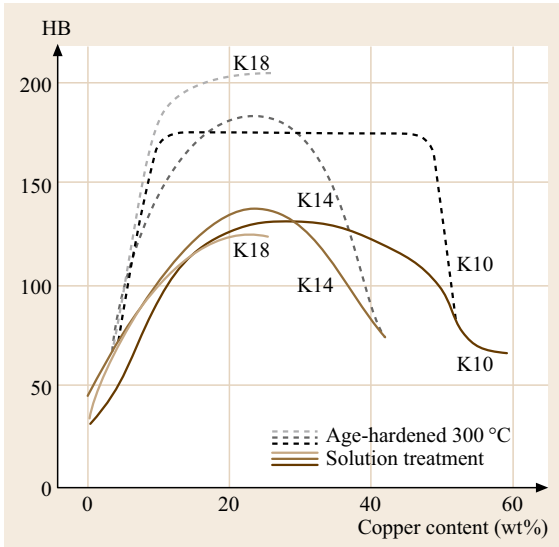


**Fig. 14.47** Influence of Cu content on age hardening of 10, 14 and 18 kt Au-Ag-Cu alloys (after [14.3])

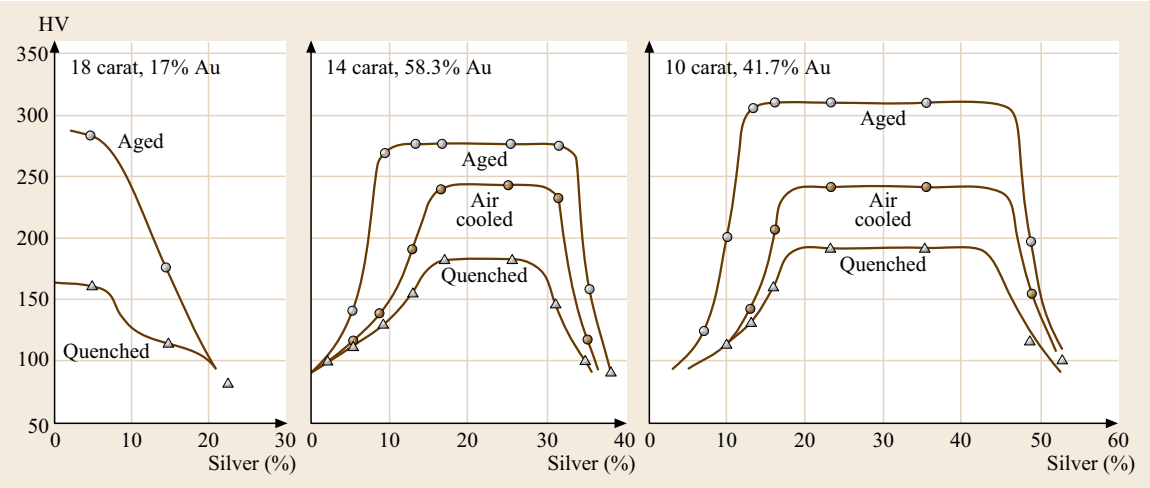


**Fig. 14.48** Variation of hardness with silver content for Au-Ag-Cu alloys (after [14.2])

**Table 14.62** Specific electrical resistivity $\rho = \rho_0 + \rho_i(T)$ of Au at different temperatures (after [14.2])

| $T$ (K) | 20 | 60 | 120 | 273.2 | 400 | 800 | 1000 | 1200 |
|---|---|---|---|---|---|---|---|---|
| $\rho$ ($\mu\Omega$ cm) | 0.0138 | 0.287 | 0.796 | 2.031 | 3.094 | 6.742 | 8.871 | 11.299 |

$\rho_0 = 0.0222\,\mu\Omega$ cm at $T < 400$ K, $\rho_0 = 0.014\,\mu\Omega$ cm at $T > 400$ K

## 14.2.4 Electrical Properties

Tables 14.62–14.64 and Figs. 14.49 and 14.50 [14.2, 16, 39] summarize the electrical properties of gold and gold alloys. The RRR for high purity gold amounts to 300. The electrical conductivity of gold alloys decreases in the low concentration range roughly linearly with the atomic concentration of the solute. Au alloys with 1.15 wt% Mn show increasing temperature coefficients of the electrical resistivity (positive TCR) due to the Kondo effect. This behavior is applied in resistance thermometers for temperature measurements below 20 K. Superconductivity occurs in intermetallic phases of Au-Ge with $2.99 < T_c < 3.16$ K and Au-Sn with $T_c = 1.25$ K [14.40, 41].

**Table 14.63** Specific electrical resistivity ($\rho_{25}$) and TCR of Au-Pd and Au-Pt alloys (after [14.2])

| Solute | | Content | | | |
|---|---|---|---|---|---|
| Content | | 80 | 60 | 40 | 30 |
| Pd | $\rho_{25}$ | 9.8 | 17 | 30 | 26 |
| | TCR | 0.88 | 0.61 | 0.45 | 1.2 |
| Pt | $\rho_{25}$ | 28 | 44 | 37 | 34 |
| | TCR | 0.28 | 0.26 | 0.82 | 0.8 |

$\mathrm{TCR}_{T_1 T_2} = \frac{1}{\rho_1} \frac{\rho_{T_2} - \rho_{T_1}}{T_2 - T_1}$

**Table 14.64** Increase of atomic electrical resistivity of Au by alloying elements $\Delta\rho/C$ ($\mu\Omega$ cm/at.%) (after [14.2])

| Base element | Alloying element | $\Delta\rho/C$ ($\mu\Omega$ cm/at.%) |
|---|---|---|
| Au | Ag | 0.35 |
| | Al | 1.9 |
| | Cd | 0.60 |
| | Co | 6.2 |
| | Cr | 4.5 |
| | Cu | 0.4 |
| | Fe | 8 |
| | Ga | 2.2 |
| | Ge | 5.5 |
| | Hg | 0.4 |
| | In | 1.4 |
| | Mn | 2.4 |
| | Mo | 4 |
| | Ni | 0.8 |
| | Pb | 3.9 |
| | Pt | 1 |
| | Rh | 3.3 |
| | Ru | 1.6 |
| | Sn | 3.5 |
| | Ti | 13 |
| | V | 13 |
| | Zn | 0.94 |

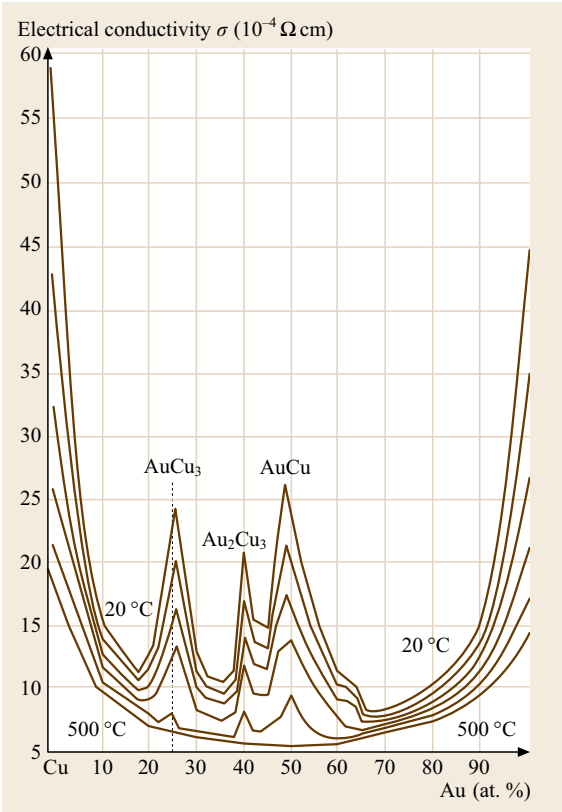


**Fig. 14.49** Specific electrical conductivity of Au-Cu alloy phases (after [14.39])

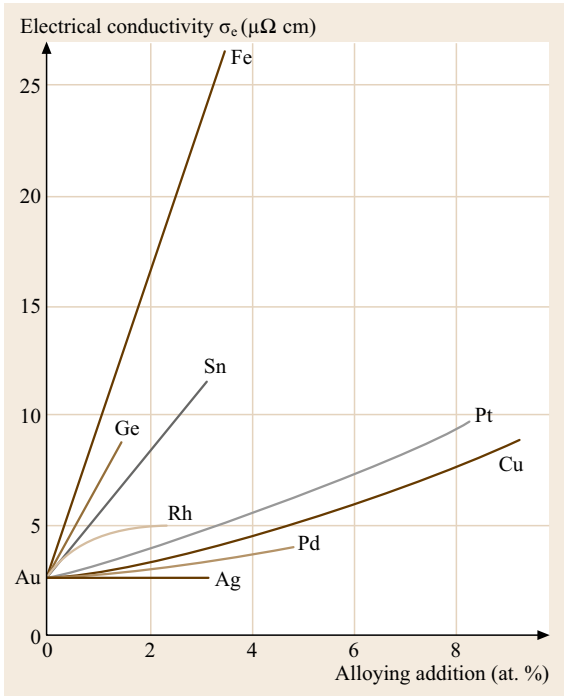


**Fig. 14.50** Influence of alloying elements on the electrical conductivity of binary Au alloys (after [14.16])

## 14.2.5 Thermoelectric Properties

Tables 14.65–14.68 [14.1] and Figs. 14.51–14.53 [14.1, 3] list the thermoelectric properties of gold and its alloys. Au-Fe and Au-Co-alloys are used in thermocouples for measuring very low temperatures [14.42], Au-Pd and Au-Pd-Pt alloys in thermocouples working under highly corrosive conditions.

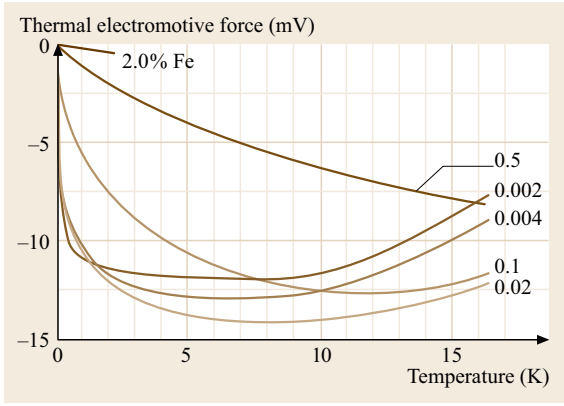


**Fig. 14.51** Thermal electromotive force of Au-Fe alloys (after [14.3]) ►

**Table 14.65** Absolute thermoelectric power of Au (after [14.43])

| Temperature (°C) | −255 | −200 | −160 | −100 | 0 | 100 | 300 | 500 | 700 |
|---|---|---|---|---|---|---|---|---|---|
| Thermoelectr. power (μV/K) | −0.93 | −0.78 | +0.80 | +1.00 | +1.1 | +1.8 | +3.1 | +3.3 | +3.7 |

**Table 14.66** Thermal electromotive force $E$ of Au and Pt at different temperatures; reference junction at 0 °C (after [14.1])

| $T$ (°C) | −200 | −100 | −50 | +100 | +200 | +400 | +800 |
|---|---|---|---|---|---|---|---|
| $E_{Au,Pt}$ (mV) | −0.39 | −0.21 | −0.10 | 0.77 | 1.834 | 4.623 | 12.288 |

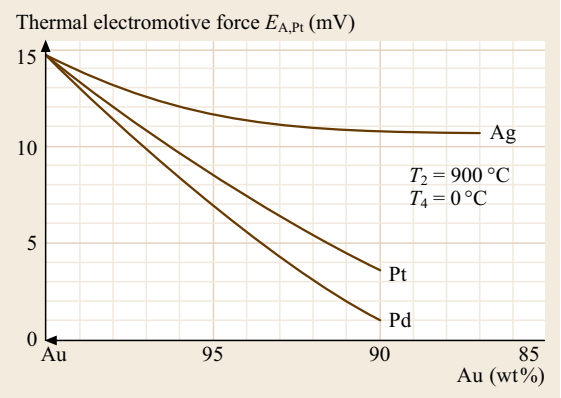


**Fig. 14.52** Thermal electromotive force of Au alloys (after [14.1])

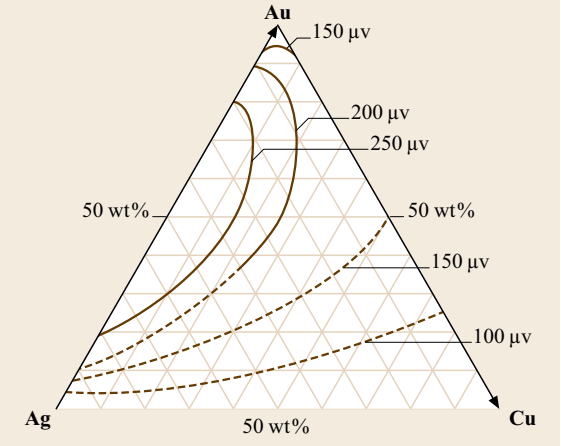


**Fig. 14.53** Thermal electromotive force of Au-Ag-Cu alloys (after [14.1])

**Table 14.67** Thermal electromotive force of Au-Fe and Au-Co-alloys (after [14.1])

| $T_1$ (K) | $T_2$ (K) | Au-$Co_{2.1}Cu$ (at.%) | Au-$Fe_{0.02}Cu$ (at.%) |
|---|---|---|---|
| 4.2 | 10 | 0.044 | 0.093 |
| 4.2 | 20 | 0.173 | 0.208 |
| 4.2 | 40 | 0.590 | 0.423 |

**Table 14.68** Thermocouples for very low temperatures (after [14.1])

| Thermocouple | Temperature range |
|---|---|
| AuFe (0.03 at.% Fe)/chromel | From 4.2 to 273 K |
| AuCo (2.11 at.% Co)/AuAg (0.37 at.% Ag) or Cu | From 240 to 0 °C |
| AuFe (0.02 at.% Fe)/Cu | From −270 to −230 °C |

## 14.2.6 Magnetic Properties

Figure 14.54 [14.2] illustrates the metal's magnetic properties. Gold is diamagnetic. The magnetic susceptibility remains constant from 0 K to the melting point. Alloying of gold with B metals causes only weak variations compared to pure gold. In the range of continuous solid solutions, the molar susceptibilities remain negative, the alloys are diamagnetic. Ni, Pd, and Pt dissolve diamagnetically up to 25 at.%. Cr, Fe, and Mn give rise to paramagnetism. Magnetic transformations are reported for Au-Co alloys between ≈ 18 and 92 wt% Co at 1122 °C and for Au-Ni alloys between ≈ 3 and 95 wt% at ≈ 340 °C [14.44].

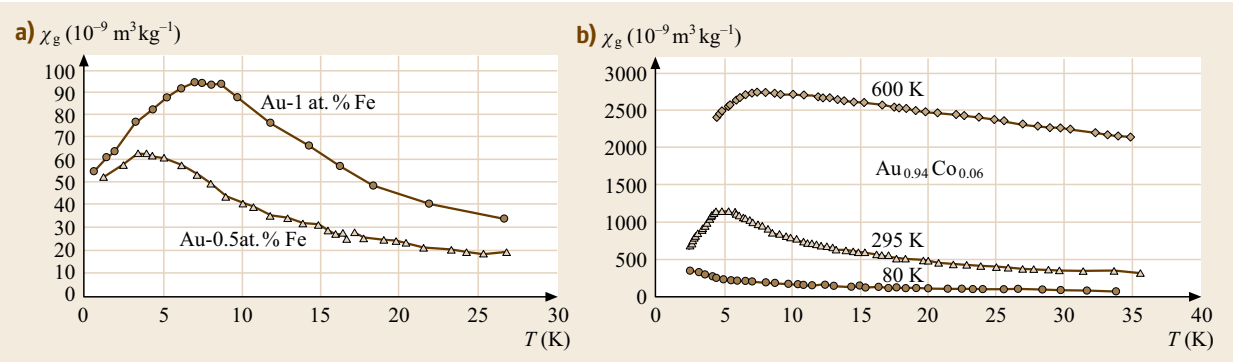


**Fig. 14.54a,b** Magnetic susceptibility of **(a)** Au-Fe and **(b)** Au-Co alloys (after [14.2])

### 14.2.7 Thermal Properties

Data for thermal expansion and thermal conductivity of Au and Au alloys are listed in Tables 14.30, 14.31, and 14.34. Table 14.69 [14.2] shows the recrystallization temperatures of gold of different purity. After 90% cold work, the hardness decreases by about 50%.

### 14.2.8 Optical Properties

For the optical properties of colored Au alloys, see Tables 14.36 and 14.37 and Figs. 14.55–14.58 [14.45–48]. The reflectivity of gold shows a marked decrease at $\approx 550\,\text{nm}$ in the visible range with a minimum of $R \approx 0.25$ in the near ultraviolet. Interband transitions occur at $\approx 2.17\,\text{eV}$. The reflected light contains all wavelengths above 550 nm, which accounts for the typical gold color.

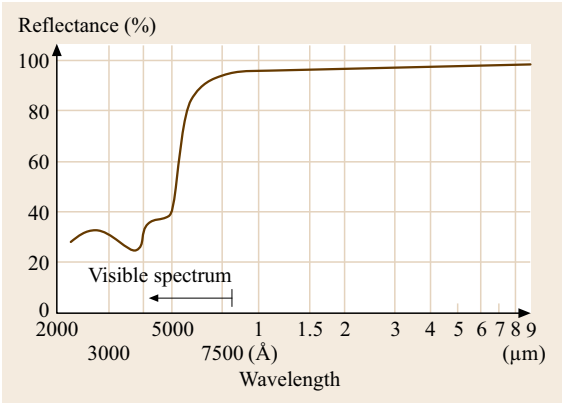


**Fig. 14.55** Reflectance as a function of wavelength of pure Au (after [14.45])

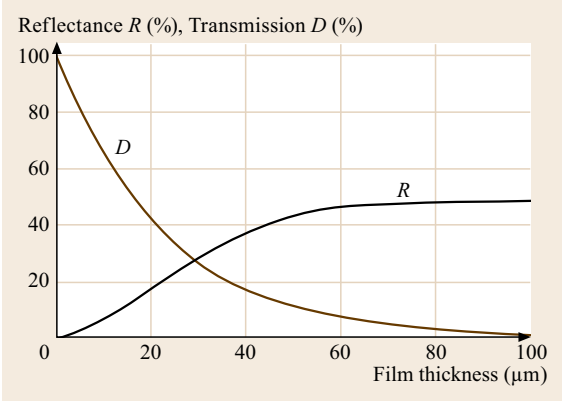


**Fig. 14.56** Reflectance and transmission of thin Au films at $\lambda = 492\,\mu\text{m}$ (after [14.45])

**Table 14.69** Recrystallization temperatures of Au 3N, 4N and 5N purity (after [14.2])

| Purity (%) | Decrease of hardness | |
|---|---|---|
| | 50% $T_{\text{recryst.}}$ (°C) | 100% $T_{\text{recryst.}}$ (°C) |
| 99.9 (3N) | 200 | |
| 99.99 (4N) | 160 | 200 |
| 99.999 (5N) | 112 | 149 |

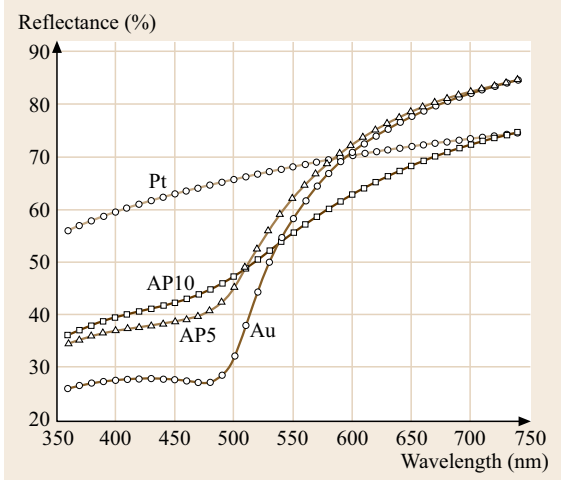


**Fig. 14.57** Reflectance–wavelength curves for Au-Pt and binary Au-Pt alloys (after [14.46])

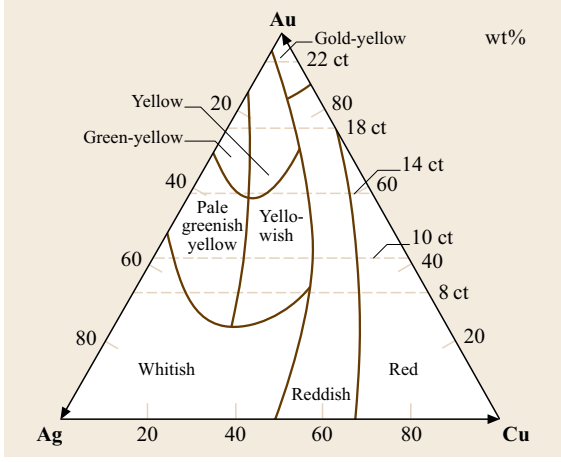


**Fig. 14.58** Color ranges of Au-Ag-Cu alloys (after [14.47])

### 14.2.9 Diffusion

Characteristic data are shown on Tables 14.38, 14.39, and 14.41–14.43 and Figs. 14.22 and 14.59 [14.2, 23].

### 14.2.10 Chemical Properties

Figures 14.60 and 14.61 show that gold has the reduction potential of $E_0 = +1.42\,V$ for $Au/Au^{3+}$. At room temperature it is resistant against dry and wet atmospheres, $H_2O$, $O_2$, F, I, S, alkali, non-oxidizing acids, and ozone below 100 °C. It is dissolved in $3\,HCl + 1\,HNO_3$, $HCl + Cl_2$ in acid concentration above 6 mol/l, in $NaCN/H_2O/O_2$, and other oxidizing solutions. Halogens generally attack gold, except for dry fluorine below 300 °C. Gold alloys are corrosion-resistant against acids if the base metal content is lower than 50% and also if each base metal present contains more than 50% of noble metal. Detailed information of chemical properties of Au and Au alloys are given in [14.2].

Gold and gold alloys (with Ag, Ir, Pt) and cationic gold (I) phosphines act as selective catalysts in hydrogenation, oxidation, and reduction reactions [14.49–51]. Nanometer-sized Au particles (≈ 5 nm) in the presence of ceria or a transition-metal oxide have superior catalytic activities [14.52–54].

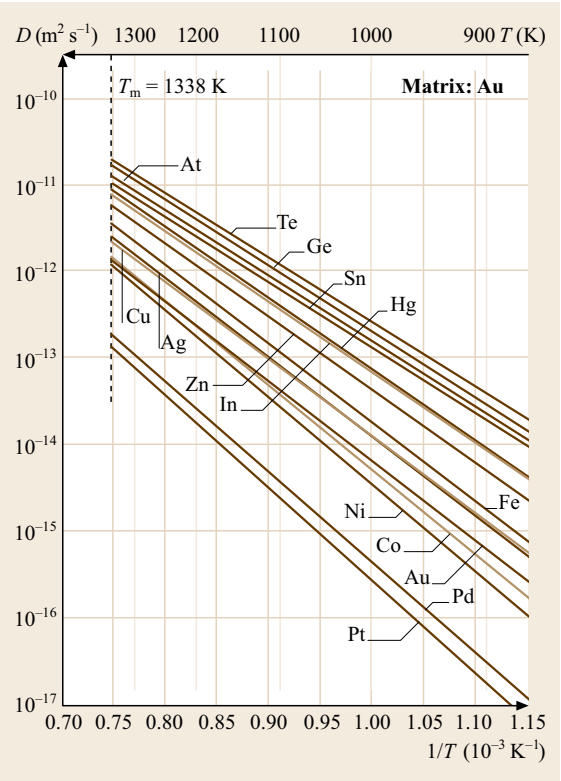


**Fig. 14.59** Diffusion of impurities in Au (after [14.23])

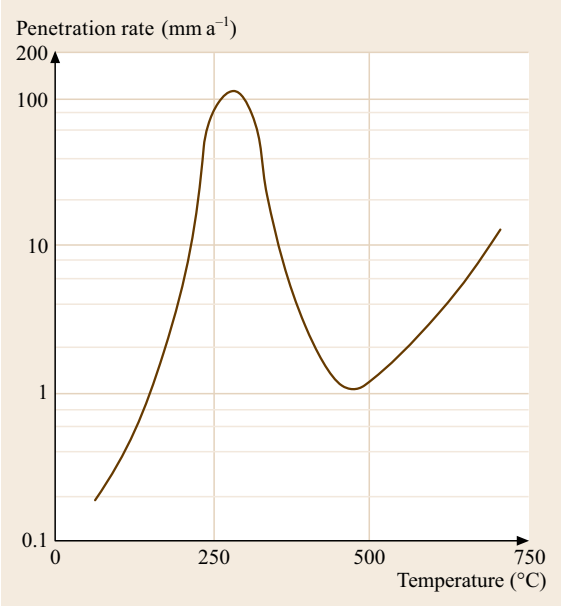


**Fig. 14.60** Corrosion of gold in dry chlorine gas (after [14.2])

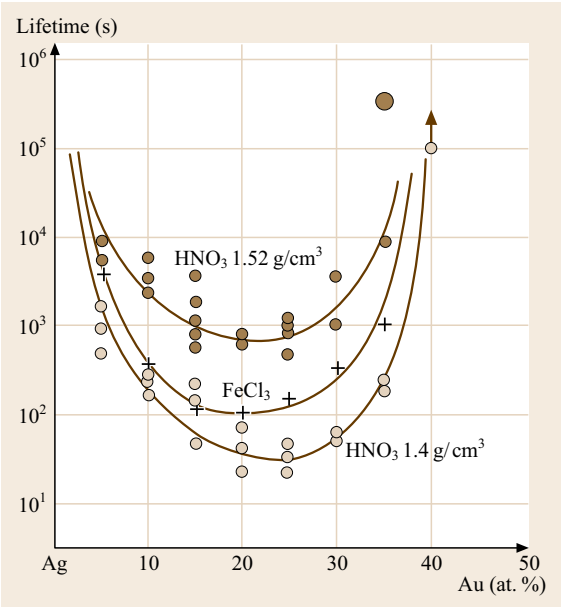


**Fig. 14.61** Lifetime of Ag-Au solid solutions in $HNO_3$ and $FeCl_3$ solution (after [14.2])

**Table 14.70** Physical properties of the eutectic alloys Au20Sn, Au12Ge, and Au3Si (after [14.55])

| Composition (wt%) | Melting point (°C) | Young's modulus (GPa) versus temperature | | | | Thermal conductivity (W/(m K)) | Coefficient of thermal expansion (ppm/°C) |
|---|---|---|---|---|---|---|---|
| | | −60 °C | 23 °C | 100 °C | 150 °C | | |
| Au20Sn | 280 | 59.5 | 59.2 | 48.5 | 35.8 | 57.3 | 15.93 ± 0.88 (−50−170) |
| Au12Ge | 356 | 69.8 | 69.3 | 68.2 | 62.7 | 44.4 | 13.35 ± 3.13 (10−250) |
| Au3Si | 363 | 77.0 | 83.0 | 82.8 | 83.0 | 27.2 | 12.33 ± 0.86 (10−250) |

## 14.2.11 Special Alloys

### Binary Alloys

The material Au–20 wt% Ag is used for low-voltage electrical contacts. Gold–copper alloys form the ordered phases $Au_3Cu$ [60748-60-9], AuCu [12006-51-8], and $AuCu_3$ [12044-96-1]. Gold–nickel alloys decompose into gold-rich and nickel-rich solid solution phases in a miscibility gap below 800 °C. The alloy Au–18 wt% Ni is a structural material for turbine blades in jet engines and nuclear and space technology materials.

Alloys of Au-Co(Fe,Ni) with 1−3 wt% Co, Fe, or Ni serve as hard and wear-resistant surface coatings on electrical contacts. The gold-cobalt alloy of Au–5 wt% Co is resistant against silver migration. The gold-platinum alloy of Au–10 wt% Pt is used for electrical contacts working under highly corrosive conditions. The high Pt content alloy Au–30 wt% Pt serves as a material for spinnerets for rayon and as a high-melting platinum solder ($T_{liquidus}$ = 1450 °C, $T_{solidus}$ = 1228 °C), additions ≈ 0.5% of Rh, Ru, or Ir suppress segregation. Gold–Platinum alloys containing 40−65 wt% Au harden by quenching from 1100 °C and annealing at 500 °C to yield strengths up to ≈ 1400 N/mm². Au–1 wt% Ti (Figs. 14.33 and 14.42 [14.30, 36, 55, 56]) is of importance for bonding wires, electrical conductors, and as hard high-carat gold alloy for jewelry. Strengthening can be induced by precipitation of the intermetallic compound $Au_4Ti$ and by formation of highly-dispersed Ti oxide on annealing in an oxidizing atmosphere. The alloys Au–12 wt% Ge, Au–3.1 wt% Si, and Au–20 wt% Sn are low melting eutectic solders of high strength, corrosion resistance and stability against temperature cycling, used for the hermetic sealing of electronic devices (Table 14.70 [14.55]).

**Table 14.71** Basic compositions of gold-based jewelry alloys (after [14.34])

| Colored gold fineness | Ag (wt%) | Cu (wt%) | |
|---|---|---|---|
| 750 | 0−20 | 5−25 | |
| 585 | 5−35 | 5−35 | |
| 375 | 5−15 | 45−50 | |
| (333) | 5−40 | 25−60 | |
| **White gold fineness** | **Ag (wt%)** | **Cu (wt%)** | **Pd (Ni) (wt%)** |
| 750 | 0−10 | 0−10 | 10−20 |
| 585 | 0−25 | 5−30 | 5−20 |
| 375 | 0−35 | 5−50 | 5−20 |
| (333) | 0−35 | 10−50 | 5−25 |
| Zinc max. 20%, tin, indium, and gallium each max. 4% | | | |

### Ternary and Higher Alloys

Au-Ag-Cu, Au-Ag-Ni and Au-Ag-Pd alloys are of major importance for jewelry and dentistry (Tables 14.71 and 14.72) [14.34, 35]. The microstructures and thus the mechanical properties are determined by wide miscibility gaps. Additions of Zn and In serve to adjust the melting ranges. The high-carat Au alloy AuSb0.3Co0.2 can be hardened by cold working and precipitation annealing to 142 HV 5 (Fig. 14.43) [14.38].

AuAg25Pt5, AuAg26Ni3, and AuCu14Pt9Ag4 are used for electrical contacts working under highly corrosive conditions. AuNi22Cr6 is a hard solder of high mechanical stability [14.16]. Au-Ag-Ge alloys of various compositions are solders applicable under $H_2$, Ar, or vacuum in melting ranges between 400 and 600 °C. Additions of 0.5−2 wt% Pd, Cd, or Zn improve their ductility [14.56, 57].

**Table 14.72** Basic compositions of noble-metal-based dental alloys (after [14.35])

| Noble metal base | Most common alloying elements |
|---|---|
| **Crown and bridge alloys** | |
| Au | Ag, Cu, Pt, Zn |
| Au-Ag | Pd, Cu, Zn, In |
| Ag-Pd | Cu, In, Au, Zn |
| **Porcelain fused to metal alloys** | |
| Au | Pt, Pd, In, Sn |
| Au-Pd | Sn, In, Ga, Ag |
| Pd | Cu, Ga, Sn, In |
| Pd-Ag | Sn, In, Zn |

## 14.3 Platinum Group Metals and Their Alloys

Characteristic properties of the platinum-group metals (PGM) Pd, Pt, Rh, Ir, Ru, and Os are their high chemical stability, mechanical strength, thermoelectric and magnetic behavior, and their catalytic activities in heterogeneous and homogeneous chemical reactions, automobile exhaust gas purification, and the stereospecific synthesis of enantiomeric compounds. Their melting temperatures, $T_m(\mathrm{Os}) = 3045\,^\circ\mathrm{C}$, $T_m(\mathrm{Pd}) = 1554\,^\circ\mathrm{C}$, hardness, brittleness, and the recrystallization temperatures decrease with increasing nuclear charge, while their thermal expansion and ductility increase.

The catalytic properties of the PGM in the heterogeneous catalysis are based on the moderate values of the heats of adsorption which correspond to the dissociation energies of the reactant molecules. Figure 14.62 [14.58] and Table 14.73 [14.3] give some values of the heat of adsorption and binding energies between adsorbates and surface atoms on various noble metal single crystals. The heat of adsorption increases for different orientations of the crystal surface planes of the fcc crystals in the order (111) < (100) < (110) (Table 14.74 [14.3]). The catalytic activities are element-specific for different reactions. Reactivity and selectivity of the reactions are presumably controlled by the dimensional fit between adsorbed molecules and catalyst surface, and the alloy composition. A survey of PGM catalyst activities is given in [14.2, 3, 28].

All platinum metals are paramagnetic ($\chi > 0$). The magnetic susceptibilities of palladium and platinum decrease with increasing temperature, the magnetic susceptibilities of rhodium, iridium, ruthenium, and osmium increase with increasing temperature (Fig. 14.83 [14.3]).

The platinum group metals occur jointly as alloys and as mineral compounds in placer deposits of varying compositions. Ru and Os are separated from the PGM mix by distillation of their volatile oxides, whereas platinum, iridium, palladium, and rhodium are separated by repeated solution and precipitation as complex PGM chlorides, or by solvent extraction and thermal decomposition to sponge or powder. PGM scrap is recycled by melting with collector metals (lead, iron, or copper) followed by element-specific extraction.

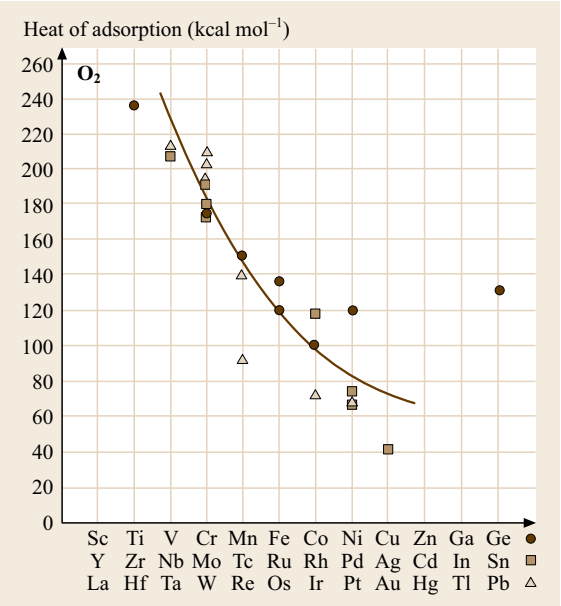


**Fig. 14.62** Heat of adsorption of molecular oxygen on polycrystaline transition metal surfaces (after [14.3])

### 14.3.1 Palladium and Palladium Alloys

Palladium and palladium alloys are important constituents of catalysts of chemical reactions and automobile exhaust gas cleaning, of electrical contacts, capacitors, permanent magnetic alloys, thermocouples, and for the production of high purity hydrogen. The low thermal neutron cross section permits their use in solders and brazes of nuclear structural parts. Classical applications are jewelry and dentistry alloys.

Commercial grades of palladium are sponge and powder in purities of 99.9 to 99.95–99.98 wt% (ASTM (B 589-82)). High purity electronic grade is 99.99 wt%.

**Table 14.73** Binding energies between adsorbates and surface atoms on noble metal single crystals (after [14.3])

| Precious metals | Binding energy (kcal/mol) | | | | |
|---|---|---|---|---|---|
| | N | O | H | CO | NO |
| Ru(0001) | | | 61 | 29 | |
| Ir(111) | 127 | 93 | 63 | 34 | 20 |
| Pd(111) | 130 | 87 | 62 | 34 | 31 |
| Pt(111) | 127 | | 57 | 30 | 27 |
| Ag(111) | | 80 | | 6.5 | 25 |

**Table 14.74** Heat of adsorption of diatomic molecules on different single crystals planes of various transition metals (after [14.3])

| Adsorption system | Heat of adsorption (kcal/mol) | | |
|---|---|---|---|
| | (111) | (100) | (110) |
| $O_2$/Pd | 50 | 55 | 80 |
| Co/Ni | 27 | 30 | 30 |
| Co/Pd | 34 | 37 | 40 |
| Co/Pt | 30 | 32 | 32 |
| $H_2$/Pd | 21 | | 24 |
| $H_2$/W | 37 | 33 | 35 |
| $N_2$/Fe | 51 | 53 | 49 |

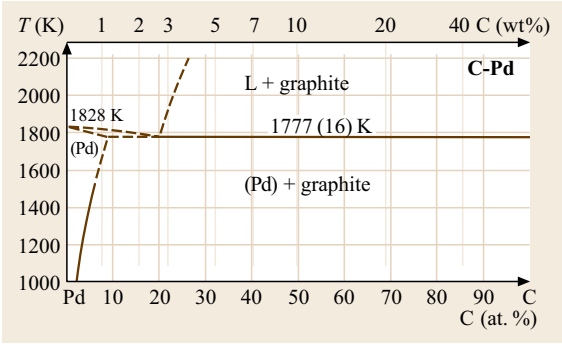


**Fig. 14.63** Binary phase diagram: Pd-C (after [14.4])

### Production

Palladium sponge or powder are compacted by pressing and sintering. Melting and alloying is performed in electrical heated furnaces, vacuum arc, or by electron beam melting. Crucible materials are $Al_2O_3$ and MgO.

### Phases and Phase Equilibria

Selected phase diagrams are shown in Figs. 14.63–14.67 [14.4]. Pd forms continuous solid solutions with all other noble metals and with Co, Cu, Fe, and Ni. Miscibility gaps exist in alloys with C, Co, Ir, Pt, Rh, and ternary Pd-Ag-Cu alloys (Fig. 14.68) [14.5]. All PGMs lower the $\gamma-\alpha$ transition temperature in Fe-alloys considerably (Fig. 14.153). Thermodynamic data are given in Tables 14.75–14.80. Numerous intermediate phases exist also in alloys with rare earth metals [14.1, 2, 7]. The solubility of carbon rises from 0.04 wt% at 800 °C to 0.45 wt% at 1400 °C, with the hardness increasing from 80 to 180 $HV_{25\,g}$ [14.58]. The continuous series of solid solutions of Pd-H-alloys (Fig. 14.69) [14.58] splits up below 295 °C into a fcc palladium-rich $\beta$ phase and an fcc hydrogen-rich phase, forming a miscibility gap which broadens with decreasing temperature.

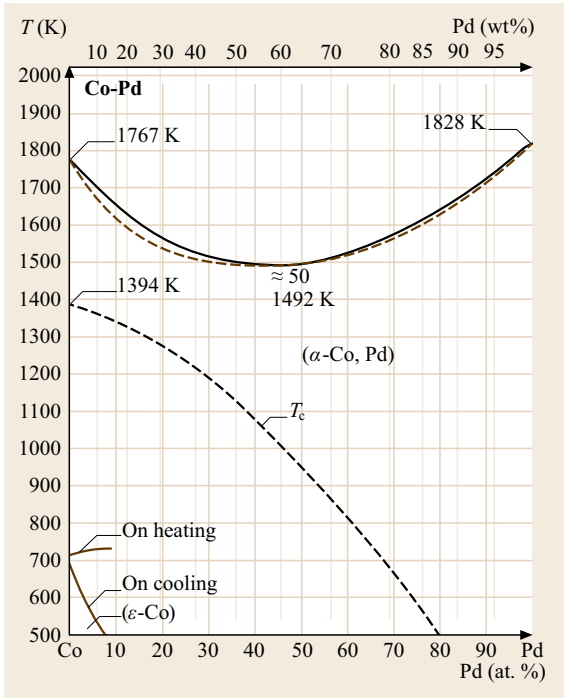


**Fig. 14.64** Binary phase diagram: Pd-Co (after [14.4])

The equilibrium hydrogen-pressure at 295 °C amounts to 19.87 atm with 21 at.% hydrogen. The $\alpha$-phase takes hydrogen up to 1300 times of the volume of palladium, corresponding 50 at.% hydrogen. Further quantities up to 2800 times of the Pd-volume can be loaded by cathodic deposition. The lattice parameters increase with increasing hydrogen content from 3.891 to 4.06 A at 75 at.% hydrogen. The dissolved hydrogen moves easily and diffuses quickly through thin Pd-membranes. This effect is used for the production of high-purity Pd and for the separation of H isotopes.

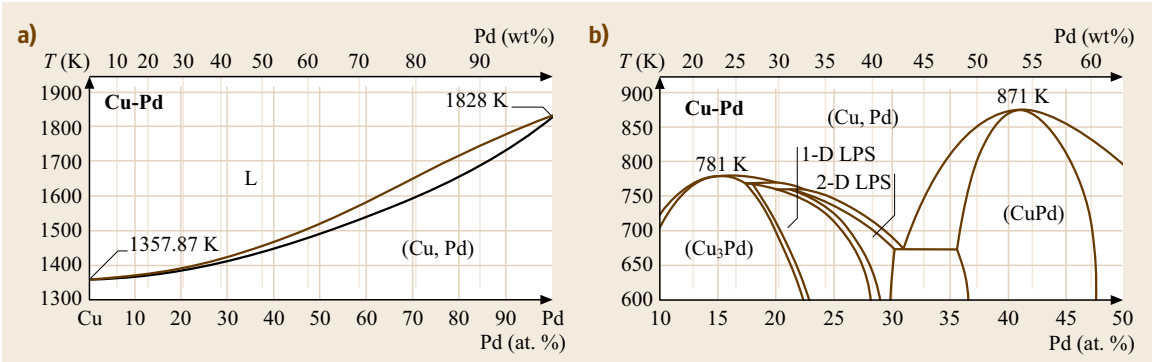


**Fig. 14.65a,b** Binary phase diagrams: Pd-Cu. **(a)** liquid–solid equilibrium; **(b)** low temperature (600–900 °C). 1D-LPS = one-dimensional long-period superstructure; 2D-LPS = two-dimensional long-period superstructure (after [14.4])

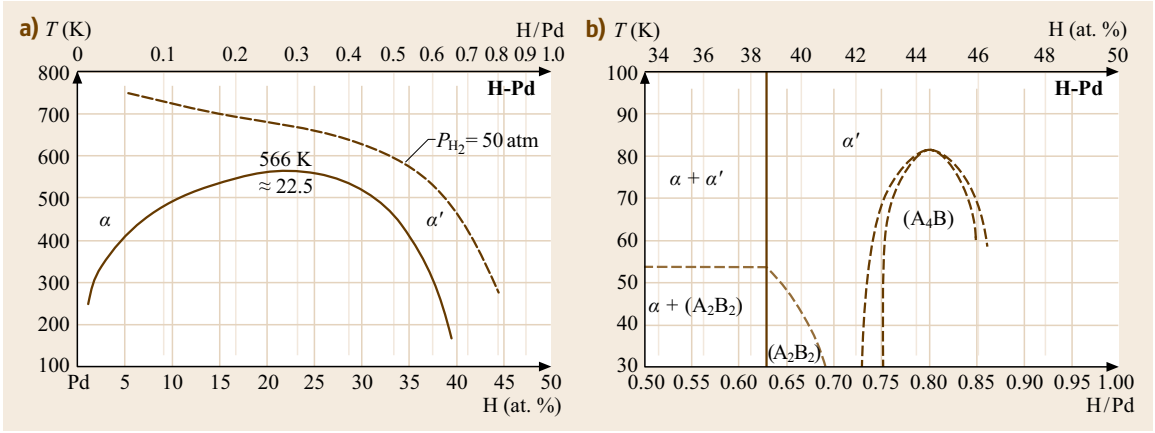


**Fig. 14.66a,b** Binary phase diagrams: Pd-H. **(a)** Phase diagram; **(b)** low temperature phase (after [14.4])

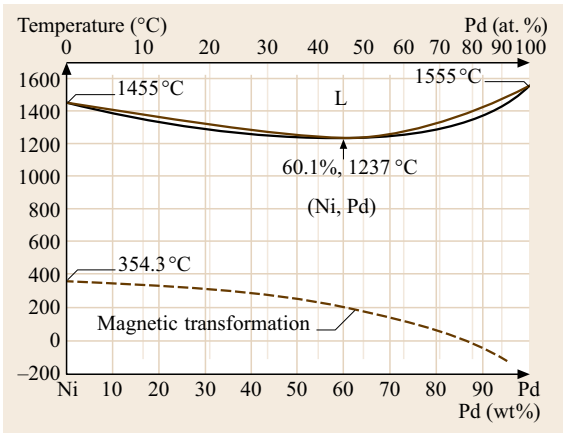


**Fig. 14.67** Binary phase diagram: Pd-Ni (after [14.4])

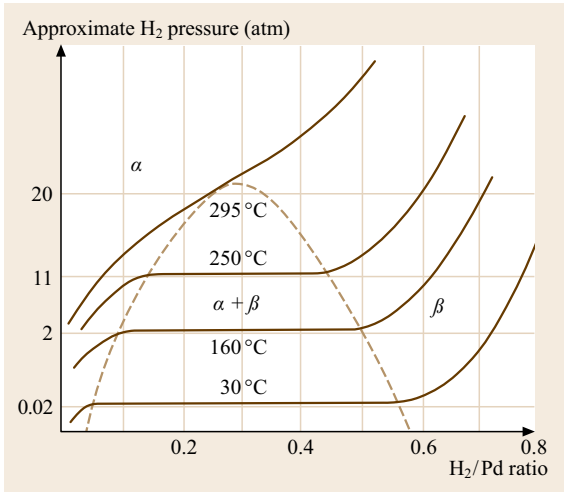


**Fig. 14.69** Hydrogen pressure in the Pd-H system (after [14.59])

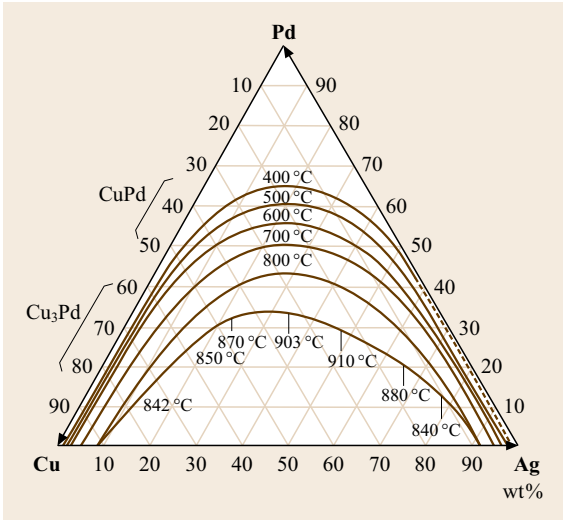


**Fig. 14.68** Miscibility gap in the Pd-Ag-Cu alloy system (after [14.5]) ◄

**Table 14.75** Molar heat capacities of solid PGMs (after [14.7])

| Element | $c_p = 4.1868(a + 10^{-3}bT + 10^{-5}cT^2)$ J/K | | | |
|---|---|---|---|---|
| | *a* | *b* | *c* | Temperature range (K) |
| Ir | 5.56 | 1.42 | – | 298–1800 |
| Os | 5.69 | 0.88 | – | 298–1900 |
| Pd | 5.80 | 1.38 | – | 298–1828 |
| Pt | 5.80 | 1.28 | – | 298–2043 |
| Rh | 5.49 | 2.06 | – | 298–1900 |
| Ru | 5.20 | 1.50 | – | 298–1308 |
| Ru | 7.20 | – | – | 1308–1773 |
| Ru | 7.50 | – | – | 1773–1900 |

**Table 14.76** Latent heat and temperatures of transition of Pd and Pt intermediate compounds (after [14.7])

| Phase | $N_2$ | Transition | $T_t$ (°C) | $L_t$ (J/g-at.) |
|---|---|---|---|---|
| CuPt | 50 | Order–disorder | 800 | 3810 |
| $Cu_3Pt$ | 20 | Order–disorder | 610 | 1968 |
| $Pd_3Sb$ | 25 | Order–disorder | 950 | 10 300 |

$T_t$ = transition temperature, $L_t$ = latent heat of transition

**Table 14.77** Thermodynamic data of Pd (after [14.2])

| *T* (K) | $c_p$ (J/(K mol)) | *S* (J/(K mol)) | *H* (J/mol) | *G* (J/mol) | *p* (at) |
|---|---|---|---|---|---|
| 298.15 | 25.99 | 37.823 | 0 | −11.277 | $5.97 \times 10^{-60}$ |
| 400 | 26.706 | 45.568 | 2.686 | −13.541 | $3.65 \times 10^{-43}$ |
| 600 | 27.768 | 56.602 | 8.136 | −25.825 | $8.92 \times 10^{-27}$ |
| 800 | 28.827 | 64.733 | 13.704 | −37.903 | $1.11 \times 10^{-18}$ |

*T* = temperature, $c_p$ = specific heat capacity, *S* = entropy, *H* = enthalpy, *G* = free enthalpy
*p* = partial pressure of the pure elements

**Table 14.78** Enthalpy of formation $H_T$ of Pd and Pt alloys at temperatures of reaction (after [14.1])

| | Concentration of alloying metal in at.% [ETA 89] | | | | | |
|---|---|---|---|---|---|---|
| Base metal | Alloy comp. | Temp. (K) | 20 at.% | 40 at.% | 60 at.% | 80 at.% |
| Enthalpy of formation $H_T$ | | | | | | |
| Pd | Ag | 915 | | | | 1050 |
| | | 1200 | 283 | 897 | 1290 | 887 |
| Pt | Co | 914 | 1680 | 2580 | | |
| | Cu | 1625 | 3110 (30%) | | 3375 | 1950 (90%) |
| | Fe | 1123 | −680 | 0 | 1600 | 1800 |

**Table 14.79** Maximum hydrogen inclusion by platinum-group metals (after [14.2])

| Element | Max. $H_2$ (ml/g) | Composition |
|---|---|---|
| Ru | 123 | $RuH_{1.1}$ |
| Rh | 24 | $RhH_{0.2}$ |
| Pd | 75 | $PdH_{0.7}$ |
| Os | 75 | $OsH_{1.2}$ |
| Ir | 35 | $IrH_{0.6}$ |
| Pt | 2.4 | $PtH_{0.04}$ |

**Table 14.80** Structure and lattice parameters of selected intermediate Pd compounds (after [14.2])

| Phase | Pearson symbol | $a$ (nm) | $b$ (nm) | $c$ (nm) | $c/a$ | Remarks | Concentration $x$ $A_{1-x}B_x$ |
|---|---|---|---|---|---|---|---|
| C-Pd | *cF*4 | 0.3735 | | | | | 0.97 |
| Co-Pd | *cF*4 | 0.3735 | | | | | |
| Cu-Pd | *cF*4 | 0.377 | | | | HT | 0.5 |
| $Cu_3Pd$ | *tP*4 | 0.3701 | 0.3666 | 0.9905 | | | |
| $Cu_3Pd$ | *tP*28 | 0.371 | 2.5655 | 6.9151 | | | 0.19 |
| Fe-Pd | *cF*4 | 0.38873 | | | | | 0.936 |
| FePd | *tP*4 | 0.386 | | 0.3731 | 0.9666 | | |
| $FePd_3$ | *cP*4 | 0.3851 | | | | | |
| $H_3Pd_5$ | *cF** | 0.4018 | | | | | |
| $H_4Pd_3$ | *cP** | 0.2995 | | | | HT > 923 K | |
| $H_4Pd_3$ | *tP*4 | 0.2896 | | 0.333 | 1.1499 | | |
| Ni-Pd | *cF*4 | 0.373 | | | | 298 K | 0.474 |
| $Pd_3Zr$ | *hP*16 | 0.5612 | | 0.9235 | 1.6456 | | |

HT = high temperature modification

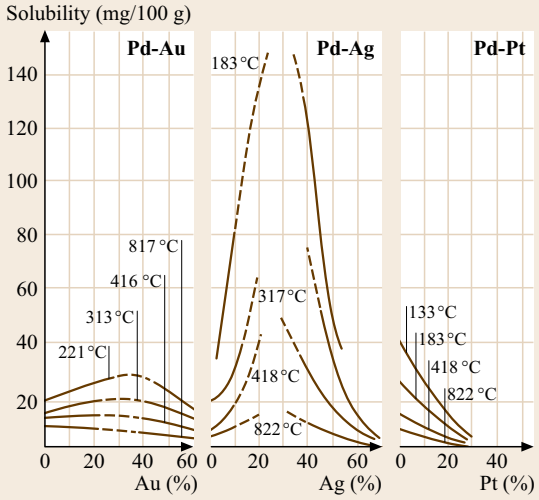


**Fig. 14.70** Solubility of hydrogen at 1 atm in Pd-Au, Pd-Ag, and Pd-Pt alloys (after [14.60])

Thermal cycling of Pd-H-alloys in the duplex phase causes brittleness due to stresses generated by changes of the lattice dimensions for different quantities of dissolved hydrogen. Palladium-silver alloys with 20–25 wt% silver dissolve higher amounts of hydrogen than pure palladium (Fig. 14.70).

For composition and crystal structures, see Tables 14.80 and 14.81 [14.2, 4, 58]. Primary solid solutions have the fcc structure of Pd. The lattice parameters correspond with few exceptions roughly to Vegard's law. Superlattices occur in alloys with Cu, Fe, Nb, and V in atomic ratios from 1 : 1, 2 : 1, and 3 : 1 (Tables 14.8 and 14.82).

**Table 14.81** Structures of platinum-group metal oxides (after [14.4, 58])

| Oxide | Structure type | Unit cell dimensions (Å) | | |
|---|---|---|---|---|
| | | $a$ | $b$ | $c$ |
| $\alpha$-$PtO_2$ | Primitive hexagonal | 3.08 | | 4.19 |
| $\beta$-$PtO_2$ | Primitive orthorhombic | 4.486 | 4.537 | 3.138 |
| $Pt_3O_4$ | Primitive cubic | 5.585 | | |
| PdO | Tetragonal | 3.043 | | |
| PdRhO | Hexagonal | 5.22 | | 6.0 |
| $Rh_2O_3$ (LT) | Hexagonal (corundum) | 5.108 | | 13.87 |
| $Rh_2O_2$ | Tetragonal (rutile) | 4.4862 | 3.0884 | |
| PdO | Tetragonal | 3.03 | | 5.33 |
| $PdO_2$ | Tetragonal (rutile) | 4.483 | | 3.101 |

LT = low temperature modification

**Table 14.82** Superlattice structures of the platinum-group metals (after [14.61])

| Ordered structure type | Examples |
|---|---|
| Tetragonal ($L1_0$-type) | CdPt, CoPt, $Cu_4Pd$, FePd, FePt, MnPt, NiPt |
| Face-centered cubic ($L1_2$-type) | $CoPt_3$, $Cu_3Pt$, $FePd_3$, $FePt_3$, $Fe_3Pt$, $MnPt_3$, $Ni_3Pt$ |
| Body-centered cubic (B2-type) | BePd, CuPd, FeRh, RhSc, RhTi |
| Rhombohedral ($L1_1$-type) | CuPt (unique) |
| Close-packed hexagonal ($DO_{19}$-type) | $Pt_3U$ |

Ordered $A_3B$-phases of Pd-Mn and Pd-Fe alloys show higher solubility for hydrogen than the disordered phases. In Pd-Mn alloys, hydrogen uptake lowers the temperature of the ordering process.

### Mechanical Properties

Characteristic data are shown in Tables 14.83–14.87 and Figs. 14.71–14.77 [14.2, 5, 16, 58]. At room temperature Pd is very ductile and can be easily rolled or drawn to form a sheet, foil, and wire. The recrystallization temperatures (Table 14.97) depend on purity grade, degree of cold forming and annealing time. Strengthening is affected by solid solution and by order hardening in alloys, forming superlattice structures. Solid solution hardening is also effected by alloying with rare earth metals in concentrations of 0.1–0.6 at.%.

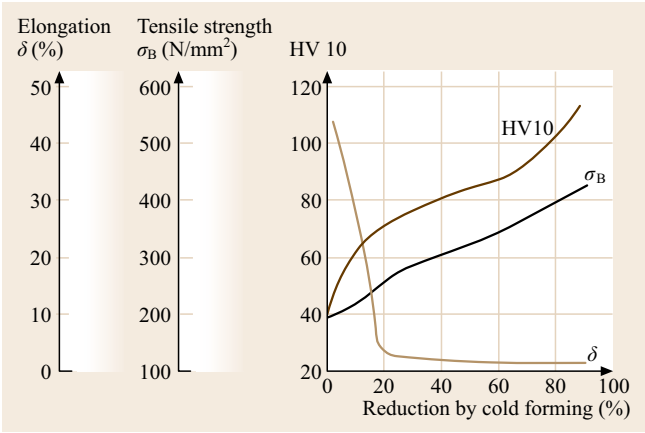


**Fig. 14.71** Work hardening of Pd (99.99%) (after [14.16])

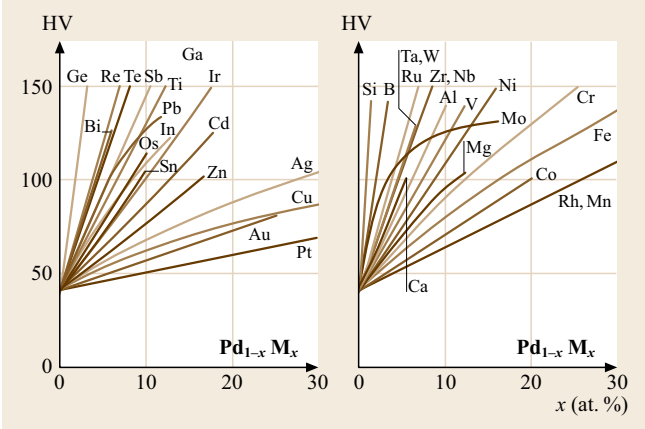


**Fig. 14.72** Solid solution hardening of Pd by various elements (after [14.2])

**Table 14.83** Modulus of elasticity in crystal directions (GPa) (after [14.2])

| $E\langle 100\rangle$ | $E\langle 110\rangle$ | $E\langle 111\rangle$ |
|---|---|---|
| 65 | 129 | 186 |

**Table 14.84** Elastic constants of Pd (after [14.2])

| $T$ (°C) | $c_{11}$ | $c_{12}$ | $c_{14}$ |
|---|---|---|---|
| −273 | 234.1 | 176.1 | 71.2 |
| 7 | 226.2 | 175.2 | 71.5 |

**Table 14.85** Mechanical properties of Pd (99.9%) at different temperatures (after [14.2])

| $T$ (°C) | $E$ (GPa) | $R_m$ (MPa) | $A$ (%) | $R_{p0.2}$ (MPa) | HV |
|---|---|---|---|---|---|
| 20 | 124 | 190 | 25 | 50 | 50 |
| 250 | 121 | 180 | 16 | 90 | 47 |
| 500 | 117 | 68 | 94 | 50 | 39 |
| 750 | 98 | 28 | 42 | 20 | 17 |

$A$ = Elongation, $E$ = modulus of elasticity, $R_p$ = limit of proportionality, HV = Vickers hardness, $R_m$ = tensile strengh

**Table 14.86** Tensile strength (MPa) of binary Pd and Pt alloys (after [14.2])

| Alloying element | Weight % of alloying element | | | | | |
|---|---|---|---|---|---|---|
| | 2 | | 5 | | 10 | |
| | Pd | Pt | Pd | Pt | Pd | Pt |
| Ag | 230 | 370 | 270 | 550 | 310 | 830 |
| Au | 200 | 200 | 220 | 320 | 230 | 540 |
| Co | 190 | 360 | 210 | – | 270 | – |
| Cu | 240 | 290 | 280 | 400 | 300 | – |
| Fe | 200 | 360 | 230 | – | 340 | – |
| Ni | 190 | 260 | 219 | 450 | 270 | 640 |
| Pd | – | 170 | – | 190 | – | 200 |
| Pt | 200 | – | 220 | – | 240 | – |
| Rh | 230 | 170 | 290 | 230 | 380 | 330 |
| Ru | 230 | 250 | 350 | 380 | – | 550 |

**Table 14.87** Mechanical properties of Pd by cold forming as a function of reduction in thickness $V$ (after [14.2])

| $V$ (%) | $R_m$ (MPa) | $A$ (%) | HV |
|---|---|---|---|
| 0 | 220 | 60 | 50 |
| 20 | 250 | 170 | 80 |

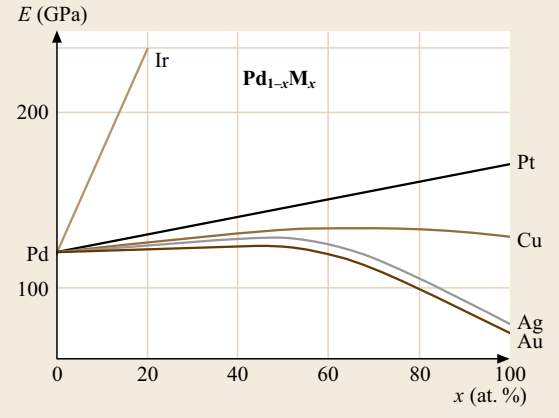


**Fig. 14.73** Modulus of elasticity of binary Pd alloys (after [14.2])

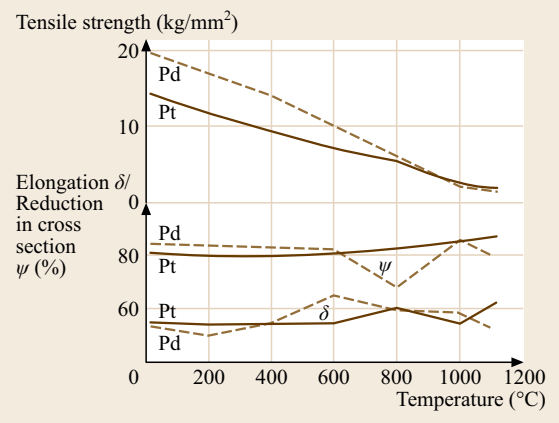


**Fig. 14.74** Tensile strength of Pd and Pt at different temperatures (after [14.5])

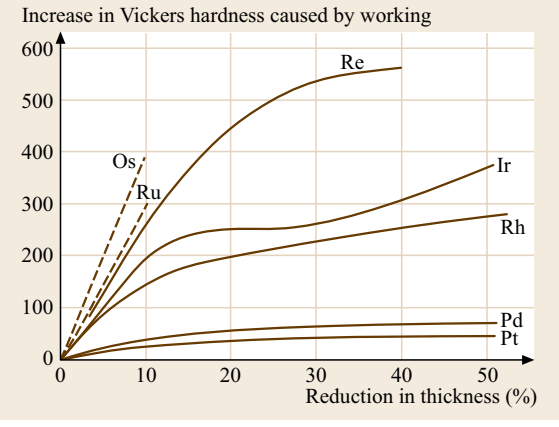


**Fig. 14.75** Work hardening of the platinum group metals (after [14.58])

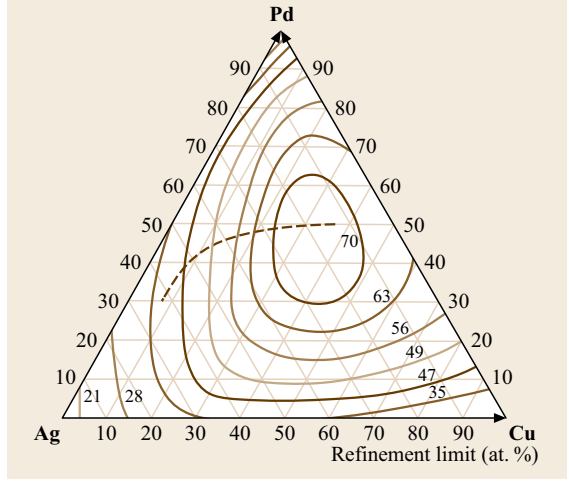


**Fig. 14.76** Tensile strength of Pd-Ag-Cu alloys. *Dashed line*: refinement limit (after [14.5])

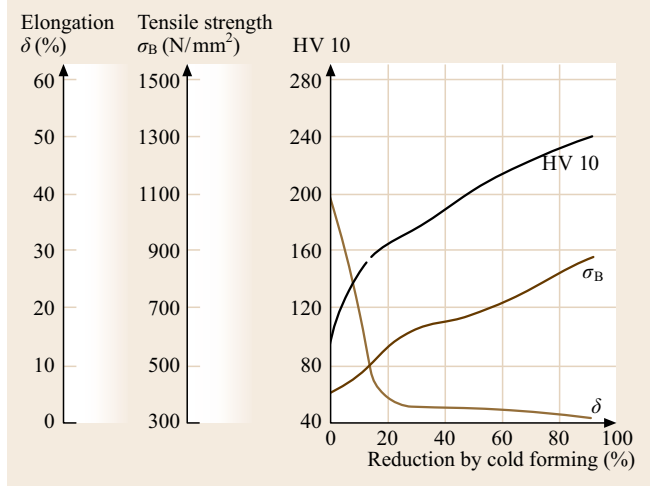


**Fig. 14.77** Work hardening of PdCu15 alloys (after [14.16])

### Electrical Properties

In Tables 14.88–14.90 [14.2] and Figs. 14.78 and 14.79 [14.13, 16] characteristic data are shown. Pure Pd shows no superconductivity, PdH and some intermetallic compounds are superconducting at low critical temperatures, e.g., $T_c(Bi_2Pd) = 3.7\,K$.

### Thermoelectric Properties

Tables 14.91–14.95 [14.1, 2] and Figs. 14.80 and 14.81 [14.1, 3] give data of absolute thermoelectric power, thermal electromotive force of pure Pd and Pd alloys at different temperatures. Special alloys for thermocouples with high corrosion resistance are shown in Table 14.95 [14.2].

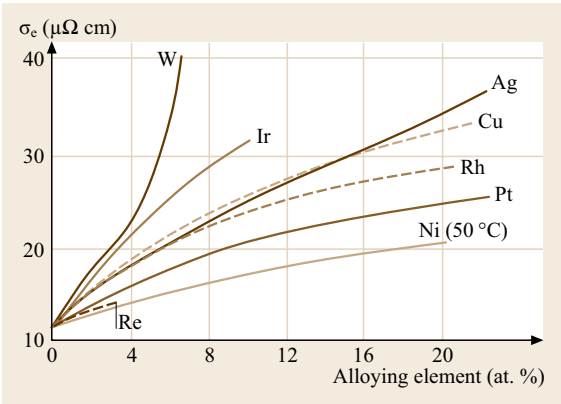


**Fig. 14.78** Influence of alloying elements on the electrical conductivity of Pd (after [14.16])

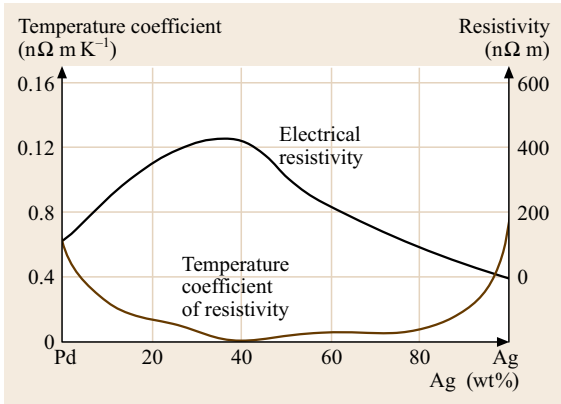


**Fig. 14.79** Electrical resistivity and temperature coefficient of resistivity of Pd-Ag alloys as a function of Ag content (after [14.13])

**Table 14.88** Increase of atomic electrical resistivity of Pd and Pt (after [14.2])

| Basic element | $\Delta\rho/C$ (μΩ cm/at.%) |
|---|---|
| Pd | Ag 1.17, Al 2.17, Au 0.65, B 1.43, Bi 5.45, Cd 1.36, Co 2.04, Cr 2.98, Cu 1.35, Fe 2.06, Ga 2.25, Ge 4.13, In 1.96, Ir 7.0, Mn 167, Mo 4.49, Ni 0.72, Pb 3.5, Pt 0.88, Rh 1.67, Ru 3.3, Sn 2.89, V 3.2, Zn 1.73, Zr 2.49 |
| Pt | Ag 2.2, Au 1.3, Be 3, Co 1.7, Cr 6.8, Cu 3, Fe 3.9, In 3.4, Mn 2.95, Mo 6.2, Nb 5.4, Ni 0.9, Os 2.4, Pd 0.6, Rh 1.0, Ru 2.4, Sn 3.9, W 5.7, Zr 4.7 |

**Table 14.89** Residual electrical resistivity ratio (RRR) of pure noble metals (273.2 K/4.2 K) (after [14.2])

| Ru | Rh | Pd | Ag | Os | Ir | Pt | Au |
|---|---|---|---|---|---|---|---|
| 25 000 | 570 | 570 | 2100 | 400 | 85 | 5000 | 300 |

**Table 14.90** Specific electrical resistivity of Pd at different temperatures (after [14.2])

| $T$ (K) | 90 | 175 | 273 | 500 | 800 | 1300 |
|---|---|---|---|---|---|---|
| $\rho$ (μΩ cm) | 2.147 | 5.821 | 9.725 | 17.848 | 26.856 | 38.061 |

**Table 14.91** Absolute thermoelectric power of the platinum-group metals at different temperatures (after [14.1])

| Metal | Absolute thermoelectric power (μV/deg) at | | | | | | | | |
|---|---|---|---|---|---|---|---|---|---|
| | −255 °C | −200 °C | −100 °C | −20 °C | 0 °C | 100 °C | 300 °C | 500 °C | 800 °C |
| Pd | +1.02 | +3.96 | −3.16 | −7.94 | −9.6 | −13.4 | −18.8 | – | −35 |
| Pt | +1.8 | +5.9 | +0.1 | −3.6 | −4.4 | −7.3 | −10.9 | −14.0 | −18.6 |
| Rh | +1.6 | +1.8 | – | +1.7 | – | +1.2 | +0.3 | 0.3 | – |
| Ir | – | – | +1.8 | – | +1.5 | +0.9 | −0.3 | −1.3 | – |
| Ru | – | – | – | – | – | – | −32.5 | −42 | −43 |

**Table 14.92** Thermal electromotive force $E_{A,Pt}$ (mV) of the thermocouples of noble metals and pure Pt at different temperatures, reference junction at 0 °C (after [14.2])

| Thermal electromotive force $E_{A,Pt}$ (mV) | | | | | | |
|---|---|---|---|---|---|---|
| $T$ (°C) | Ru | Rh | Ir | Pd | Ag | Au |
| −100 | | −0.32 | −0.35 | 0.48 | 0.21 | 0.21 |
| 0 | 0 | 0 | 0 | 0 | 0 | 0 |
| 100 | 0.684 | 0.70 | 0.660 | 0.570 | 0.740 | 0.770 |
| 300 | 2.673 | 2.68 | 2.522 | −1.990 | 3.050 | 3.127 |
| 600 | 6.485 | 6.77 | 6.201 | −5.030 | 8.410 | 8.115 |
| 900 | 11.229 | 12.04 | 10.943 | 9.720 | 10.943 | 14.615 |
| 1200 | 16.864 | 18.42 | 16.665 | – | – | – |
| 1400 | – | 22.56 | 20.819 | 20.41 | – | – |

**Table 14.93** Thermal electromotive force $E_{A,Pt}$ (mV) of Pd alloys at different temperatures, reference junction at 0 °C (after [14.2])

| Alloying element | $T$ (°C) | Composition (wt%) 10 | 30 | 50 | 70 | 90 |
|---|---|---|---|---|---|---|
| Ag | 100 | −1.1 | −2.4 | −3.3 | −0.5 | 0.1 |
| | 1000 | −23.5 | −44.4 | −45.8 | −11.5 | – |
| Au | 100 | −1.0 | −1.7 | −2.7 | −2.7 | 0 |
| | 1000 | −14.5 | −24.1 | −38.5 | −33.5 | 3.0 |
| | 1300 | −22.0 | −34.0 | −52.0 | −48.0 | – |
| Cu | 100 | −1.05 | −1.49 | | | |
| Ir | 100 | 2.01 | 2.02 | | | |
| | 1000 | 22.1 | 26.1 | | | |
| Ni | 100 | −0.80 | −1.47 | −1.75 | −1.75 | −1.65 |
| | 1000 | −9.4 | −9.4 | 10.2 | −11.6 | 11.5 |
| Pt | 100 | 0.32 | 0.83 | 0.75 | 0.53 | 0.22 |
| | 1000 | −2.1 | 7.8 | 9.4 | 7.8 | 4.6 |
| | 1300 | −5.2 | 8.0 | 11.7 | 10.7 | 5.3 |

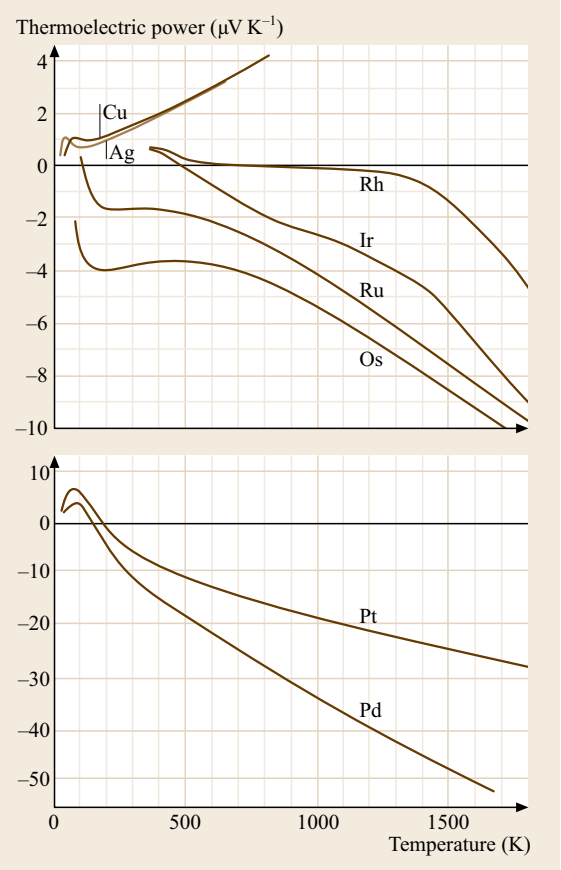


**Fig. 14.80** Thermoelectric power of the platinum group metals (after [14.3])

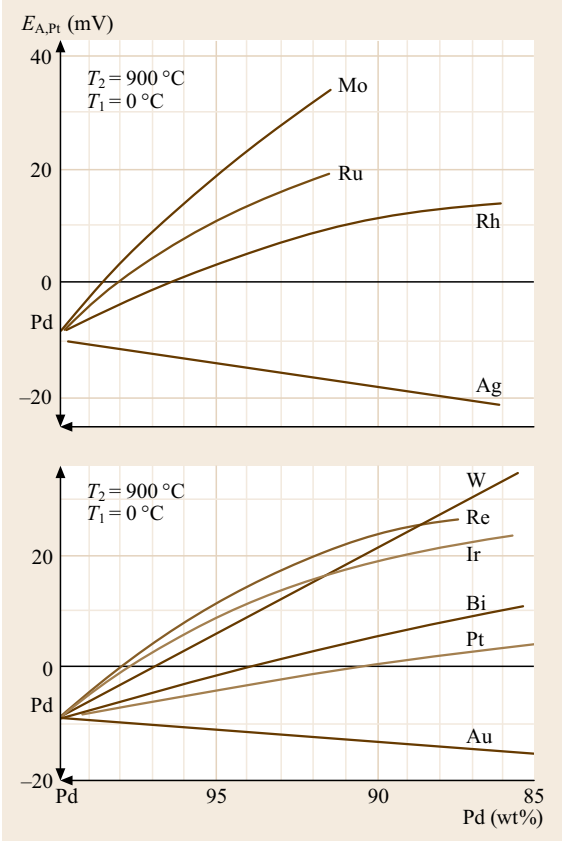


**Fig. 14.81** Thermal electromotive force $E_{At,Pt}$ of Pd alloys at 900 °C (reference junction at 0 °C) (after [14.1])

**Table 14.94** Basic data of thermal electromotive force of thermocouples according to Table 14.95 (after [14.2])

| *T* (°C) | Th.-C.1 (mV) | Th.-C.2 (mV) | Th.-C.3 (mV) |
|---|---|---|---|
| 100 | 3.31 | 4.6 | 3.3 |
| 400 | 15.70 | 21.5 | 15.4 |
| 600 | 24.70 | 34.2 | 24.6 |
| 800 | 33.50 | 46.9 | 33.4 |
| 1000 | 41.65 | 59.6 | 41.3 |

**Table 14.95** Palladium alloys for thermocouples (Th.-C.) of high corrosion resistance (after [14.2])

| | | |
|---|---|---|
| Th.-C.1 | AuPd40 | Pd38Pt14Au3 |
| Th.-C.2 | AuPd46 | PtIr10 |
| Th.-C.3 | AuPd35 | PtPd12.5 |

### Magnetic Properties

All PGMs show magnetostriction in a magnetic field. The reversible change of length is proportional to the square of the applied magnetic field (Table 14.96) [14.2, 3]. The paramagnetic susceptibilities of Pd and Pd alloys decrease with increasing temperature (Figs. 14.82 and 14.83) [14.2, 3]. Alloying with 0.05 wt% Rh raises the susceptibility from $88\times10^{-10}$ to $160\times10^{-10}\,m^3/mol$. Pd-Cu alloys are diamagnetic up to 50 at.% Pd. The susceptibilities of the ordered phases in this system are higher than those of the disordered solid solution phase. The paramagnetism of Pd decreases by dissolution of $H_2$ to reach zero at $PdH_{0.66}$ and above. Partial ordering within FePd raises its coercive field from the disordered value of 2–260 Oe [14.62].

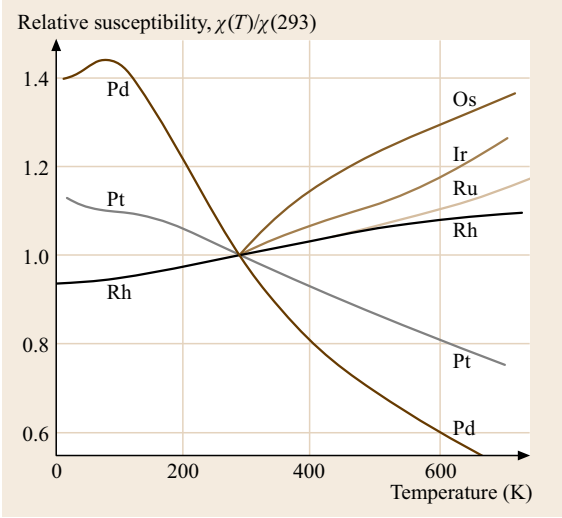


**Fig. 14.82** Temperature dependence of the magnetic susceptibility of the platinum group metals (after [14.3])

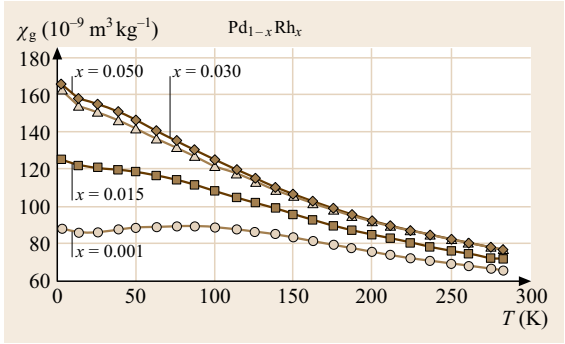


**Fig. 14.83** Temperature dependence of the magnetic mass susceptibility of Pd-Rh alloys (after [14.2])

**Table 14.96** Magnetostriction of platinum-group metal and platinum-group metal alloys, expressed by the factor $S_l$ of proportionality according to $\Delta l/l = S_l H^2$ (after [14.2])

| Metal/alloy | $S_l$ |
|---|---|
| Ru | 1.4 |
| Rh | 11 |
| Pd | −39.4 |
| Ir | 3.8 |
| Pt | −32 |
| $Rh_{0.50}Ir_{0.50}$ | 9.5 |
| $Rh_{0.50}Pd_{0.50}$ | 27 |
| $Ir_{0.60}Pd_{0.40}$ | 13.4 |
| $Pd_{0.67}Pt_{0.33}$ | −17.4 |
| $Pd_{0.33}Pt_{0.67}$ | −79 |

### Thermal Properties

Selected data of thermal conductivity and thermal expansion of PGM and Pg-Ag alloys are given in Tables 14.97–14.100, Fig. 14.84. Fe-Pd-alloys exhibit around the $Fe_3Pd$ stoechiometry in the disordered state zero coefficient of thermal expansion (Invar effect) [14.62].

### Optical Properties

In Table 14.101 and Fig. 14.85 characteristic data are given. The optical reflectance of Pd is increased by alloying with Ru (Fig. 14.86).

**Table 14.97** Recrystallization temperatures of platinum-group metal (at 0 °C) (depending on purity, degree of cold forming an annealing time) (after [14.2])

| Metal | Recrystallization temperature (°C) |
|---|---|
| Ir | 1200–1400 |
| Pd | 485–600 |
| Pt | 350–600 |
| Rh | 700–800 |
| Ru | 1200–1300 |

**Table 14.98** Thermal conductivity of platinum-group metals at different temperatures (after [14.2])

| Temperature (°C) | Thermal conductivity (W/(m K)) | | | | | | | |
|---|---|---|---|---|---|---|---|---|
| | Pd | Pt | Rh | Ir | Ru[a] | Ru[b] | Ru[c] | Os |
| 100 | 76 | 85.6 | 185 | – | 140 | 180 | 150 | – |
| 273 | 75.6 | 75.0 | 153 | 149 | 110 | 134 | 119 | 88 |
| 600 | 79.0 | 73.0 | 135 | 130 | 95 | 129 | 105 | 85 |
| 800 | 83.0 | 74.8 | 126 | 125 | 87 | 112 | 96 | – |
| 1200 | 88.2 | 83.2 | 118 | 117 | 77 | 101 | 83 | – |

[a] Vertical to the crystal *c* axis; [b] Parallel to the crystal *c* axis; [c] Polycrystalline

**Table 14.99** Thermal expansion coefficient of the platinum-group metals (after [14.2])

| Temperature (°C) | Thermal expansion coefficients ($10^{-6}$ K$^{-1}$) | | | | | | | | | |
|---|---|---|---|---|---|---|---|---|---|---|
| | Pd | Pt | Rh | Ir | Ru[a] | Ru[b] | Ru[c] | Os[a] | Os[b] | Os[c] |
| 323 | – | – | – | – | 5.9 | 8.8 | 6.9 | 4.0 | 5.8 | 4.8 |
| 373 | 11.9 | 9.1 | 8.5 | 6.7 | – | – | – | – | – | – |
| 423 | | | | | 6.1 | 9.3 | 7.2 | 4.3 | 6.2 | 5.0 |
| 473 | 12.1 | 9.2 | 9.0 | – | – | – | – | – | – | – |
| 623 | | | | | 6.8 | 10.5 | 8.0 | 4.0 | 7.1 | 5.7 |
| 673 | 12.6 | 9.5 | 9.6 | – | – | – | | – | – | |
| 723 | | | | | 7.2 | 11.0 | 8.4 | 5.3 | 7.6 | 6.2 |
| 823 | – | – | 9.6 | – | | 11.7 | 8.8 | 5.8 | 8.3 | 6.9 |
| 1073 | 13.4 | 10.0 | 10.3 | – | – | – | – | – | – | |

[a] Vertical to the crystal *c* axis; [b] Parallel to the crystal *c* axis; [c] Polycrystalline

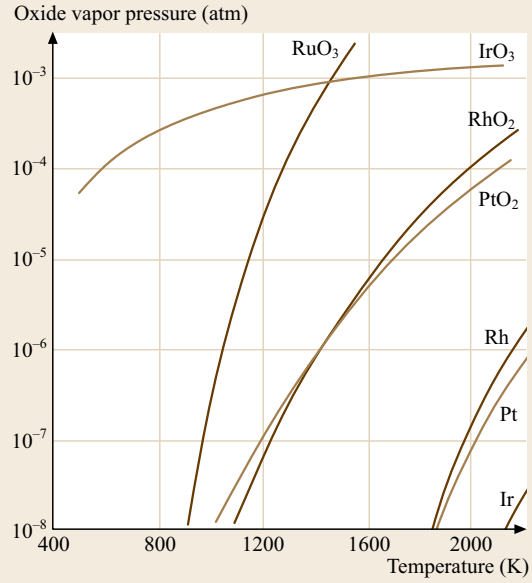


**Fig. 14.84** Vapor pressures of platinum group metal oxides (after [14.58])

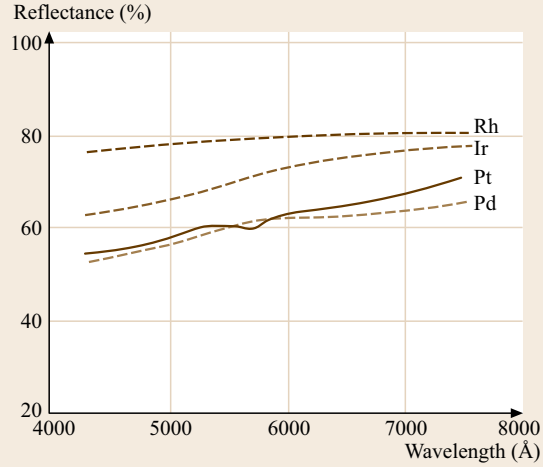


**Fig. 14.85** Optical reflectance of the platinum group metals (after [14.5])

**Table 14.100** Thermal expansion coefficient of Pd-Ag alloys; temperature range 373–473 K (after [14.2]) ►

| Temp. range (K) 373–473 | |
|---|---|
| Pd-content (%) | Thermal expansion coefficient ($10^{-6}$ K$^{-1}$) |
| 20 | 16.2 |
| 50 | 14.7 |
| 80 | 12.4 |

**Table 14.101** Spectral degree of emission $\varepsilon$ of the platinum-group metals at different temperatures (after [14.2])

| | Surface | Temperature (°C) | Spectral emission $\varepsilon$ |
|---|---|---|---|
| Ru[b] | Solid | 1000 | 0.421 |
| | Solid | 2000 | 0.314 |
| Os[b] | Solid | 1000 | 0.526 |
| | Solid | 2000 | 0.383 |
| Rh[a] | Solid | < 1966 | 0.29 |
| | Liquid | > 1966 | 0.3 |
| Ir[a] | Solid | 927–2027 | 0.3 |
| | Solid | 2000 | 0.383 |
| Pd[a] | Solid | 900–1530 | 0.33 |
| | Liquid | 1555 | 0.37 |
| Pt[a] | Solid | 1000 | 0.371 |
| | Solid | 1400 | 0.421 |
| | Liquid | 1800 | 0.38 |

[a] 650 nm, [b] 655 nm

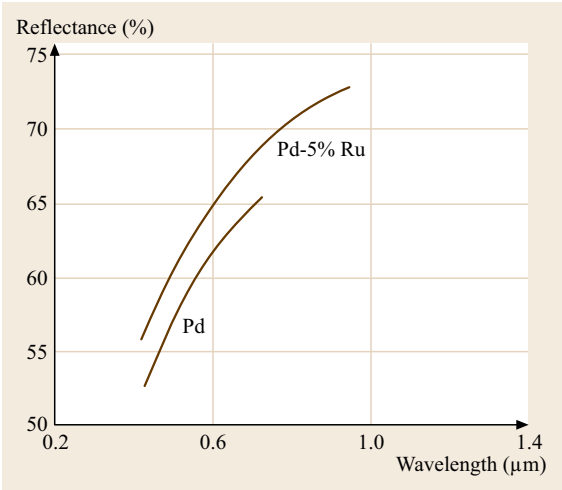


**Fig. 14.86** Optical reflectance of PdRu5 alloy (after [14.13])

## Diffusion

Data for selfdiffusion, diffusion of tracer elements and of hydrogen and oxygen are shown in Tables 14.42, 14.43, and 14.102.

Carbon diffuses very rapidly through Pd at elevated temperatures in presence of a concentration gradient on the surface.

## Chemical Properties

Pd has the reduction potential of $E_0 = 0.951\,\mathrm{V}$ for $Pd/Pd^{2+}$. It is resisant against reducing acids and in oxydizing media above pH 2. Alkali melts attack above $\approx 400\,°C$. In oxygen atmosphere between 400 and

**Table 14.102** Self-diffusion in pure platinum-group metals (after [14.2])

| Element | $D^0$ ($10^{-4}\,m^2/s$) | $Q$ (kJ/mol) | $T$ (K) |
|---|---|---|---|
| **Lattice diffusion** | | | |
| Ir(S) | 0.36 | 438.8 | 2092–2664 |
| Pd(S) | 0.205 | 266.3 | 1323–1773 |
| Pt | 0.33 | 285.6 | 1598–1837 |
| Pt(S) | 0.05 | 257.6 | 850–1265 |
| **Surface diffusion** | | | |
| Rh(111) | $4\times10^{-6}$ | 174 | 1200–1500 (Vac.) |
| Pt | $4\times10^{-7}$ | 108 | 1160–1580 (Vac.) |

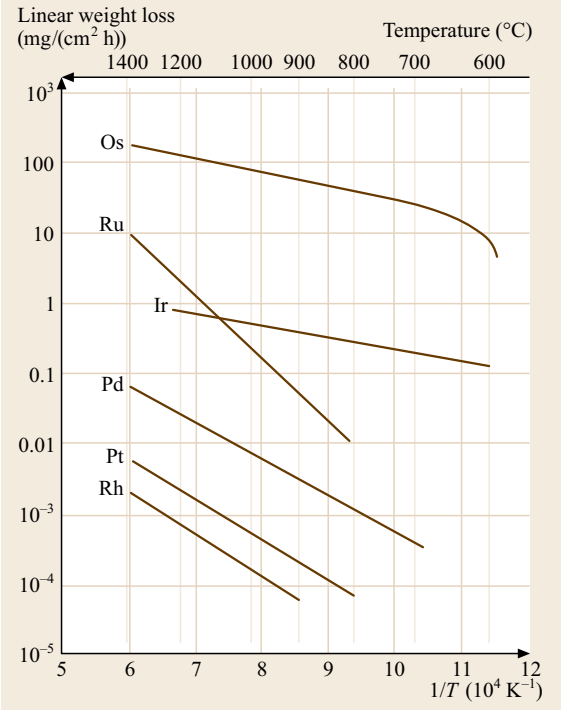


**Fig. 14.87** Weight losses of the platinum group metals at annealing on air (after [14.2])

800 °C are thin PdO-surface layers formed, which dissociate above 800 °C. Above 1100 °C occur increasing weight losses by evaporation (Fig. 14.87).

Catalysis: Pd and Pd alloys are effective catalysts in numerous chemical reactions. In heterogenous catalysis, PGM are applied in form of wire nets and of powders with high specific surfaces (20–1000 $m^2/g$, *platinum black*, *palladium black*) on carbon or $Al_2O_3$ supports. Automotive gas cleaning catalysts use of Pd-Pt-Rh alloys in different compositions.

**Table 14.103** Physical properties of some technical Pd and Pt alloys (after [14.16])

| Material | Density ($g/cm^3$) | Melting point/interval (°C) | Electrical conductivity ($10^6$ S/m) | Temperature coefficient of electrical resistance ($10^3$ $K^{-1}$) | Modulus of elasticity ($kN/mm^2$) |
|---|---|---|---|---|---|
| Pt (99.9) | 21.45 | 1773 | 9.4 | 3.92 | 16–17 |
| PtIr5 | 21.5 | 1774–1776 | 4.5 | – | 18.5–19.5 |
| PtIr10 | 21.6 | 1780–1785 | 5.6 | 2.0 | ca. 22 |
| PtRu10 | 20.6 | ca. 1800 | 3.0 | 0.83 | ca. 23.5 |
| PtNi8 | 19.2 | 1670–1710 | 3.3 | 1.5 | ca. 18 |
| PtW5 | 21.3 | 1830–1850 | 2.3 | 0.7 | ca. 18.5 |
| Pd (99.99) | 12.0 | 1552 | 9.3 | 3.77 | ca. 12.5 |
| PdCu15 | 11.3 | 1370–1410 | 2.6 | 0.49 | ca. 17.5 |
| PdCu40 | 10.4 | 1200–1230 | 3.0 | 0.28 | ca. 17.5 |
| PdNi5 | 11.8 | 1455–1485 | 5.9 | 2.47 | ca. 17.5 |

**Table 14.104** Composition and melting temperature range of selected Pd-jewelry alloys (after [14.2])

| Alloy | Melting temperature range (°C) |
|---|---|
| Pd95Cu3Ga2 | 1340–1400 |
| Pd95Cu5 | 1400–1460 |
| Pd95Ni5 | 1450–1490 |
| Pd50Ag47.5Cu2.5 | 1200–1280 |

**Table 14.106** Crystal structure and lattice parameters of intermediate phases of Pt oxides (after [14.4])

| Phase | Structure | Type | *a* (nm) | *b* (nm) | *c* (nm) |
|---|---|---|---|---|---|
| PtO | Tetragonal | PtO | 0.304 | | 0.534 |
| $Pt_3O_4$ | Cubic | $Pt_3O_4$ | 0.6226 | | |
| $PtO_2$ | Orthorhombic | $Fe_2O_3$ | 0.4533 | 0.4488 | 0.3138 |
| $PtO_2$ | Hexagonal | | 0.310 | | 0.435 |

### Special Alloys

Tables 14.45, 14.46, and 14.103 show typical compositions of Pd containing brazing alloys, and Table 14.104 shows Pd containing jewelry alloys. PdAg40 has a very low temperature coefficient of resistivity (0.00003 $°C^{-1}$ between 0 and 100 °C, electrical resistivity 42 μΩ cm). It is used for precision resistance wires (Fig. 14.79). Pd60Ni35Cr5 is corrosion resistant against molten salt mixtures up to 700 °C, suited for brazing graphit, Mo and W.

Ti-Pd-Ni and Fe-Pd alloys show shape memory effects. Partial replacement of Pd in the alloy Fe30 at.% Pd by > 4 at.% Pt decreases the temperature of the fcc/fct martensite transformation and effects strengthening.

## 14.3.2 Platinum and Platinum Alloys

Platinum and platinum alloys are important constituents of catalysts (chemistry, automotive exhaust gas cleaning, fuel cells), sensor materials (thermocouples, resistance thermometers), strong permanent magnet alloys, magnetic and magnetooptical (memory) devices, high temperature and corrosion resistant structural parts, and electrical contacts and connecting elements. Classical applications are jewelry and dentistry alloys.

Commercial grades are sponge and powder in purities varying from minimum 99.9 to 99.95% (ASTM B 561-86). High purity electronic grade is 99.99%.

### Production

Platinum sponge or powder are compacted by pressing and sintering. Melting and alloying is done in electrical heated furnaces in $Al_2O_3$ or MgO crucibles, by vacuum arc and by electron beam melting 99.98%.

### Phases and Phase Equilibria

Selected phase diagrams are shown in Figs. 14.88–14.92 [14.4]. Thermodynamic data are given in Tables 14.76, 14.78, and 14.105 [14.1, 2, 7]. For compositions and crystal structures, see Tables 14.81, 14.106, and 14.107 [14.2, 4]. Platinum forms continuous solid

**Table 14.105** Thermodynamic data of Pt (after [14.2])

| *T* (K) | $c_p$ (J/(K mol)) | *S* (J/(K mol)) | *H* (J/mol) | *G* (J/mol) | *p* (at) |
|---|---|---|---|---|---|
| 298.15 | 25.857 | 41.631 | 0 | 112.412 | $8.26 \times 10^{-92}$ |
| 400 | 26.451 | 49.314 | 2.664 | −17.961 | $1.30 \times 10^{-66}$ |
| 800 | 28.593 | 68.313 | 13.677 | −40.973 | $9.75 \times 10^{-30}$ |
| 1400 | 31.731 | 85.111 | 31.776 | −87.38 | $5.84 \times 10^{-14}$ |

*T* = temperature, $c_p$ = specific heat capacity, *S* = entropy, *H* = enthalpy, *G* = free enthalpy, *p* = partial pressure of the pure elements

**Table 14.107** Structure and lattice parameter of selected intermediate Pt compounds (after [14.2])

| Phase | Pearson symbol | *a* (nm) | *b* (nm) | *c* (nm) | *c*/*a* | Remarks | Concentration *x* $A_{1-x}B_x$ |
|---|---|---|---|---|---|---|---|
| CoPt | *tP*4 | 0.3806 | 0.3684 | 0.9679 | | | |
| $CoPt_3$ | *cP*4 | 0.3831 | | | | | |
| CuPt | *hR*32 | 0.7589 | | | | | 0.5 |
| $CuPt_3$ | *cF*4 | 0.3849 | | | | | |
| $Cu_3Pt$ | *o*** | 0.7596 | 0.2745 | 0.777 | | | |
| $Cu_3Pt$ | *cP*4 | 0.3682 | | | | | |
| Fe-Pt | *cF*4 | 0.376 | | | | | 0.245 |
| FePt | *tP*4 | 0.3861 | | 0.3788 | 0.9811 | | |
| $Fe_3Pt$ | *cP*4 | 0.3727 | | | | | |
| NiPt | *tP*4 | 0.3823 | | 0.3589 | 0.9388 | | |
| PtZr | *oC*8 | 0.3409 | 1.0315 | 0.4277 | | | |
| $Pt_3Zr$ | *hP*16 | 0.5624 | | 0.9213 | 1.6328 | | |

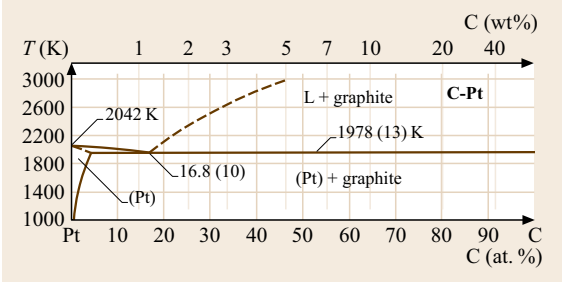


**Fig. 14.88** Binary phase diagram: Pt-C (after [14.4])

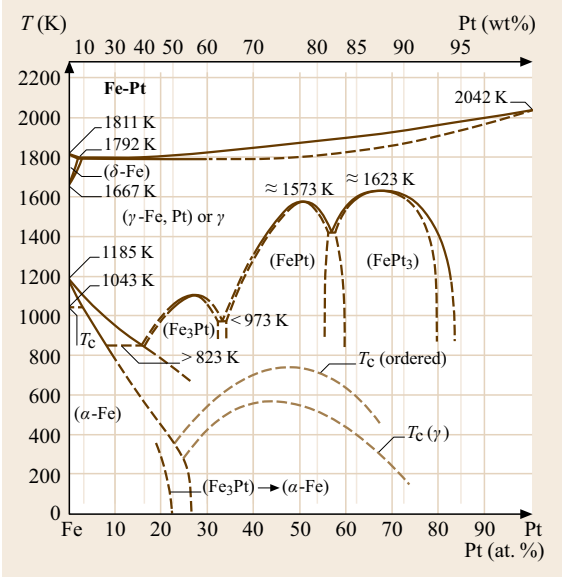


**Fig. 14.89** Binary phase diagram: Pt-Fe (*dash-dotted line*: Curie temperature) (after [14.4])

solutions with all other noble metals and with Co, Cu, Fe, and Ni. Miscibility gaps exist with C, Co, Ir,

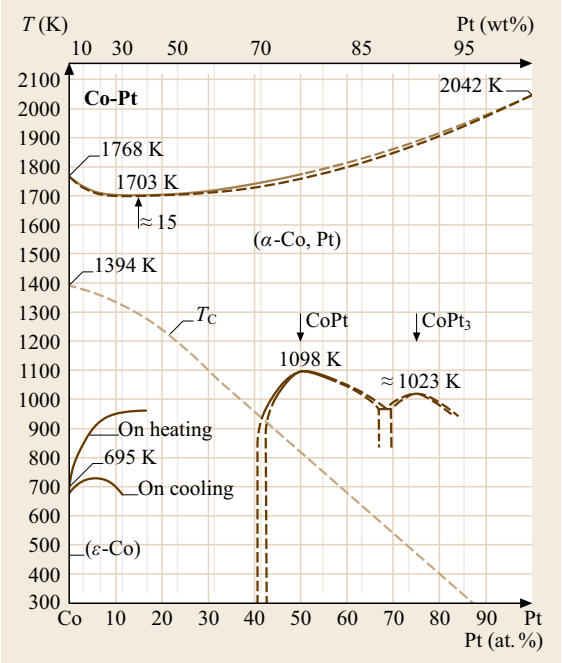


**Fig. 14.90** Binary phase diagram: Pt-Co (after [14.4])

Pt, and Rh. Primary solid solutions have fcc structure and the lattice parameters correspond with few exceptions roughly to Vegard's law. Numerous intermediate phases exist in alloy systems with rare earth metals. The formation and crystal structures of the intermediate phases have been related to the electron configuration of the alloy components (Engel–Brewer correlation) [14.43, 63]. Phases with superlattice structures are formed with Co, Cu, Fe, Nb, and V in atomic ratios of 1 : 1, 2 : 1, and 3 : 1 (Tables 14.8, 14.82). The ordered CuPt phase has a long-range ordered rhombohedral structure.

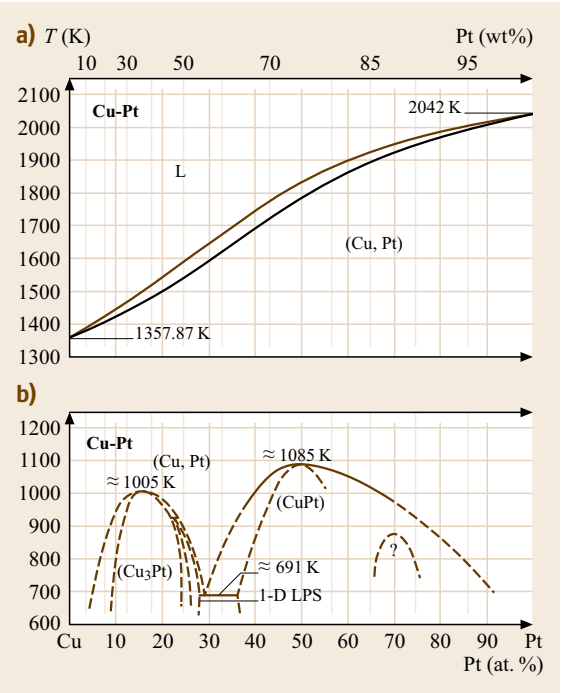


**Fig. 14.91a,b** Binary phase diagrams: Pt-Cu. **(a)** Liquid–solid, **(b)** solid–solid (1D-LPS = one-dimensional long-period superstructure) (after [14.4])

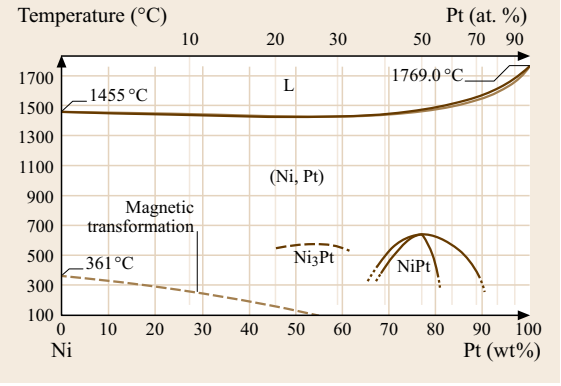


**Fig. 14.92** Binary phase diagram: Pt-Ni (after [14.4])

### Mechanical Properties

Characteristic data are shown in Tables 14.108–14.111 [14.2] and Figs. 14.93–14.101 [14.2, 13, 13, 16]. For elastic properties of PGMs at different temperatures, see [14.2]. Strengthening is affected by solid solution hardening, order hardening (Pt-Co, Pt-Cu), and dispersion hardening. Dispersion-strengthened Pt and Pt alloys are remarkably resistant to creep at high temperatures. They are produced either by co-precipitation with refractory oxides (e.g., 0.16 vol.% $ZrO_2$) or by internal oxidation of alloys with 0.2 wt% Cr or 0.8 wt% Zr. Rh additions improve the solubility for oxygen. TiC powder affects dispersion strengthening in concentrations of 0.04–0.08 wt% (Fig. 14.102) [14.58].

**Table 14.108** Elastic constants of Pt (after [14.2])

| $c_{11}$ | $c_{12}$ | $c_{44}$ |
|---|---|---|
| 347 | 173 | 76.5 |

**Table 14.109** Mechanical properties of Pt (99.9%) at different temperatures (after [14.2])

| $T$ (°C) | $E$ (GPa) | $R_m$ (MPa) | $A$ (%) | $R_{p0.2}$ (MPa) | HV |
|---|---|---|---|---|---|
| 20 | 173 | 135 | 41 | 50 | 55 |
| 250 | 169 | 110 | 40 | 40 | 53 |
| 500 | 159 | 78 | 42 | 30 | 50 |
| 750 | 140 | 44 | 46 | 20 | 35 |
| 900 | 126 | 34 | 44 | 17[a] | 23 |

[a] Interpolation
$A$ = elongation, $E$ = modulus of elasticity, $R_p$ = limit of proportionality, HV = Vickers hardness, $R_m$ = tensile strength

**Table 14.110** Mechanical properties of Pt as function of reduction in thickness (%) by cold rolling (after [14.2])

| Reduction (%) | $R_m$ (MPa) | $R_p$ (MPa) | HV Pt > 99.5% | HV Pt > 99.99% |
|---|---|---|---|---|
| 0 | 250 | 140 | 50 | 40 |
| 20 | 350 | 310 | 70 | 63 |
| 59 | 400 | 380 | 84 | 73 |

**Table 14.111** Tensile strength $R_m$ and elongation $A$ of binary Pt alloys at different temperatures (after [14.2])

| Alloy compound (wt%) | $R_m$ (MPa)/$A$ (%) 20 °C | 400 °C | 600 °C |
|---|---|---|---|
| Au5 | 340/18 | 290/10 | 250/10 |
| Ir10 | 260/33 | 240/27 | 180/33 |
| Ni5 | 470/26 | 420/26 | 320/25 |
| Pd20Rh5 | 370/30 | 290/18 | 240/23 |
| Rh5 | 225/44 | 150/40 | 120/43 |
| Rh10 | 287/39 | 200/33 | 170/38 |

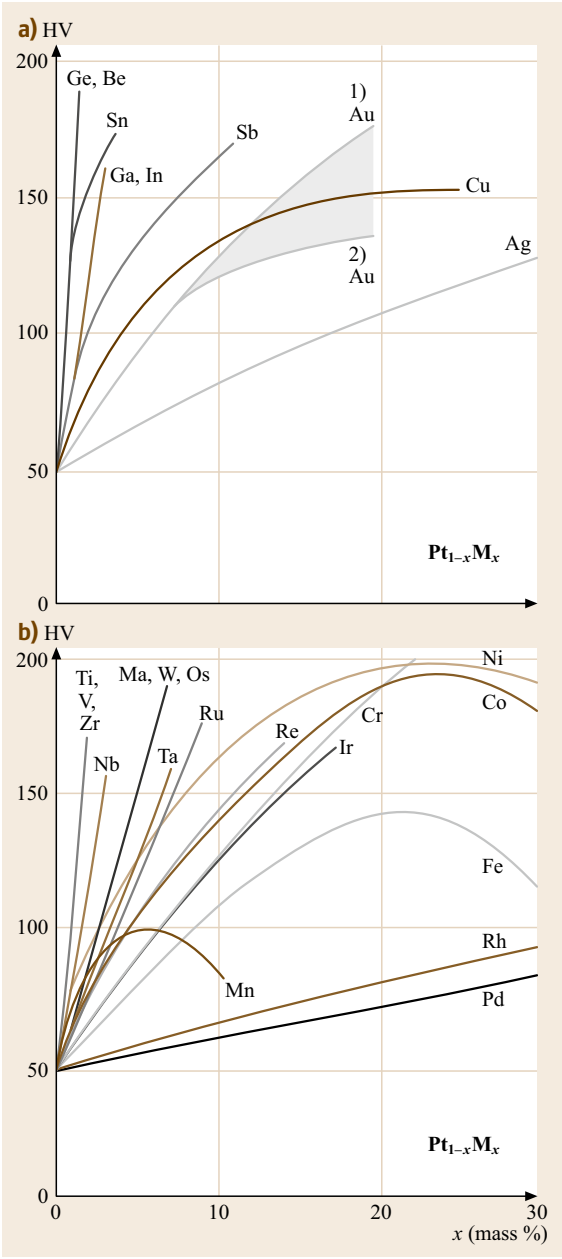


**Fig. 14.93a,b** Solid solution hardening of binary Pt alloys: **(a)** de-alloyed at 900 °C; **(b)** solution annealed at 1200 °C (after [14.2])

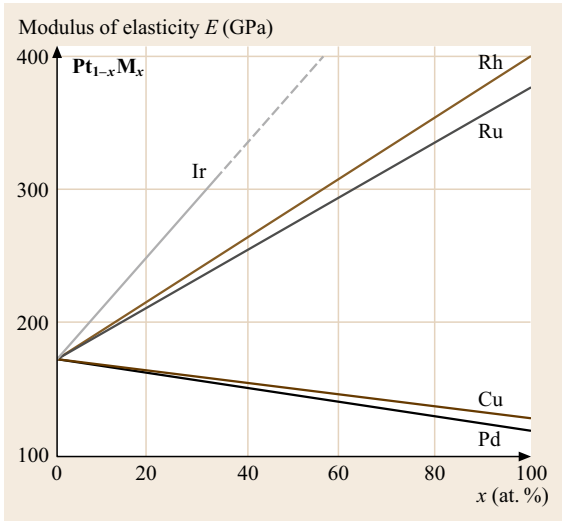


**Fig. 14.94** Modulus of elasticity $E$ of binary Pt alloys (after [14.2])

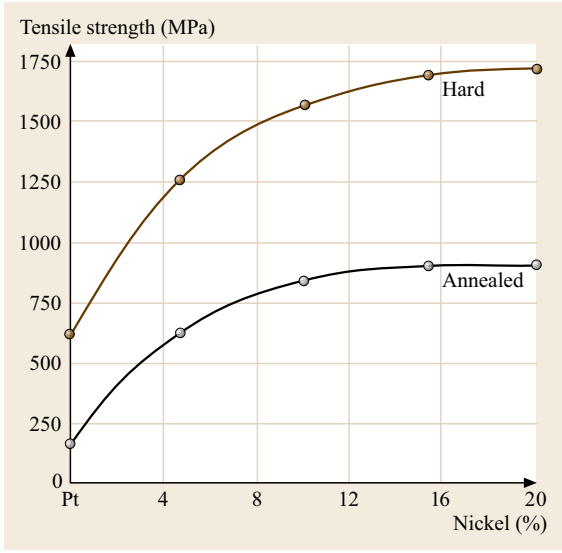


**Fig. 14.95** Tensile strength of Pt-Ni alloys as a function of Ni content (after [14.13])

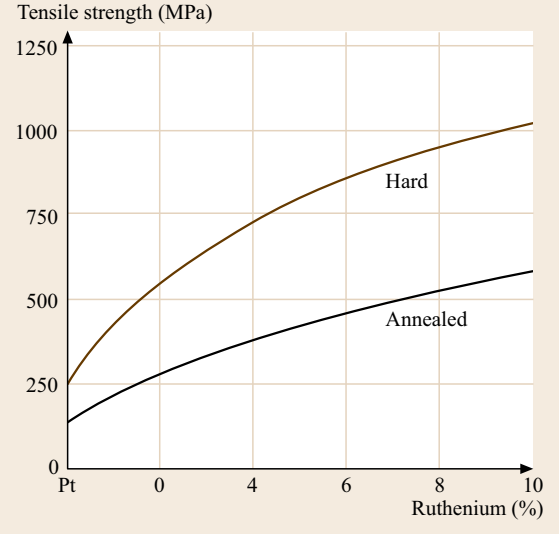


**Fig. 14.96** Tensile strength of Pt-Ru alloys as a function of Ru content (after [14.13])

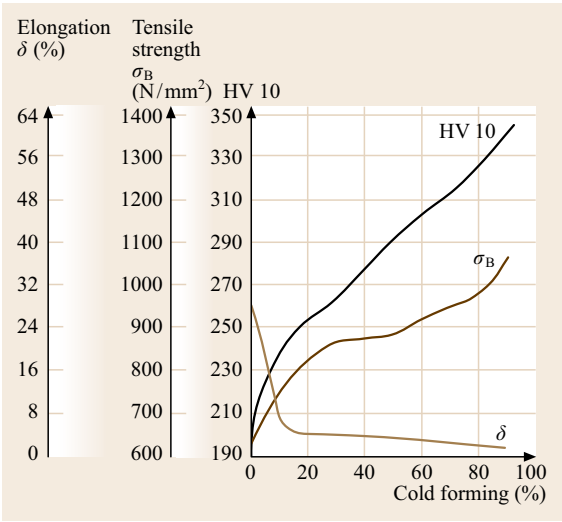


**Fig. 14.98** Mechanical properties of PtNi8 by cold forming as a function of reduction of cross section (after [14.16])

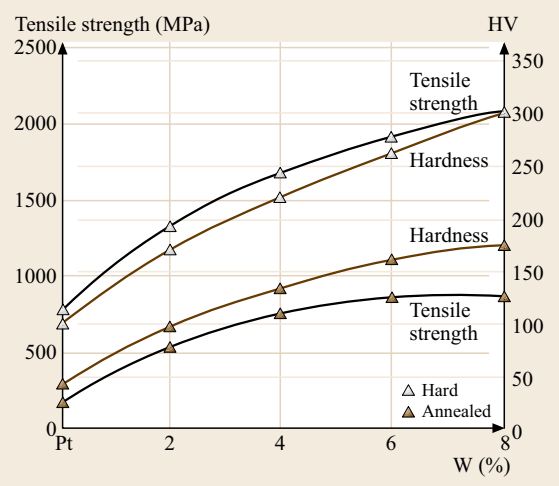


**Fig. 14.97** Tensile strength of Pt-W alloys as a function of W content (after [14.13])

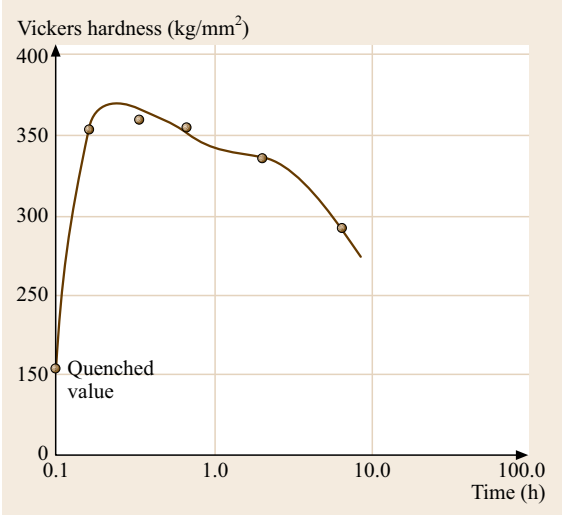


**Fig. 14.99** Order hardening of stoichiometric CuPt alloy (after [14.64])

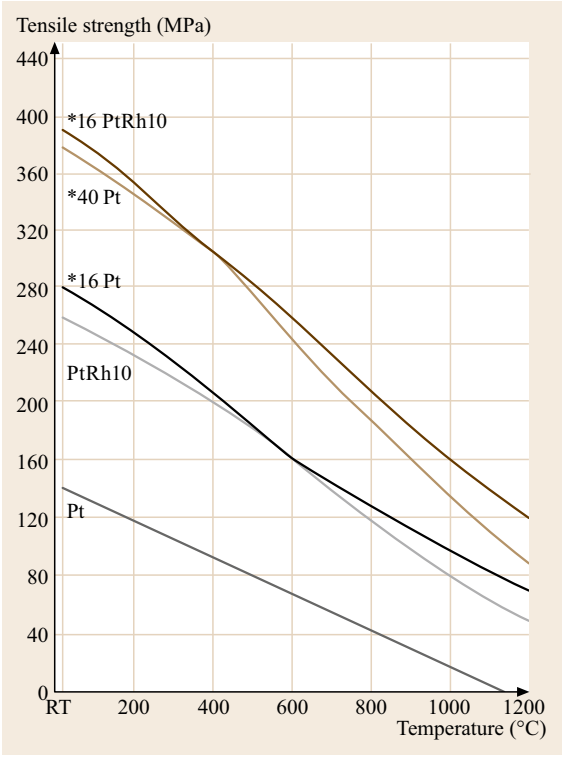


**Fig. 14.100** Tensile strength of dispersion hardened Pt and PtRh10 (* grain stabilized with 0.16 and 0.40 vol.% $ZrO_2$, respectively; RT = room temperature) (after [14.2])

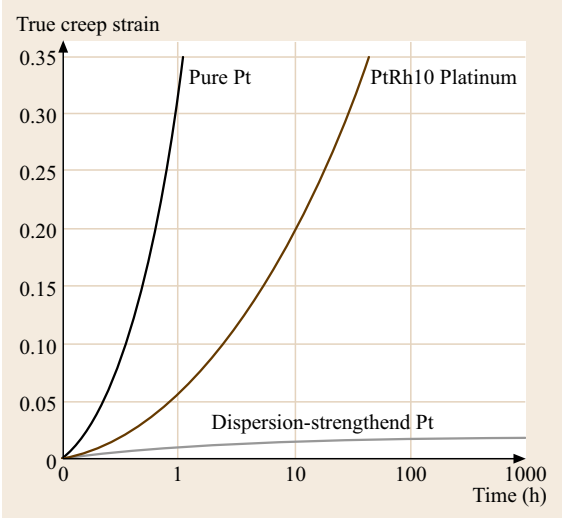


**Fig. 14.101** Creep curves of TiC-dispersion-strengthened Pt and PtRh10 wire at 1400 °C in air (after [14.58])

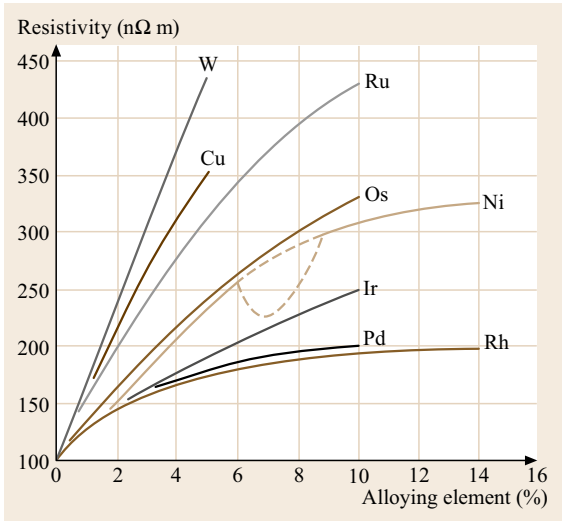


**Fig. 14.102** Effect of various alloying additions on the electrical resistivity of binary Pt alloys at 20 °C (after [14.16])

### Electrical Properties

Characteristic data are shown in Tables 14.89, 14.88, and 14.112 [14.2] and Figs. 14.103–14.104 [14.2, 13, 16]. Mo-28 at.% Pt (A15 structure) shows superconductivity at $T_c \approx 4.2-5.6$ K [14.65].

### Thermoelectric Properties

Selected values of thermal electromotive force of Pt and Pt alloys are given in Tables 14.91, 14.92, and 14.113–14.116 [14.1, 2, 7], and Figs. 14.105 and 14.106 [14.1]. Thermocouples that are Pt-Rh-based are especially suited for high temperatures (Fig. 14.107).

**Table 14.112** Specific electrical resistivity of Pt at different temperatures (after [14.2])

| $T$ (K) | 10 | 50 | 120 | 273 | 673 | 1273 | 1673 |
|---|---|---|---|---|---|---|---|
| $\rho$ ($\mu\Omega$ cm) | 0.0029 | 0.719 | $3.56_5$ | 9.83 | 24.57 | 37.45 | 53.35 |

**Table 14.113** Pt-Rh thermocouples according to IEC 5845 (Fig. 14.107) (after [14.2])

| Class | Thermocouple | Maximum applicable temperature (°C) |
|---|---|---|
| Type R | PtRh8713/Pt | 1500–1600 |
| Type S | PtRh9010/Pt | 1500–1600 |
| Type B | PtRh7030/Pt | 1750–1800 |

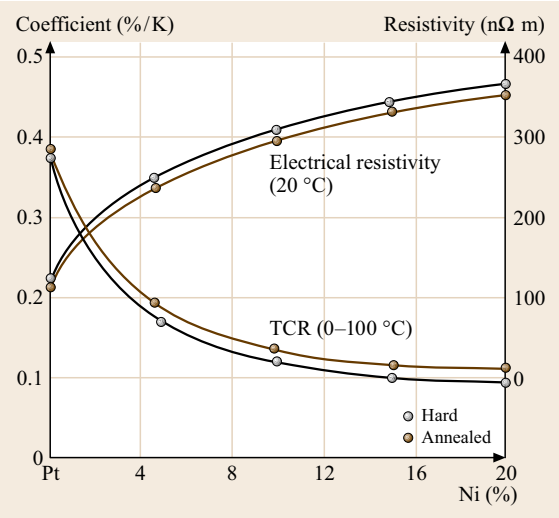


**Fig. 14.103** Electrical resistivity and temperature coefficient of resistivity (TCR) of Pt-Ni alloys as a function of composition (after [14.13])

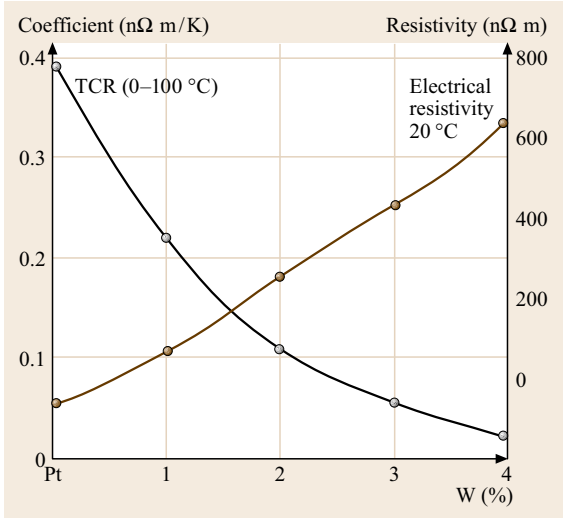


**Fig. 14.104** Electrical resistivity and temperature coefficient of resistivity (TCR) of Pt-W alloys as a function of composition (after [14.13])

**Table 14.114** Absolute thermoelectric power of Pt (after [14.7])

| Temperature (K) | 300 | 400 | 500 | 600 | 700 | 800 | 900 | 1000 | 1100 | 1200 |
|---|---|---|---|---|---|---|---|---|---|---|
| Thermoelectric power (μV/K) | −5.05 | −7.66 | −9.69 | −11.33 | −12.87 | −14.38 | −15.97 | −17.58 | −19.03 | −20.56 |

**Table 14.115** Thermal electromotive force of Pt alloys (mV) at different temperatures, reference junction at 0 °C (after [14.2])

| Alloy const. | $T$ (°C) | Composition (wt%) | | | | | |
|---|---|---|---|---|---|---|---|
| | | 10 | 30 | 40 | 70 | 80 | 90 |
| Ag | 100 | | | | −0.4 | −0.1 | 0.2 |
| | 900 | | | | 6.8 | 4.0 | 4.5 |
| Au | 100 | | | | | 0.8 | 0.4 |
| | 900 | | | | | 11.9 | 13.5 |
| Ir | 100 | 1.3 | 1.2 | | | | |
| | 1000 | 15.7 | 19.1 | 19.4 | | | |
| Rh | 100 | 0.64 | 0.62 | 0.60 | | | |
| | 1000 | 9.57 | 12.3 | 13.3 | | | |
| | 1300 | 13.1 | 17.9 | 19.0 | | | |

**Table 14.116** Basic values of thermal electromotive force (mV) of common PGM-based thermocouples (after [14.1])

| $T_1$ (°C) | $T_2$ (°C) | Pt-Rh10/Pt | Pt-Rh20/Pt-Rh5 | Rh-Ir60 | Platinel[a] | Pallador[b] |
|---|---|---|---|---|---|---|
| 0 | 100 | 0.643 | 0.074 | 0.371 | 3.31 | 4.6 |
| 0 | 500 | 4.221 | 1.447 | 2.562 | 20.20 | 27.9 |
| 0 | 1000 | 9.570 | 4.921 | 5.495 | 41.65 | 59.6 |
| $T_1$ (K) | $T_2$ (K) | Au-Co2.1/Cu (at.%) | Au-Fe0.02/Cu (at.%) | | | |
| 4.2 | 10 | 0.044 | 0.093 | | | |
| 4.2 | 20 | 0.173 | 0.208 | | | |
| 4.2 | 40 | 0.590 | 0.423 | | | |

[a] Platinel, Pd83Pt14Au3/AuPd35, [b] Pallador, PtIr10/AuPd40

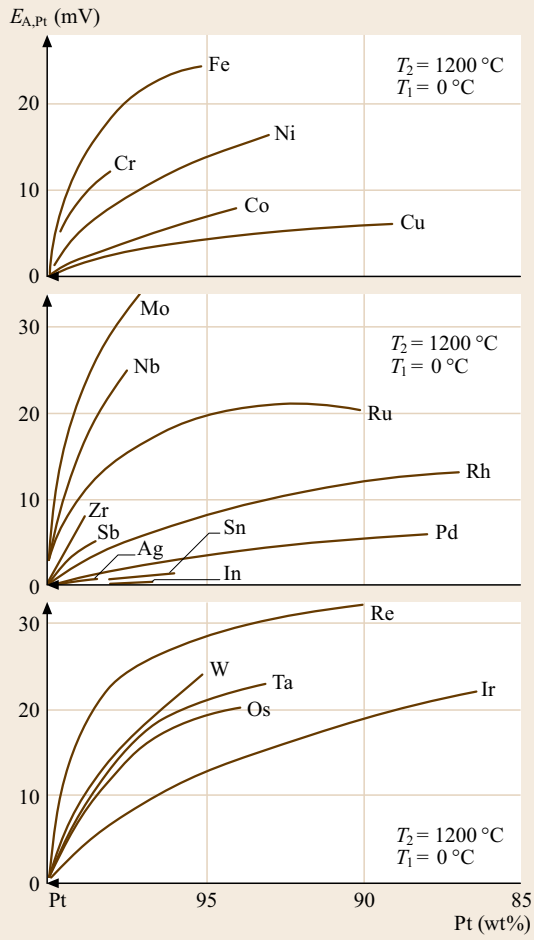


**Fig. 14.105** Thermal electromotive force $E_{A,Pt}$ of binary Pt alloys (after [14.1])

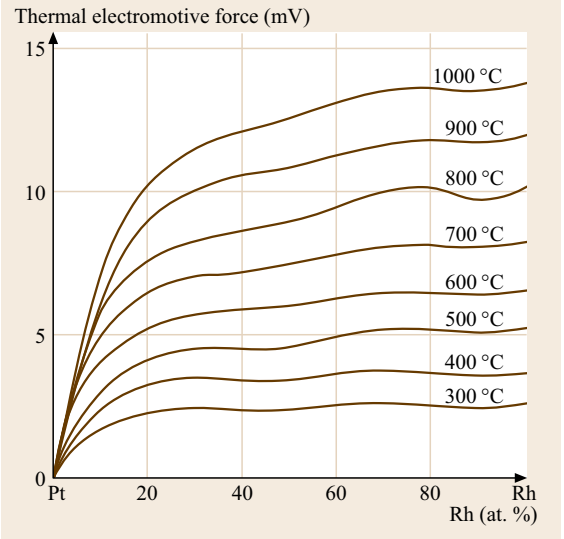


**Fig. 14.106** Influence of the Rh content on the thermal electromotive force of Pt-Rh alloys against Pt (after [14.2])

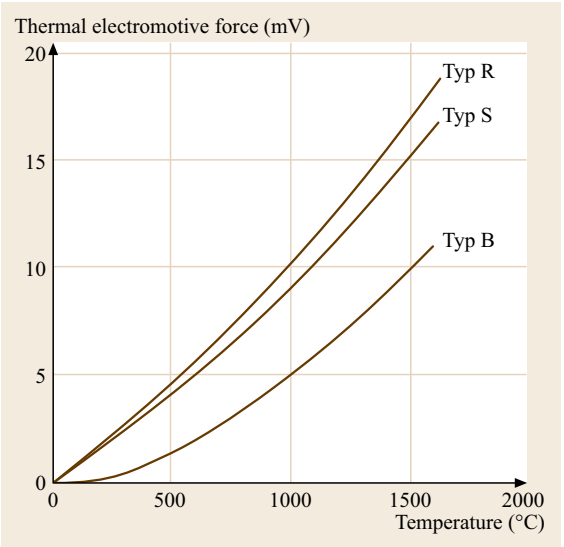


**Fig. 14.107** Thermal electromotive force of Pt-Rh thermocouples according to IEC 5845 (type R: PtRh8713/Pt; type S: PtRh9010/Pt; type B: PtRh7030/PtRh946) (after [14.2])

### Magnetic Properties

Selected data are shown in Tables 14.96 and 14.117 [14.2, 7], and Fig. 14.108 [14.5]. The paramagnetic susceptibility of Pt ($25.2\times10^{-10}\,m^3\,mol^{-1}$ at 0 K) rises by alloying with 0.1 at.% Rh to $42.5\times10^{-10}\,m^3\,mol^{-1}$. CoPt is a hard magnetic material ($H_c = 3500–4700$ Oe) but has been replaced by rare-earth transition metal magnetic materials in recent years. Superlattice phases in Pt-Cr-alloys in the composition ranges of 17–65 wt% Cr are ferromagnetic, with the maximum of $T_c$ at $\approx 30$ at.% Cr. The superlattice structure in FePt and CoPt with tetragonal crystal symmetry gives rise to high values of magnetic anisotropy. The coercivity of sputtered Pt-Co multilayers is increased by annealing in air, caused by the formation of cobalt oxide at the grain boundaries. The oxide layer gives rise to domain pinning and to magnetic isolation of the grains, thus leading to a high perpendicular anisotropy [14.2].

**Table 14.117** Characteristic properties of technical permanent magnet alloys (after [14.7])

| Alloy | $BH_{max}$ (kJ/m$^3$) | $H_c$ (kA/m) | $B_r$ (T) |
|---|---|---|---|
| Pt77Co23 | 75.0 | 380 | 0.60 |
| Sm34Co66 | 110–160 | 560 | 0.80 |
| Co52Fe35V13 | 22.4 | 36 | 1.00 |

$BH_{max}$ = maximum product; $H_c$ = coercive field strength; $B_r$ = remanence

**Table 14.118** Thermal conductivity $\lambda$ of Pt-(Au,Rh,Ir) alloys (after [14.2])

| Alloy | PtAu5 | PtRh5 | PtRh10 | PtRh20 | PtIr5 | PtIr10 |
|---|---|---|---|---|---|---|
| $\lambda$ (W/m K) | 43 | 33[a] | 30 | 28[a] | 42 | 31 |

[a] Calculated with Wiedemann–Franz' law $\lambda = L\sigma T$, Lorenz number $L = 2.45\times10^{-6}$ W/K from $\lambda$(PtRh10) and the specific electrical conductivity of Pt-Rh-alloys

**Table 14.119** Thermal expansion coefficient $\alpha$ of Pt-Rh alloys at different temperature ranges (after [14.2])

| Rh-content (wt%) | $\alpha$ ($10^{-6}$ K$^{-1}$) 273–983 K | 293–1473 K |
|---|---|---|
| 6 | 10.7 | 11.3 |
| 10 | 10.7 | 11.2 |
| 20 | 10.9 | 11.5 |
| 30 | 10.8 | 11.4 |

### Thermal Properties

Tables 14.97–14.100, 14.118, and 14.119 [14.2] provide selected data of thermal conductivity and thermal expansion. In the disordered state the Fe-Pt alloy system exhibits a negative thermal expansion coefficient at room temperature near $Fe_3Pt$ (Invar effect) [14.62].

### Optical Properties

Values of the spectral degree of emission and the optical reflectivity are given in Table 14.101 [14.2] and Fig. 14.85 [14.5].

### Diffusion

Data for self-diffusion, diffusion of tracer elements and of hydrogen and oxygen are shown in Tables 14.43 and 14.102 [14.2].

### Chemical Properties

Platinum has the reduction potential $E_0 = +1.118$ V for $Pt/Pt^{2+}$. It is resistant against reducing acids in all pH ranges, but is attacked by alkali and oxidizing media. Alloying with 30 at.% Rh improves the corrosion resistance against alkali hydroxides. Figure 14.109 and Table 14.120 [14.2] give the potential pH diagram of the system $Pt/H_2O$ at 25 °C. Dry chlorine attacks with rising temperature (Fig. 14.110 [14.2]). Detailed information about chemical behavior is given in [14.2].

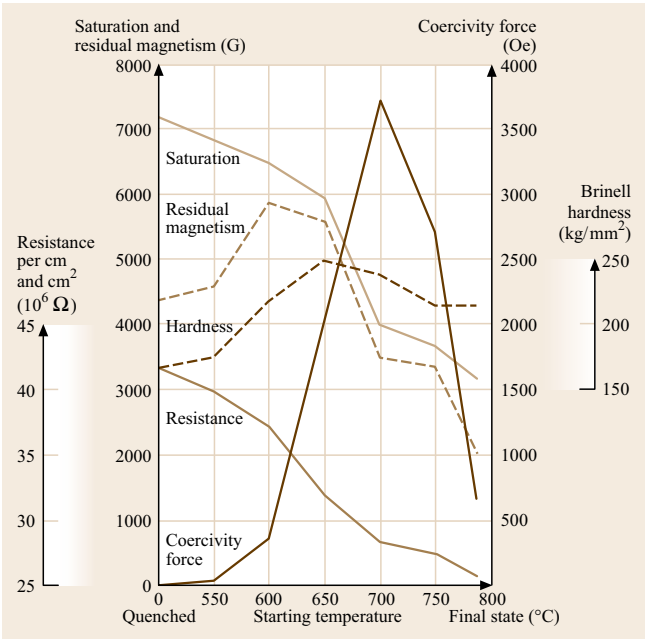


**Fig. 14.108** Change of magnetic properties of PtCo50 alloy by annealing (after [14.5])

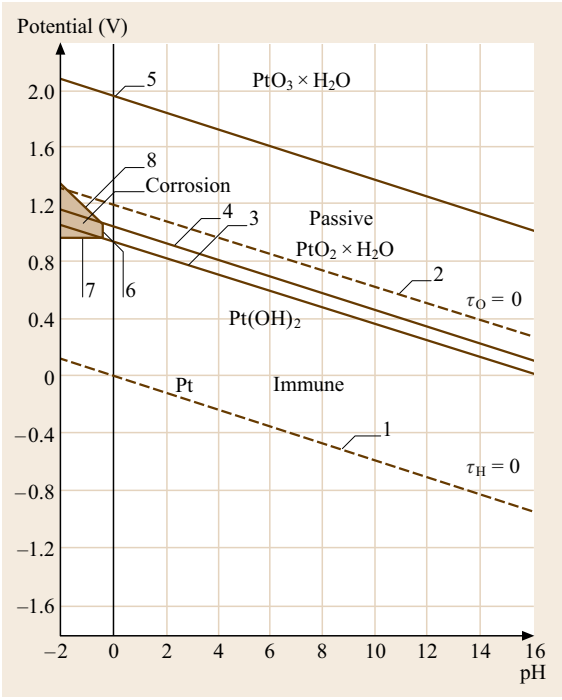


**Fig. 14.109** Potential–pH-diagram of the system $Pt/H_2O$ at 25 °C (Table 14.120) (after [14.2])

**Table 14.120** Reaction and potentials corresponding to graphs of Fig. 14.109 (after [14.2])

| Number | Reaction | Potential $E_0$ (V) |
|---|---|---|
| 1 | $2H^+ + 2e^- \rightarrow H_2$ | $0.000 - 0.0591pH$ |
| 2 | $2H_2O \rightarrow O_2 + 4H^+ + 4e^-$ | $1.228 - 0.0591pH$ |
| 3 | $Pt + 2H_2O \rightarrow Pt(OH)_2 + 2H^+ + 2e^-$ | $0.980 - 0.0591pH$ |
| 4 | $Pt(OH)_2 \rightarrow PtO_2 + 2H^+ + 2e^-$ | $1.045 - 0.0591pH$ |
| 5 | $PtO_2 + H_2O \rightarrow PtO_3 + 2H^+ + 2e^-$ | $2.000 - 0.0591pH$ |
| 6 | $Pt + H_2O \rightarrow PtO + 2H^+$ | $\log[Pt^{2+}] = -7.06 - 2pH$ |
| 7 | $Pt \rightarrow Pt^{2+} + 2e^-$ | $1.188 + 0.0259 \log[Pt^{2+}]$ |
| 8 | $Pt^{2+} + 2H_2O \rightarrow PtO_2 + 4H^+ + 2e^-$ | $0.837 - 0.1182pH - 0.0259 \log[Pt^{2+}]$ |

**Table 14.121** Thermodynamic data of Rh (after [14.2])

| $T$ (K) | $c_p$ (J/(K mol)) | $S$ (J/(K mol)) | $H$ (J/mol) | $G$ (J/mol) | $p$ (atm) |
|---|---|---|---|---|---|
| 298.15 | 24.978 | 31.506 | 0 | −9.393 | $1.43 \times 10^{-89}$ |
| 400 | 26.044 | 38.993 | 2.598 | −13 | $6.59 \times 10^{-65}$ |
| 800 | 39.155 | 58.333 | 13.853 | −32.813 | $7.21 \times 10^{-29}$ |
| 1400 | 35.195 | 76.556 | 33.532 | −73.646 | $1.71 \times 10^{-13}$ |

$T$ = temperature, $c_p$ = specific heat capacity, $S$ = entropy, $H$ = enthalpy, $G$ = free enthalpy, $p$ = partial pressure of the pure elements

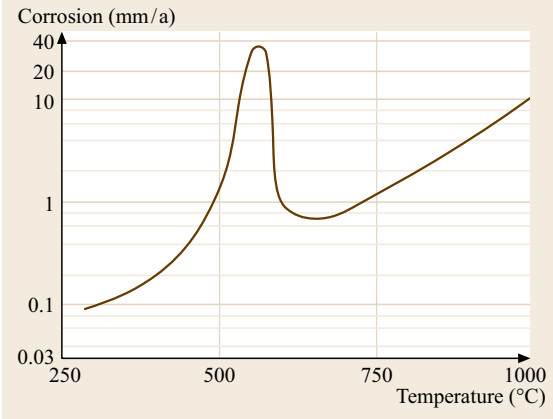


**Fig. 14.110** Corrosion of Pt in dry $Cl_2$ gas (after [14.2])

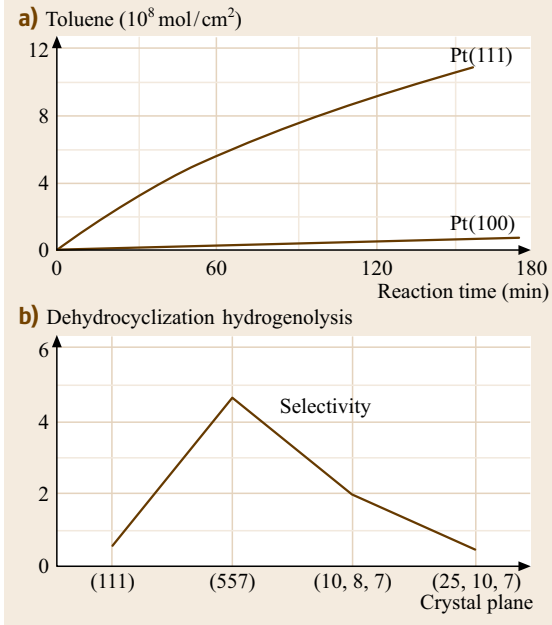


**Fig. 14.111** **(a)** Rate of reaction of *n*-heptane dehydrocyclization to toluene on Pt(111) and Pt(100). **(b)** Variation of selectivity at different crystal planes (after [14.3])

Platinum reacts with ZrC to form $Pt_3Zr$. It also reacts in the presence of hydrogen with $ZrO_2$, $Al_2O_3$, and rare earth oxides at temperatures between 1200 and 1500 °C [14.43, 63]. The solubility of oxygen in platinum is very low. Thin coatings of Pt on reactive materials are an effective protection against oxidation. Alloying of Pt with 2 wt% or higher Al improves the oxidation resistance up to 1400 °C by forming protective dense oxide coatings [14.66]. Superalloys that are Pt-Al-based have high compression strength at high temperatures. Third alloying elements (e.g., Ru) stabilize the high-temperature phase down to room temperature and affects solid-solution strengthening [14.67].

### Catalysis

Platinum and Pt alloys are preferably applied in heterogeneous catalysis as wire nets or powders with a high specific surface area ranging from 20 to 1000 $m^2/g$ (*platinum black*, *palladium black*) on carbon or $Al_2O_3$ supports. The catalytic effectivity is structure-sensitive. Figure 14.111 show an example of the catalytic action of Pt for the reaction rate and the product selectivity on different crystal planes [14.3]. Pt-Pd-Rh alloys are the main active constituents of catalytic converters for automobile exhaust gas cleaning.

### Special Alloys

Molybdenum clad with Pt serves as glass handling equipment up to 1200 °C. Binary Pt alloys with 4 at.% Cu, 5 at.% Co, 5 at.% W, and 10 at.% Ir; and ternary alloys of Pt-Pd-Cu and Pt-Pd-Co are standard jewelry alloys. Alloys of Pt-Au and Pt-Au-Rh surpass the strength of pure Pt at 1000 °C and resist wetting of molten glass. The materials PtIr3, PtAu5 are suitable for laboratory crucibles and electrodes with high mechanical stability.

## 14.3.3 Rhodium and Rhodium Alloys

Rhodium is an essential component of catalysts in numerous chemical reactions and automobile exhaust-gas cleaning. In heterogeneous catalysis it is applied in alloyed form, in homogeneous catalysis as complex organic compounds. Rhodium is an alloy component of corrosion- and wear-resistant tools in the glass industry and a constituent in platinum-group-metal-based thermocouples. Rhodium coatings on silverware and mirrors protect them against corrosion. Commercial grades available are powder, shot, foil, rod, plate, and wires with purity from 98–99.5% (ASTM B 616-78; reappraised 1983).

### Production

Rhodium is produced as powder and sponge by chemical reduction or thermal decomposition of the chloro–ammonia complex $(NH_4)_3[RhCl_6]$. Bars, rods, and wires are produced by powder compacting and extrusion, while coatings are produced galvanically, by evaporation or by sputtering.

### Phases and Phase Equilibria

Selected phase diagrams of Rh are shown in Fig. 14.112a–c. Rhodium forms continuous solid solutions with Fe, Co, Ni, Ir, Pd, and Pt. Miscibility gaps exist in alloys with Fe, Co, Ni, Cu, Ag, Au, Pd, Pt, Ru, and Os. Thermodynamic data are given in Table 14.121 (Table 14.76) and the maximum hydrogen inclusion is listed in Table 14.79.

The compositions and crystal structures of intermediate compounds are shown in Table 14.122 (Table 14.82 for superlattice structures).

### Mechanical Properties

Characteristic mechanical data of Rh are given in Tables 14.123–14.126 and Figs. 14.113–14.117. The modulus of rigidity $G = 153$ GPa; Poisson's ratio $\nu = 0.26$; the elastic constants are $c_0 = 413$, $c_{12} = 194$, and $c_{44} = 184$. Rhodium is very hard but can be deformed at temperatures above 200 °C. For strong hardening by deformations, repeated annealing is needed at temperatures higher than 1000 °C. Rhodium is an effective hardener in Pd and Pt alloys.

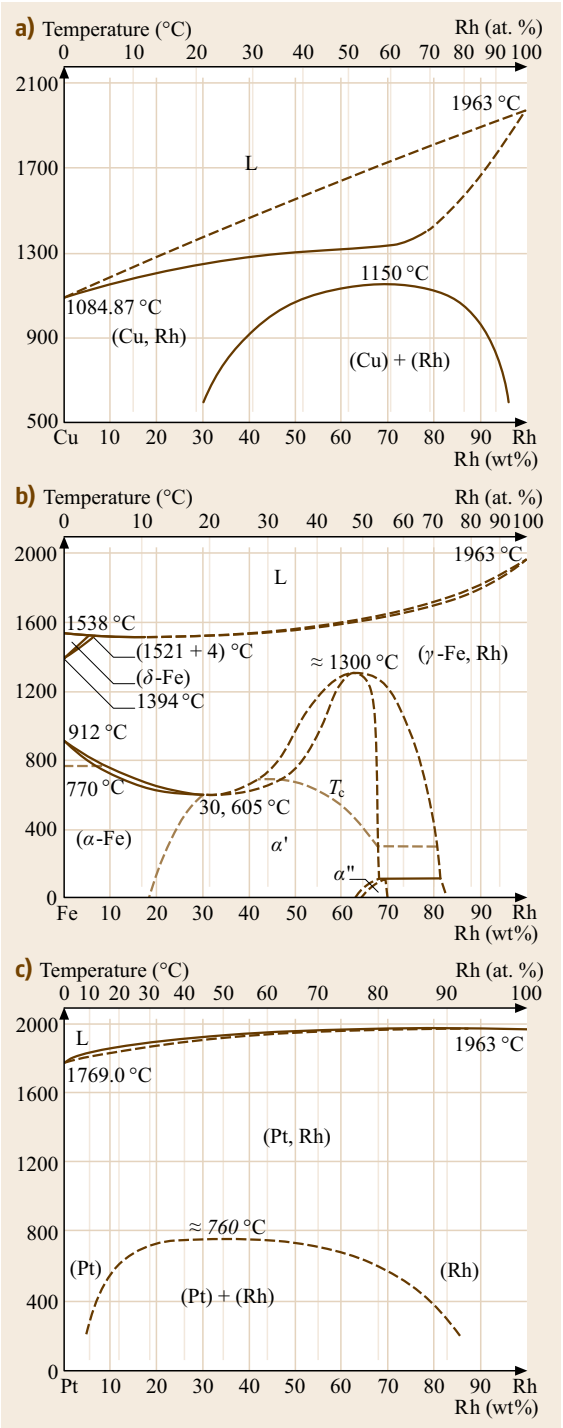


**Fig. 14.112a–c** Phase diagrams of Rh alloys with **(a)** Cu, **(b)** Fe, and **(c)** Pt (after [14.1])

**Table 14.122** Structure and lattice parameter of selected Rh compounds (after [14.2])

| Phase | Pearson symbol | *a* (nm) | *b* (nm) | *c* (nm) | Concentration $xA_{1-x}B_x$ |
|---|---|---|---|---|---|
| Cu-Rh | *cF*4 | 0.3727 | | | 0.5 |
| Fe-Rh | *cI*2 | 0.288885 | | | |
| Fe-Rh | *cF*4 | 0.374 | | | 0.5 |
| Fe-Rh | *cP*2 | 0.2998 | | | |
| Fe-Ru | *hP*2 | 0.258 | | 0.414 | 0.2 |
| Ni-Rh | *cF*4 | 0.36845 | | | 0.494 |

**Table 14.123** Mechanical properties of Rh (99%) at different temperatures (after [14.2])

| *T* (°C) | *E* (GPa) | $R_m$ (MPa) | *A* (%) | $R_{p0.2}$ (MPa) | HV |
|---|---|---|---|---|---|
| 20 | 386 | 420 | 9 | 70 | 130 |
| 500 | 336 | 370 | 19 | 80 | 91 |
| 700 | 315 | 340 | 16 | 40 | 73 |
| 1000 | – | 120 | 10 | 30 | 52 |

*A* = elongation of rupture, *E* = modulus of elasticity, $R_p$ = limit of proportionality, HV = Vickers hardness, $R_m$ = tensile strength

**Table 14.124** Increase of Rh hardness by cold forming (after [14.2])

| V (%) | HV |
|---|---|
| 0 | 130 |
| 10 | 275 |
| 30 | 50 |
| 50 | 400 |

**Table 14.125** Hardness of Pd/Rh and Pt/Rh alloys as a funtion of composition (after [14.2])

| 2nd metal | HV 5 Content (mass%) | | | | |
|---|---|---|---|---|---|
| | 0 | 20 | 40 | 60 | 80 |
| Pd | 130 | 178 | 235 | 229 | 138 |
| Pt | 130 | 165 | 164 | 145 | 123 |

**Table 14.126** Hardness of Rh-Ni alloys at 300 K (after [14.2])

| Alloy | HV 5 |
|---|---|
| RhNi27 | 275 |
| RhNi40 | 220 |
| RhPd20 | 178 |
| RhPt20 | 165 |

**Table 14.127** Increase of atomic resistivity $\Delta\rho/C$ of Rh (after [14.2])

| Base element | $\Delta\rho/C$ (μΩ cm/at.%) |
|---|---|
| Rh | Co 0.34, Cr 4, Fe 0.6, Mn 1.4 |

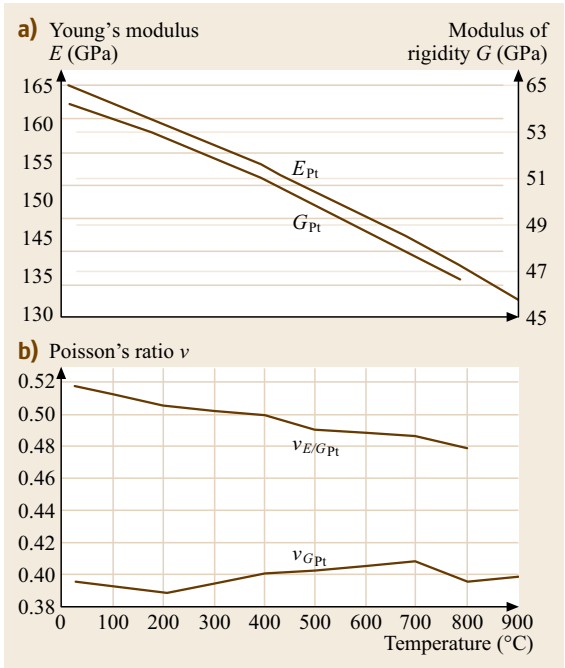


**Fig. 14.113** **(a)** Young's modulus *E* and modulus of rigidity *G* of Pt at different temperatures. **(b)** Poisson's ratio ν for Pt at different temperatures (after [14.68])

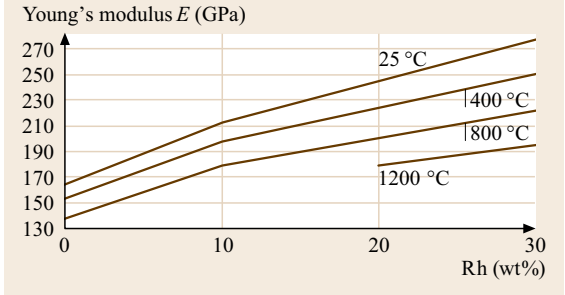


**Fig. 14.114** Young's modulus *E* of as cast Pt/Rh-alloys at various temperatures (after [14.68])

### Electrical Properties

Characteristic electrical properties are given in Tables 14.127 and 14.128 (Table 14.89). Rhodium shows superconductivity below 0.9 K [14.1]. Superconducting Rh alloys are shown in Table 14.129. Among the three-element alloys containing precious metals there exists a special group known as magnetic superconductors [14.3]. Figure 14.118 shows as example the alloy ErRh4B4 with the coexistence of superconductivity and magnetic order changing in the region below the critical temperature of beginning superconductivity [14.3]. Data for light and thermoelectric emission are given in Table 14.130.

**Fig. 14.116** **(a)** Young's modulus $E$ of Pt/Rh-10, Pt/Rh-20, and Pt/Rh-30 alloys at different temperatures. **(b)** Modulus of rigidity $G$ of Pt/Rh-10, Pt/Rh-20, and Pt/Rh-30 alloys at different temperatures. **(c)** Poisson's ratio of Pt/Rh-10, Pt/Rh-20, and Pt/Rh-30 alloys at different temperatures (after [14.68]) ►

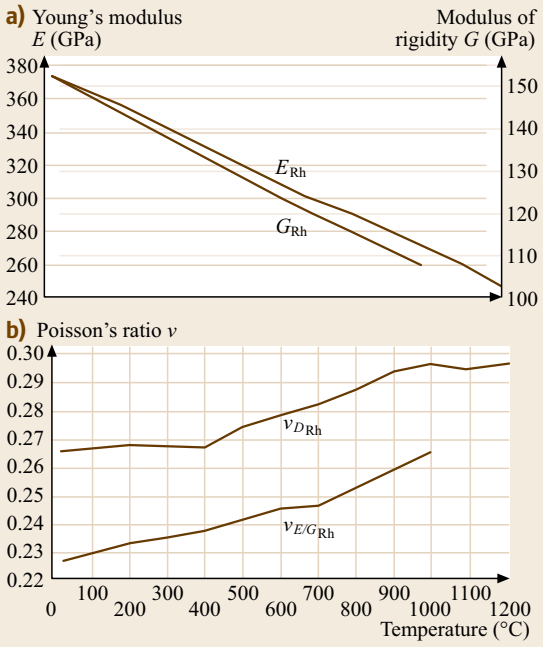


**Fig. 14.115** **(a)** Young's modulus $E$ and the modulus of rigidity $G$ of forged Rh at different temperatures. **(b)** Poissons ratio for forged Rh at different temperatures (after [14.68])

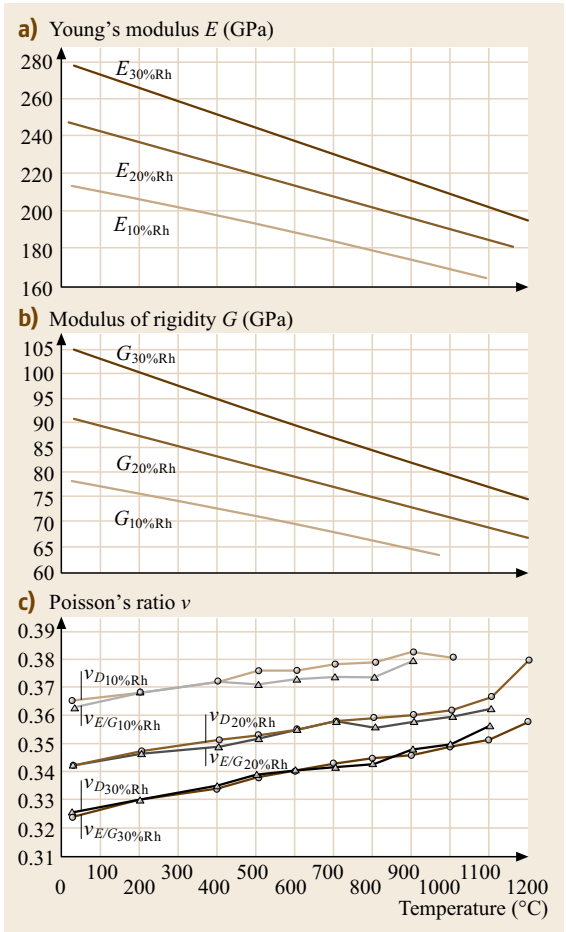


**Table 14.128** Specific electrical resistivity $\rho_i(T)$ of Rh at temperature $T$ ($\rho_0 = 0.0084\,\mu\Omega$ cm) (after [14.2])

| $T$ (K) | 25 | 70 | 160 | 273 | 500 | 1250 | 1750 |
|---|---|---|---|---|---|---|---|
| $\rho_i$ ($\mu\Omega$ cm) | 0.0049 | 0.34 | 2.12 | 4.3 | 9.20 | 26.7 | 40.9 |

**Table 14.129** Superconducting Pd, Pt, and Rh alloys (after [14.3])

| Pd, Pt | | Rh | |
|---|---|---|---|
| **Compound** | **$T_c$ (K)** | **Compound** | **$T_c$ (K)** |
| PtNb3 | 10.6 | Rh2P | 1.3 |
| Pd1.1Te | 4.07 | Rh4P3 | 2.5 |
| PdTe1.02 | 2.56 | ErRhB4 | 8.5 |
| PdTe2 | 1.69 | | |

**Table 14.130** Light and thermoelectric emission of Rh, Pd, and Pt (after [14.5])

| Metal | Light-electric constants | | Temperature (°C) | Thermoelectric work function (V) |
|---|---|---|---|---|
| | Wavelength limit (Å) | Work function (V) | | |
| Rh | 2500 | 4.57 | 20 | 4.58 (at 1550 K abs.) |
| | 2700 | – | 240 | |
| Pd | 2490 | 4.96 | RT | 4.99 (at 1550 K abs.) |
| Pt | 1962 | 6.30 | RT | 6.37 (at 1550 K abs.) |

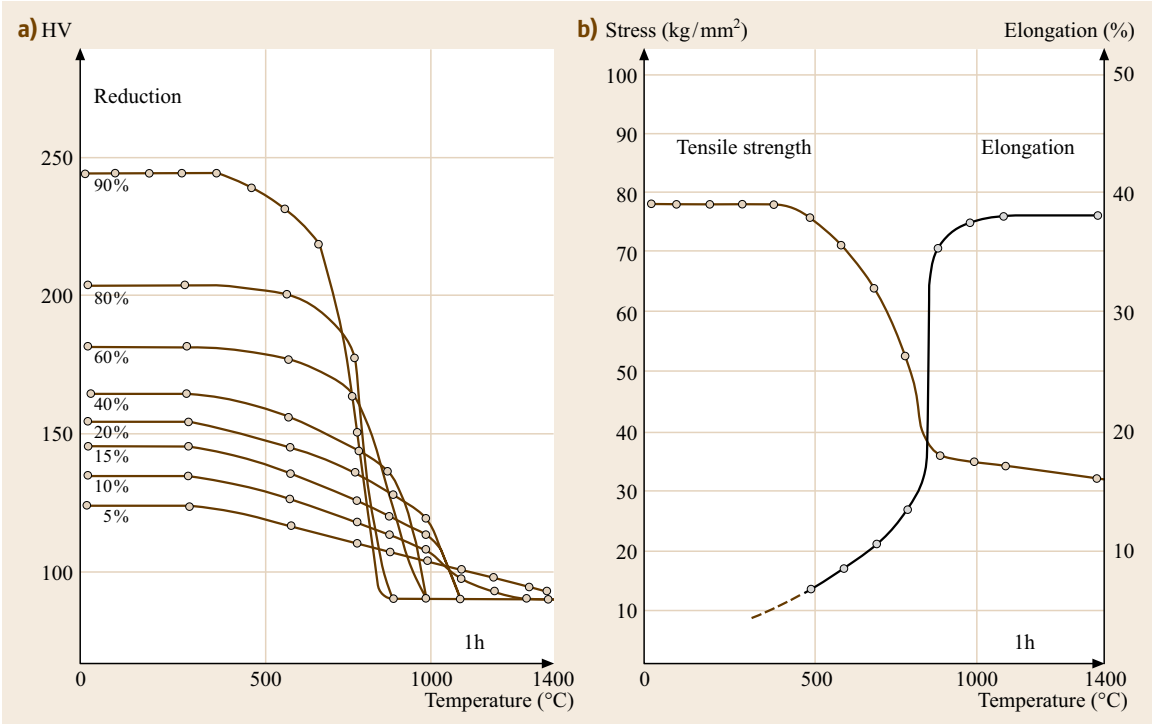


**Fig. 14.117** **(a)** Vickers hardness of Pt/Rh-10 as a function of reduction (%) and various annealing temperatures (after [14.3]). **(b)** Mechanical properties of Pt/Rh-10 alloy (after [14.3])

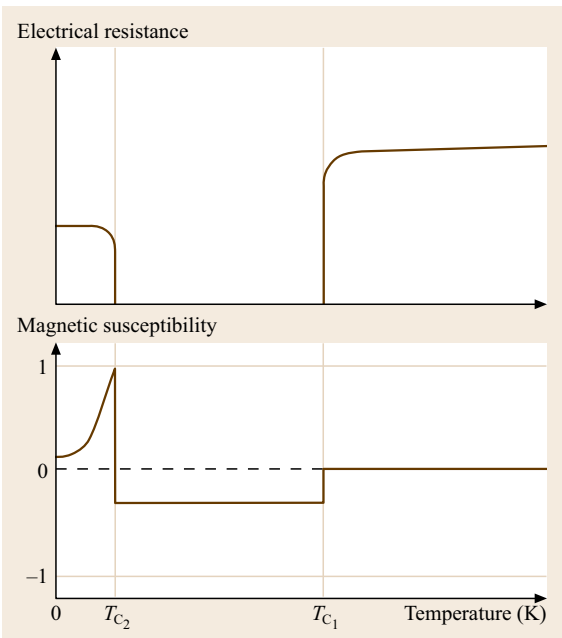


**Fig. 14.118** Coexistence of superconductivity and magnetic order in ErRh4B4 (after [14.3])

### Thermoelectrical Properties

Table 14.91 gives data for the absolute thermoelectric power; Tables 14.131 and 14.132 give the thermal electromotive force of Rh and of Rh-Ni alloys at different temperatures. Rh is also used as a component in Pt-based thermocouples (Tables 14.113, 14.114, and 14.116, Fig. 14.106).

### Magnetical Properties

Data of the magnetic susceptibility of Rh and Rh alloys are given in Figs. 14.82, 14.83, and 14.119–14.122. For magnetostriction data see Table 14.96. The superlattice alloy Fe-Rh shows a transition from the antiferro- to the ferromagnetic state near room temperature (Fig. 14.122) [14.3] where small additions of Pd, Pt, Ir, Ru, or Os enhance this effect.

### Thermal Properties

Tables 14.97–14.99 show the recrystalization temperature, thermal conductivity and thermal expansion at different temperatures. Vapor pressure at different temperatures is shown in Fig. 14.84.

**Table 14.131** Thermal electromotive force of Rh at different temperatures (after [14.2])

| $T$ (°C) | −200 | −100 | +100 | +400 | +800 | +1000 | +1300 |
|---|---|---|---|---|---|---|---|
| $E_{Rh,Pt}$ (mV) | −0.23 | −0.32 | +0.70 | +3.92 | +10.16 | +14.05 | +20.34 |

**Table 14.132** Thermal electromotive force of Rh/Ir alloys at different content (after [14.2])

| $T$ (°C) | Composition (wt%) | | | | |
|---|---|---|---|---|---|
| | 10 | 30 | 50 | 70 | 90 |
| 1000 | 15.15 | 17.40 | 18.40 | 17.75 | 15.45 |

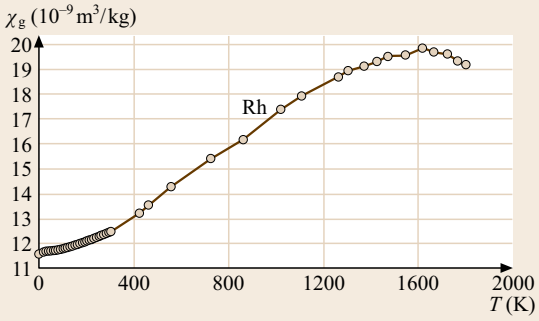


**Fig. 14.119** Temperature dependence of the mass susceptibility $\chi_g$ of Rh (after [14.2])

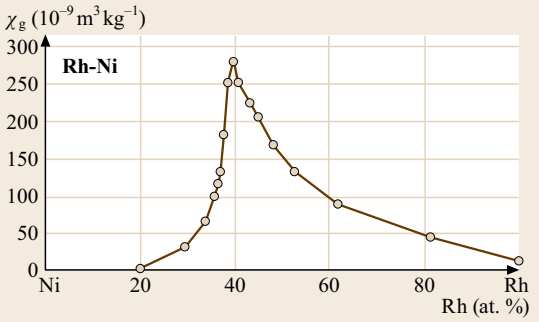


**Fig. 14.120** Mass susceptibility $\chi_g$ of Rh-Ni alloys as a function of alloy composition at 4.2 K (after [14.2])

### Optical Properties

Rhodium has the highest optical reflectivity of all platinum-group metals (Fig. 14.85), ranging about 20% below the reflectivity of Ag. It is used as hard and corrosion-resistant coating on silver jewelry and for optical reflectors. Data of the spectral emissivity are given in Table 14.101.

### Diffusion

Data for self-diffusion are given in Table 14.102 ([14.1] for further data).

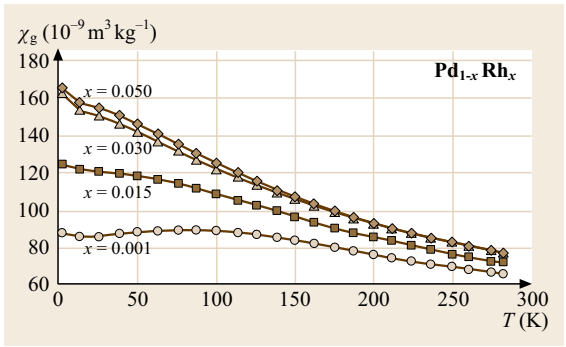


**Fig. 14.121** Mass susceptibility $\chi_g$ of binary Pd-Rh alloys as a function of alloy composition (after [14.2])

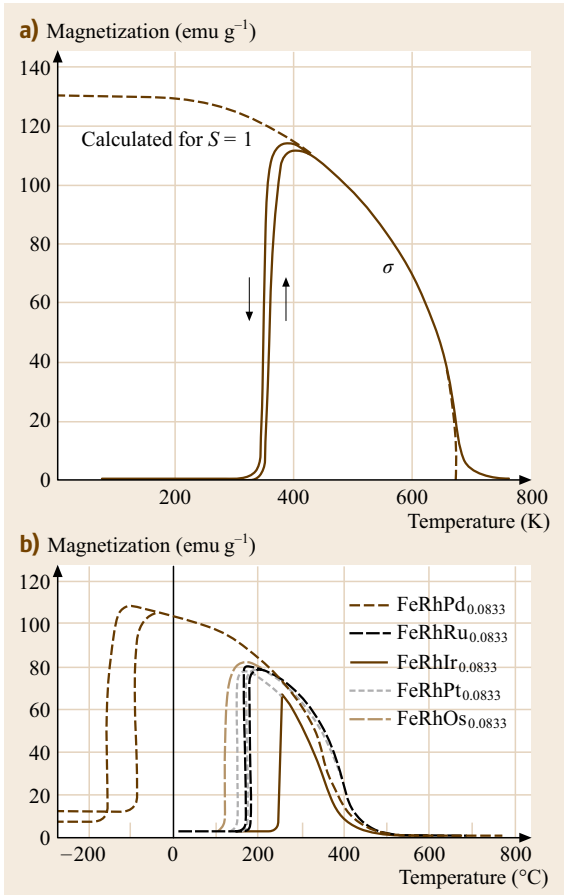


**Fig. 14.122a,b** Metamagnetic behavior of **(a)** Fe-Rh superlattice alloy (after [14.3]). **(b)** Variation by addition of small amounts of Pd, Ru, Ir, Pt, Os (after [14.3])

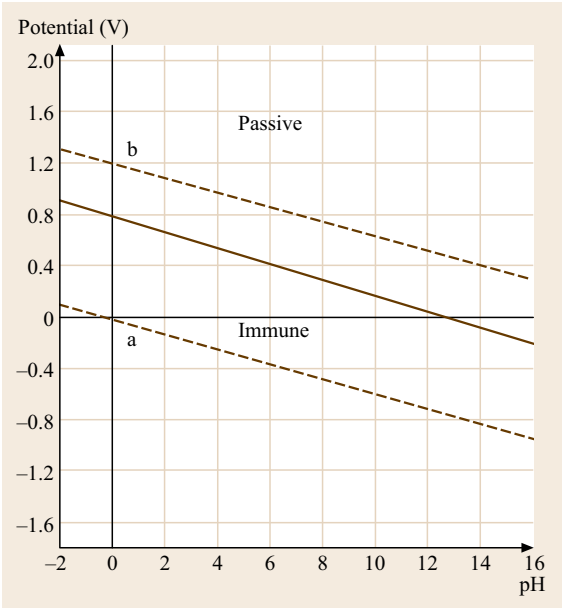


**Fig. 14.123** Potential–pH-diagram for the system Rh-$H_2O$ (after [14.2])

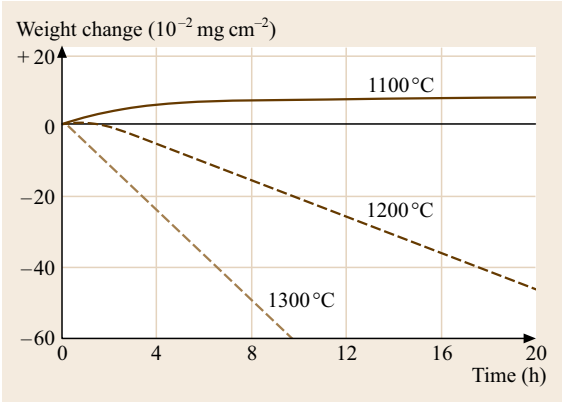


**Fig. 14.124** Weight change of Rh in oxygen (after [14.2])

### Chemical Properties

Rhodium is not attacked by acids or alkali even under oxidizing conditions (aqua regia) (Fig. 14.123). Sodium hypochlorite attacks in the order of increasing strength: Pt = Rh = Ir = Ru < Pd < Os. Heating in air causes the formation of thin oxide layers above 600 °C which decompose above 1100 °C (Fig. 14.124). Pt alloys with 5–40 wt% Rh are corrosion-resistant against $H_2F_2$. A detailed survey about these chemical properties is given in [14.1].

Rhodium is the effective component of the three-way Pt/Pd/Rh alloy autocatalyst for the reduction of $NO_x$ of exhaustion gases (Fig. 14.125a,b). Rh-catalysts

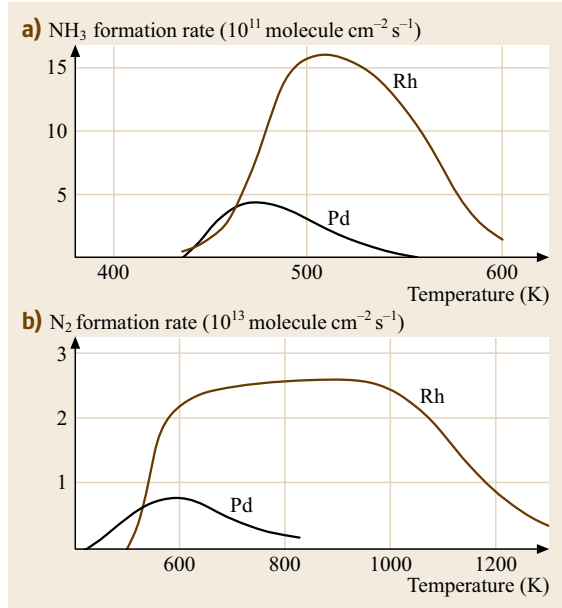


**Fig. 14.125a,b** Product formation rates in N = –$H_2$ reactions on Pd- and Rh-catalyst foils. **(a)** $NH_3$ formation rates $p(NO) = 9.4 \times 10^{-5}$ Pa, $p(H_2) = 4.9 \times 10^{-5}$ Pa. **(b)** $N_2$ formation rates $p(NO) = 1.1 \times 10^{-5}$ Pa, $p(H_2) = 1.9 \times 10^{-5}$ Pa (after [14.3])

surpass the group homolog, Co-based catalysts, with lower reaction pressures and temperatures and higher yields [14.1]. Complex organic rhodium compounds on the basis of $RhCl(PPh_3)$ with different substitute ligands are important homogeneous catalysts in the technical production processes for hydrogenation and hydroformulation (*oxo*-processes, e.g., synthesis of aldehydes and acetic acid). Replacement of $PPh_3$ by complex chiral phosphan ligands enables the synthesis of asymmetric compounds, e.g., L-DOPA and L-menthol (Fig. 14.126a,b) [14.69].

## 14.3.4 Iridium and Iridium Alloys

Iridium is used for crucibles to grow high-purity crystals for lasers, medical scanners etc. anodes to prevent corrosion of shipping vessels and under-water structures, coatings of electrodes for the manufacturing of chlorine and caustic soda, as an alloy component of automotive exhaust catalysts, and as alloy component and compounds of chemical process catalysts for the production of acetic acid and complex organic compounds. Iridium is an effective hardener for materials used at high temperature, high wear, and high corrosion conditions (e.g., spark plugs). It is also used as fine-grain forming addition in jewelry and dental gold

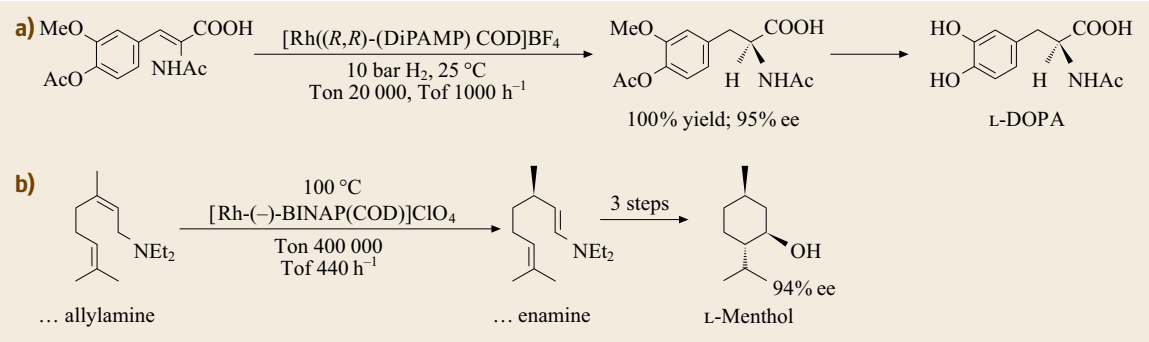


**Fig. 14.126a,b** Examples of organic synthesis of chiral compounds catalysed by complex Rh compounds. **(a)** L-DOPA, **(b)** L-menthol (after [14.69])

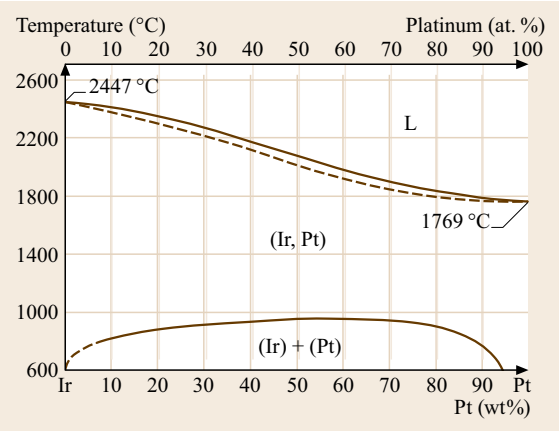


**Fig. 14.127** Phase diagram of Ir-Pt (after [14.2])

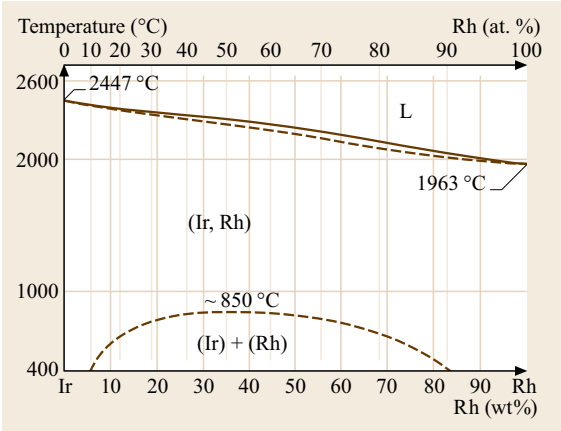


**Fig. 14.128** Phase diagram of Ir-Rh (after [14.2])

alloys. Commercial grades available are powder, shot, ingot, and wire in a purity ranging from 98% to 99.9% (ASTM 671-81, reappraised 1987).

### Production

Iridium is produced as powder and sponge by chemical reduction or thermal decomposition of the chloroammonia compound $(NH_4)_2[IrCl_6]$. Bars, rods, ingot, and wires are produced by compacting of powder followed by extrusion. Coatings are produced galvanically, by evaporation, or by sputtering.

### Phases and Phase Equilibria

Figures 14.127–14.129 [14.1] show the binary phase diagrams of Ir alloys with Pt, Rh, and Ru. Miscibility gaps exist in the solid state also in the alloy systems with Cu, Os, Re, and Ru. Iridium alloyed in Fe lowers the $\alpha \rightarrow \lambda$ transition temperature considerably (Fig. 14.153). Thermodynamic data are given in Table 14.133 [14.1].

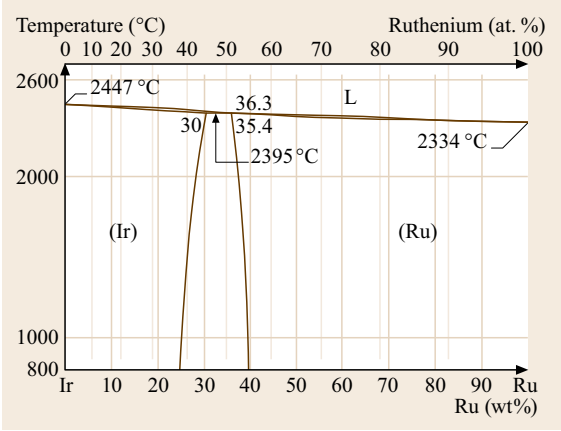


**Fig. 14.129** Phase diagram of Ir-Ru (after [14.2])

Structure and lattice parameters of selected intermediate compounds are given in Table 14.134 [14.1].

**Table 14.133** Thermodynamic data of Ir (after [14.2])

| $T$ (K) | $c_p$ (J/(K mol)) | $S$ (J/(K mol)) | $H$ (J/mol) | $G$ (J/mol) | $p$ (atm) |
|---|---|---|---|---|---|
| 298.15 | 24.979 | 35.505 | 0 | −10.586 | |
| 400 | 25.695 | 42.946 | 2.581 | −14.598 | $6.70\times10^{-80}$ |
| 800 | 28.51 | 61.62 | 13.442 | −35.875 | $2.81\times10^{-36}$ |
| 1400 | 32.733 | 78.647 | 31.795 | 78.311 | $1.15\times10^{-17}$ |

$T$ = temperature, $c_p$ = specific heat capacity, $S$ = entropy, $H$ = enthalpy, $G$ = free enthalpy, $p$ = partial pressure of the pure elements

**Table 14.134** Structure and lattice parameter of intermediate compounds (after [14.2])

| Phase | Pearson symbol | $a$ (nm) | $b$ (nm) | $c$ (nm) | Concentration $x$ $A_{1-x}B_x$ |
|---|---|---|---|---|---|
| Cu-Ir | *cF*4 | 0.3629 | | | |
| Ir-Os | *hP*2 | 0.27361 | | 0.43417 | 0.65 |
| Ir-Os | *cF*4 | 0.38358 | | | 0.2 |
| Ir-Rh | *cF*4 | 0.3824 | | | 0.5 |
| Ir-Ru | *hP*2 | 0.2718 | | 0.4331 | 0.56 |
| Ir-Ru | *cF*4 | 0.3818 | | | 0.47 |

**Table 14.135** Modulus of elasticity in crystal direction (after [14.2])

| $E$ ⟨110⟩ | $E$ ⟨111⟩ |
|---|---|
| 47.4 GPa | 662 GPa |

**Table 14.136** Elastic constants of Ir (after [14.2])

| | | | |
|---|---|---|---|
| $T = 300$ K | $c_{11} = 580$ | $c_{12} = 242$ | $c_{44} = 256$ |

**Table 14.137** Mechanical properties of Ir at different temperatures (after [14.2])

| $T$ (°C) | $E$ (GPa) | $R_m$ (MPa) | $A$ (%) | $R_{p0.2}$ (MPa) | | HV |
|---|---|---|---|---|---|---|
| 20 | 538 | 623 | 6.8 | 234 | | 200 |
| 500 | 488 | 530 | 9 | 12.7 | 234 | 138 |
| 800 | 456 | 450 | 18 | 51 | 142 | 112 |
| 1000 | 434 | 331 | – | 80.6 | 43.4 | 97 |

$A$ = elongation of rupture, $E$ = modulus of elasticity, $R_p$ = limit of proportionality, HV = Vickers hardness, $R_m$ = tensile strength

**Table 14.138** Change of hardness of Ir by degree cold forming (after [14.2])

| $V$ (%) | HV |
|---|---|
| 0 | 240 |
| 10 | 425 |
| 20 | 485 |
| 30 | 475 |
| 59 | 590 |

## Mechanical Properties

Iridium is extremely hard and can only be deformed at temperatures above 600 °C, with repeated annealing steps at temperatures higher than 1200 °C. The Young's modulus is different for different crystal directions (Table 14.135) [14.1], the modulus of rigidity is 214 GPa, and the Poisson's ratio amounts to 0.26.

Characteristic data of mechanical properties of Ir and Pt/Ir alloys are given in Tables 14.136–14.138 [14.1] and Figs. 14.130–14.132 [14.68]. Two-phase Ir-based refractory superalloys with fcc and $L1_2$ structure of the components (Ir-12Zr, Ir-17Nb, and Ir-15Nb-5Ni) have resist temperatures up to 1200 °C and exhibit marked creep resistance (Figs. 14.133–14.135) [14.7, 70].

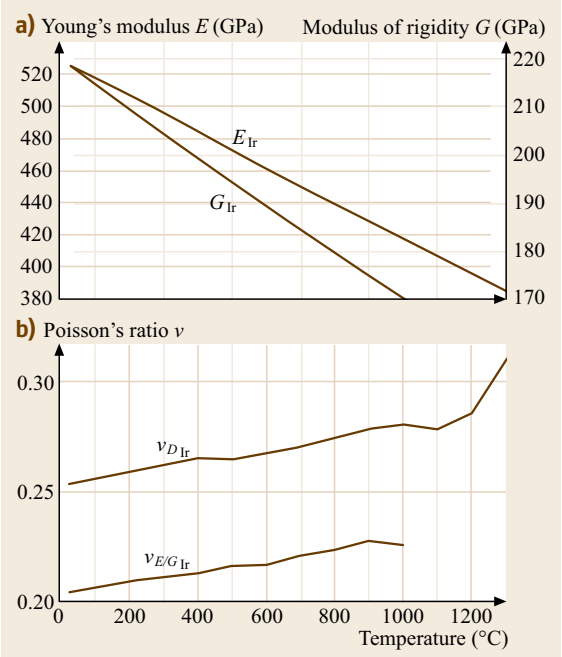


**Fig. 14.130** (a) Young's modulus $E$ and modulus of rigidity $G$ of Ir at different temperatures. (b) Poisson's ratio $\nu$ for as cast Ir at different temperatures (after [14.68])

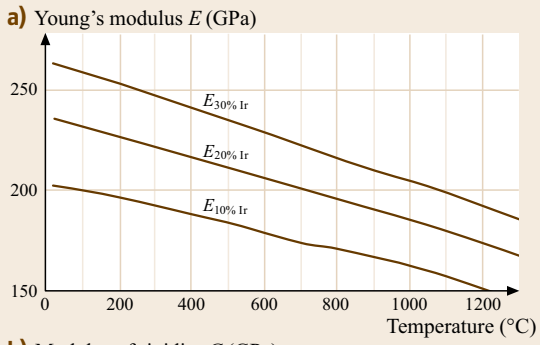


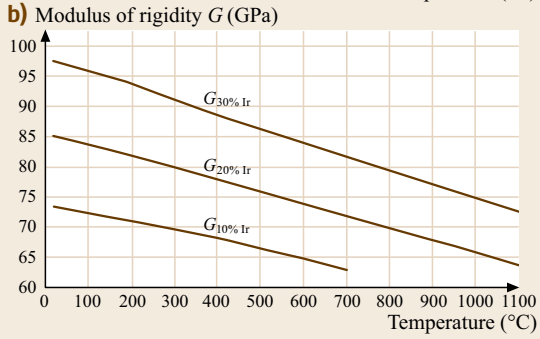


**Fig. 14.131** **(a)** Young's modulus $E$ of Pt-Ir alloys at different temperatures. **(b)** Modulus of rigidity $G$ of as cast Pt-Ir alloys at different temperatures (after [14.68])

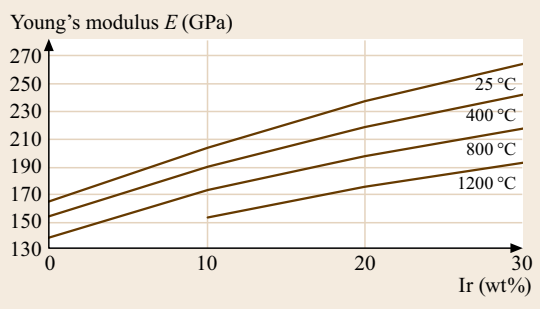


**Fig. 14.132** Young's modulus $E$ of as cast Pt-Ir alloys at different temperatures (after [14.68])

### Electrical Properties

The residual resistance ratio (RRR) amounts to 85 (Table 14.89). The specific electrical resistivity at different temperatures and the dependence of the atomic resistivity are given in Tables 14.139 and 14.140 [14.1].

Iridium becomes superconducting below 0.11 K. Some ternary alloys show critical transition temperatures between 3 and above 8 K (Table 14.141) [14.3].

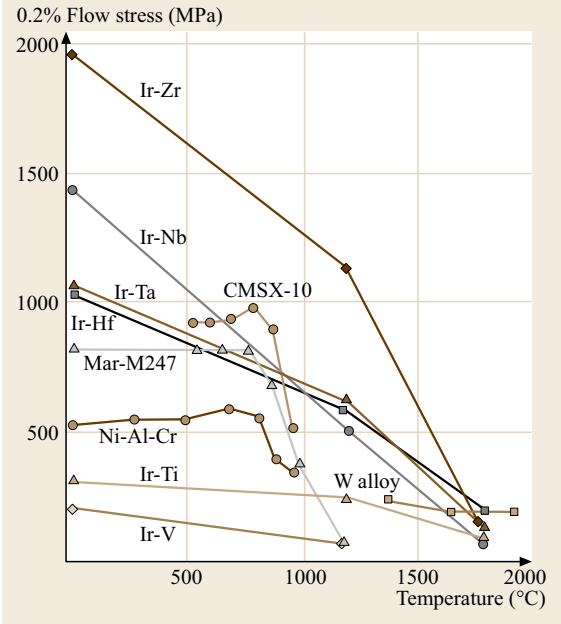


**Fig. 14.133** High-temperature compression strength of selected Ir-based alloys (after [14.67])

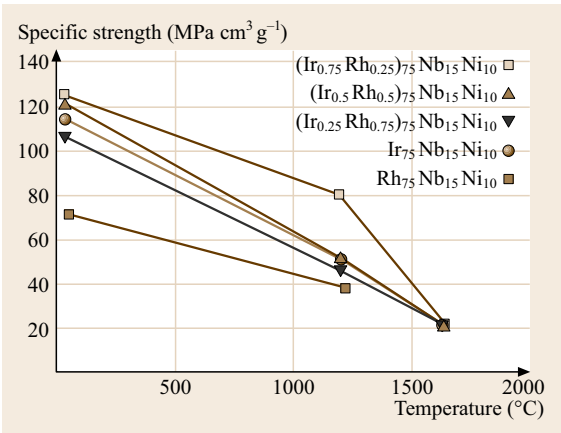


**Fig. 14.134** Specific strength of Ir-Rh-Nb alloys (after [14.70])

### Thermoelectrical Properties

Data for the absolute thermoelectric power and the thermoelectric voltage of Ir, and the thermoelectric voltage of Ir-Rh alloys are shown in Tables 14.91–14.93, and 14.142 [14.1] and Fig. 14.136 [14.2].

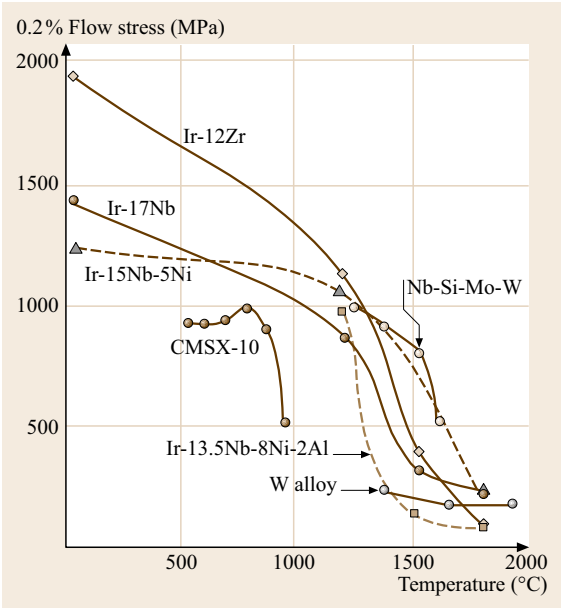


**Fig. 14.135** Comparison of compressive strength of Ir alloys versus W and Nb-Mo alloys at various temperatures (after [14.70])

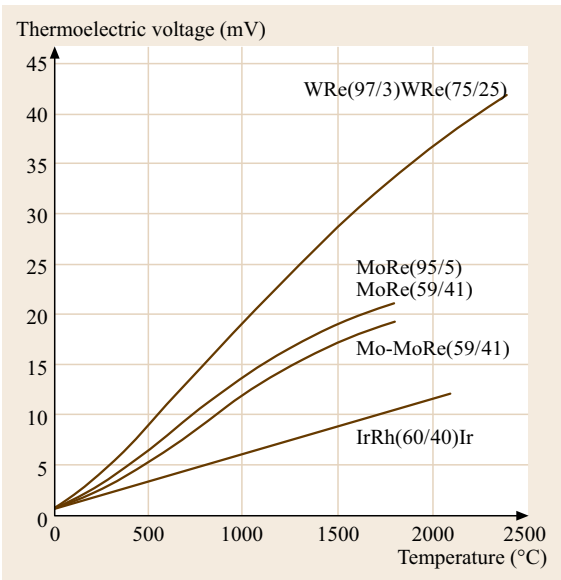


**Fig. 14.136** Thermoelectric voltage of Ir-Rh alloys compared to Mo-Re and W-Re alloys (after [14.2])

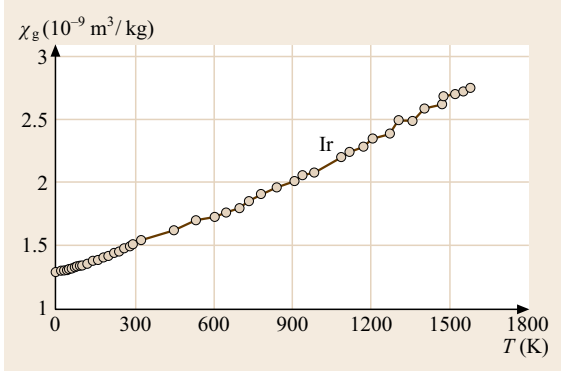


**Fig. 14.137** Mass susceptibility $\chi_g$ of Ir at different temperatures (after [14.2])

**Table 14.139** Specific electrical resisitivity of Ir at different temperatures ($\rho_i(T) = \rho_0 + \rho_i(T)$; $\rho_0 = 0.10\,\mu\Omega\,\text{cm}$) (after [14.2])

| $T$ (K) | 15 | 40 | 140 | 273 | 700 | 1100 | 1500 |
|---|---|---|---|---|---|---|---|
| $\rho_i(T)$ | 0.0013 | 0.10 | 1.96 | 4.65 | 13.90 | 23.20 | 34.02 |

**Table 14.140** Increase of atomic electrical resistivity (after [14.2])

| Base element | $\Delta\rho/C$ ($\mu\Omega$ cm/at.%) |
|---|---|
| Ir | Pt 1.33, Re 2.7, Cr 2, Mo 3.65, W 3, Fe 0.6 |

**Table 14.141** Superconducting Ir alloys (after [14.3])

| Alloy | $T_c$ (K) |
|---|---|
| IrTe3 | 1.18 |
| Sc5Ir4Si10 | 8.46–8.38 |
| Y5Ir4Si10 | 3.0–2.3 |
| Lu5Ir4Si10 | 3.76–3.72 |

### Magnetic Properties

Iridium is paramagnetic. Figures 14.82, 14.137, and 14.138 [14.1] show the mass susceptibility of Ir and Pt-Ir alloys at different temperatures. Iridium exhibits magnetostriction according the equation $\Delta l/l = S_l H^2$, with $S_l = +3.8$ (Table 14.96).

### Thermal Properties

Tables 14.97–14.99 give selected data for the recrystallization temperature (varying by purity, degree of cold forming, and annealing time), thermal conductivity, and thermal expansion coefficient.

**Table 14.142** Thermoelectric voltage of Ir at different temperatures (after [14.1])

| $T$ (°C) | −200 | −100 | −50 | +100 | +200 | +400 | +800 |
|---|---|---|---|---|---|---|---|
| $E_{Ir,Pt}$ (mV) | −0.20 | −0.35 | −0.20 | 0.66 | 1.525 | 3.636 | 9.246 |

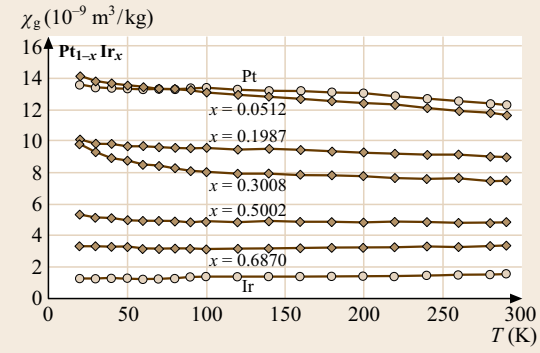


**Fig. 14.138** Mass susceptibility $\chi_g$ of Pt-Ir alloys at different temperatures (after [14.2])

### Optical Properties

The optical reflectivity of Ir is markedly lower than that of Rh increasing in the wavelength range from 0.4 to 0.8 µm (Figs. 14.2 and 14.85). Data of the spectral emissivity are given in Table 14.101.

### Diffusion

Table 14.102 gives only one value for self diffusion of iridium but further information may be obtained from Landolt–Börnstein [14.23].

### Chemical Properties

Iridium is not attacked by acids or alkali even under oxidizing conditions (aqua regia). It forms volatile oxides in air above 1000 °C but it can be heated up to 2300 °C without danger of catastrophic oxidation. Pt alloys with 1–30 wt% Ir are corrosion-resistant against $H_2F_2$. Figures 14.139 and 14.140 [14.1, 16] show data of the evaporation and oxidation behavior of Ir alloys. A detailed survey on the chemical properties is given in [14.1].

Metal-organic Ir compounds are effective homogeneous catalysts for organo-chemical reactions such as hydrogenation and carbonylation. The technical production of acetic acid (*Cativa* process). Figure 14.141 shows an example for different carbonylation rates of Rh- and Ir/Ru-based catalysts [14.71]. Complex organic Ir catalysts have high stereoselectivity in hydrating cyclic alcohols [14.1].

## 14.3.5 Ruthenium and Ruthenium Alloys

Ruthenium is a component of alloys and compounds of chemical process catalysts, and Pt-based catalysts for proton-exchange fuel cells (PEFC). Because of its corrosion resistance, it is used for corrosion-preventing anodes in shipping vessels and under-water structures,

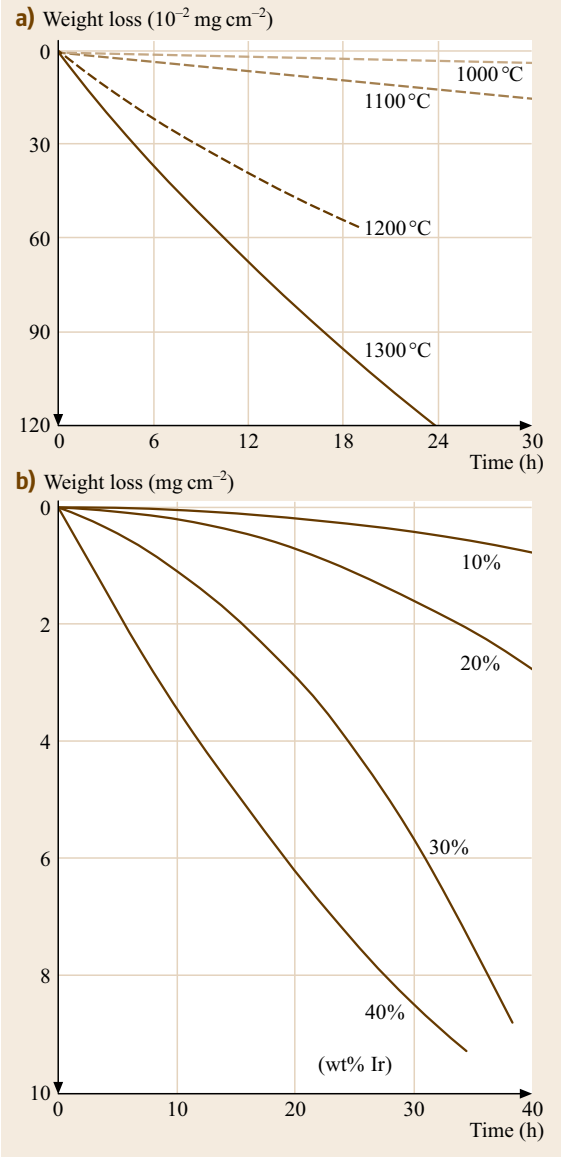


**Fig. 14.139a,b** Evaporation losses. **(a)** Pt loss in oxygen; **(b)** Pt-Ir clad loss in oxygen at 900 °C (after [14.2])

pipelines, in geothermal industries, and as coating of electrodes in chlorine and caustic soda production. Ruthenium oxide ($RuO_2$) and complex Bi/Ba/Pt oxides are materials for electrical resistors. Ruthenium layers on computer hard discs are used for high density data storage improvement of data-storage densities. Ruthenium is an effective hardener of Pd and Pt. Commercial grades available are sponge, powder, grains, and pellets in purity ranging from 99% to 99.95% (ASTM B 717).

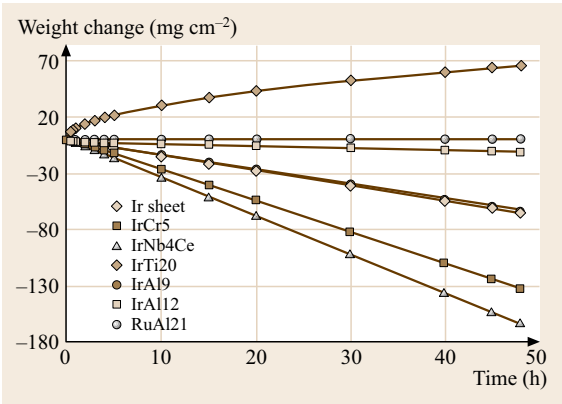


**Fig. 14.140** Oxidation behavior of various Ir alloys at 1000 °C in air (after [14.16])

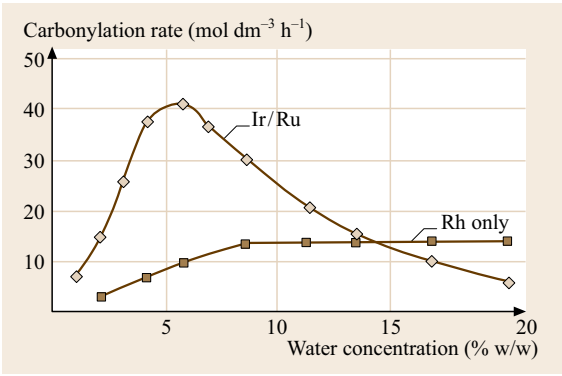


**Fig. 14.141** Carbonylation rates for Ir-Ru and Rh catalysts in methylacetat reactions (after [14.71])

### Production

Production of ruthenium starts with chemical reduction of chloro compounds to powder, followed by compacting to pellets. Coatings are produced by galvanic processing, evaporation or sputtering.

### Phases and Phase Equilibria

Selected phase diagrams are shown in Figs. 14.142–14.144, thermodynamic data are listed in Table 14.143 and molar heat capacities can be found in Table 14.75. Ruthenium alloyed to Fe lowers the $\gamma \rightarrow \alpha$ transition temperature considerably (Fig. 14.153). Table 14.144 gives the structure and lattice parameters of intermediate Co and Fe compounds. The superlattice structures can be found in Table 14.82.

### Mechanical Properties

Ruthenium has a Young's modulus of 485 GPa, the Poisson's ratio amounts to 0.29, and the modulus of rigidity is 172 GPa. Characterisitic properties of Ru are

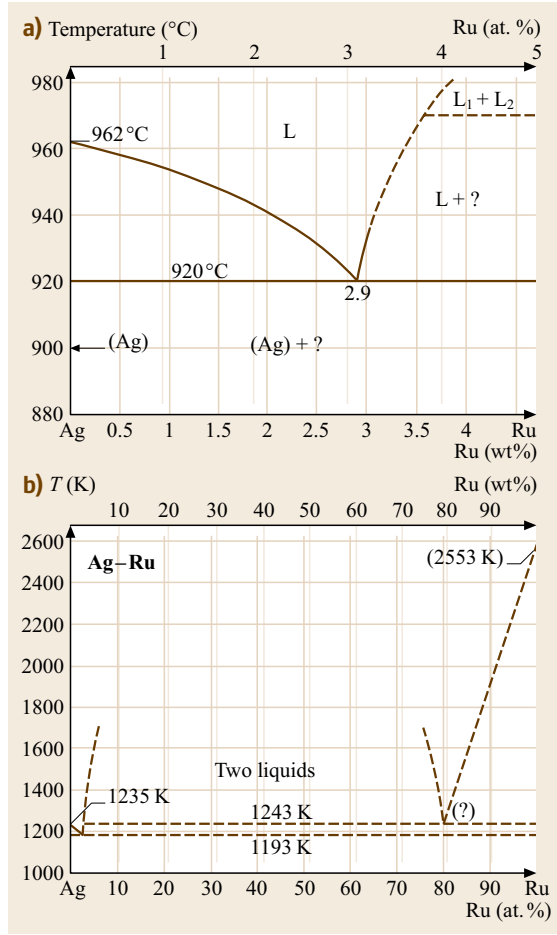


**Fig. 14.142a,b** Phase diagram of Ag-Ru (a) and phase diagram of Ag-Ru in the high-temperature range (after [14.2, 4])

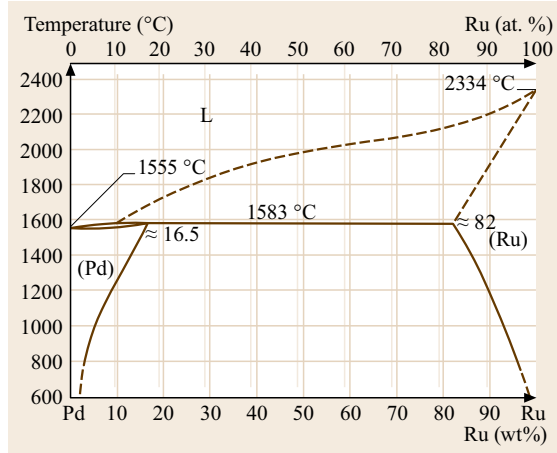


**Fig. 14.143** Phase diagram of Pd-Ru (after [14.2])

**Table 14.143** Thermodynamic data of Ru (after [14.2])

| $T$ (K) | $c_p$ (J/(K mol)) | $S$ (J/(K mol)) | $H$ (J/mol) | $G$ (J/mol) | $p$ (at) |
|---|---|---|---|---|---|
| 298.15 | 23.705 | 28.535 | 0 | −8.508 | |
| 400 | 24.345 | 35.595 | 2.449 | −11.79 | $1.50\times10^{-77}$ |
| 800 | 26.516 | 53.121 | 12.611 | −29.885 | $4.83\times10^{-35}$ |
| 1400 | 30.97 | 69.01 | 29.77 | −66.844 | $7.73\times10^{-17}$ |

$T$ = temperature, $c_p$ = specific heat capacity, $S$ = entropy, $H$ = enthalpy, $G$ = free enthalpy, $p$ = partial pressure of the pure elements

**Table 14.144** Structure and lattice parameter of intermediate compounds (after [14.2])

| Phase | Pearson symbol | $a$ (nm) | $b$ (nm) | $c$ (nm) | Concentration $x$ $A_{1-x}B_x$ |
|---|---|---|---|---|---|
| Co-Ru | *hP*2 | 0.261 | | 0.4181 | 0.5 |
| Co-Ru | *cF*4 | 0.3592 | | | 0.2 |
| Fe-Ru | *cI*2 | 0.2883 | | | 0.06 |
| Fe-Ru | *hP*2 | 0.258 | | 0.414 | 0.2 |
| Os-Ru | *hP*2 | 0.27193 | | 0.4394 | 0.5 |

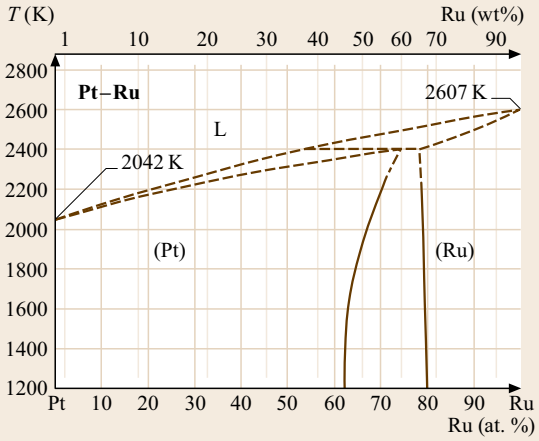


**Fig. 14.144** Phase diagram of Pt-Ru (after [14.4])

given in Tables 14.145 and 14.146. The mechanical properties are marked anisotropic. The hardness of different single crystal faces varies between HV 100 and HV 250 [14.1]. High compression-strength alloys are formed by two-phase Ru-Al intermetallic structures. Figure 14.145 gives an example of molten and hot isostatic-pressed eutectic Ru (Ru-70/Al-30) in relation to the constituent phases [14.6].

### Electrical Properties

The residual resistance ratio (RRR) amounts to 25 000 (Table 14.89). Characteristic electrical properties of Ru are given in Tables 14.89, 14.147, and 14.148. The specific electrical resistivity of $RuO_2$ is $3.5\times10^{-5}\,\Omega$ cm (1 Ω cm for PdO for comparison). Together with its low temperature dependence of the coefficient of resistance,

**Table 14.145** Mechanical properties of Ru at different temperatures (after [14.1, 2])

| $T$ (°C) | $R_m$ (MPa) | $A$ (%) | $R_{p0.2}$ (MPa) | HV |
|---|---|---|---|---|
| 20 | 500 | 3 | 380 | 250–500[a] |
| 750 | 300 | 15 | 230 | 160–280[b] |
| 1000 | 220 (430) | 14 | 190 | 100–200[a] |

[a] At different crystal planes, [b] At 600 °C
$A$ = elongation of rupture, $R_p$ = limit of proportionality, HV = Vickers hardness, $R_m$ = tensile strength

**Table 14.146** Hardness (HV 5) of Pd-Ru and Pt-Ru alloys at 300 K (after [14.2])

| Alloying metal | Alloy content (wt%) 0 | 20 | 40 | 60 | 80 |
|---|---|---|---|---|---|
| Pd | 350 | 412 | 425 | 284 | 243 |
| Pt | 350 | 330 | 446 | 293 | 253 |

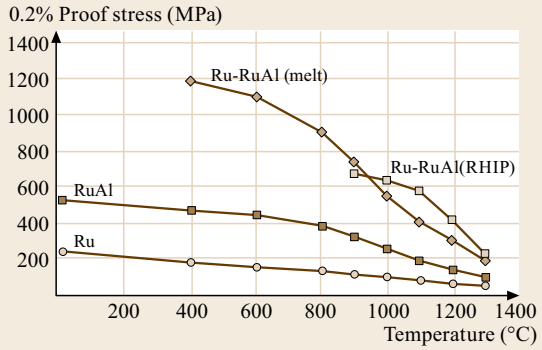


**Fig. 14.145** High-temperature compression strength of eutectic Ru-70/Al-30 in relation to its constituent phases (after [14.67])

Ru is suited for the production of resistors in sintered form or as thick-film layers covering resistors ranging from ≈ 1.5 to 10 MΩ. Conductive components are either $RuO_2$, $Pb_2Ru_2O_6$, or $Bi_2Ru_2O_7$ together with additions of doping oxides [14.3].

Ruthenium shows superconductivity below 0.47 K [14.3]. Ternary alloys have critical transition temperatures up to 12.7 K (Table 14.149).

**Table 14.147** Specific electrical resistivity $\rho_i(T)$ of Ru at different temperatures ($\rho_0 = 0.016\,\mu\Omega\,\text{cm}$) $\rho(T) = \rho_0 + \rho_i(T)$ (after [14.2])

| $T$ (K) | 25 | 50 | 100 | 200 | 273 | 300 | 500 |
|---|---|---|---|---|---|---|---|
| $\rho_i$ ($\mu\Omega$ cm) | 0.005 | 0.105 | 1.25 | 4.38 | 6.69 | 7.43 | 13.2 |

**Table 14.148** Increase of atomic electrical resisitivity by alloying elements $\Delta\rho/C$ (after [14.2])

| Base element | $\Delta\rho/C$ ($\mu\Omega$ cm/at.%) |
|---|---|
| Ru | Fe 0.21, Re 2, Y 1.5 |
| Os | Y 10 |

**Table 14.149** Critical transition temperature of superconducting Ru alloys (after [14.3])

| Alloy | $T_c$ (K) |
|---|---|
| TiRuP | 1.33 |
| ZrRuP | 12.34–10.56 |
| HrRuP | 12.70–11.08 |
| TiRuAs | >0.35 |
| ZrRuAs | 11.90–1.03 |
| HfRuAs | 4.93–4.37 |
| Y3Ru4Ge13 | 1.7–1.4 |
| Lu3Ru4Ge13 | 2.3–2.2 |

### Thermoelectric Properties

Data of thermoelectric properties of Ru are given in Tables 14.91 and 14.150.

### Magnetic Properties

Figures 14.82, 14.146, and 14.147 present data of the magnetic mass susceptibility of Ru and of Ru-Cr alloy at different temperatures.

### Thermal Properties

Characteristic data of thermal expansion and thermal conductivity are given in Tables 14.98 and 14.151. Figure 14.84 shows the vapor pressure data for Ru.

### Optical Properties

The optical reflectivity of Ru is near that of Rh (Fig. 14.2). Ruthenium alloyed to Pd enhances the optical reflectivity by 4–5% (Fig. 14.86).

### Diffusion

Table 14.102 gives some values for self diffusion of Ru.

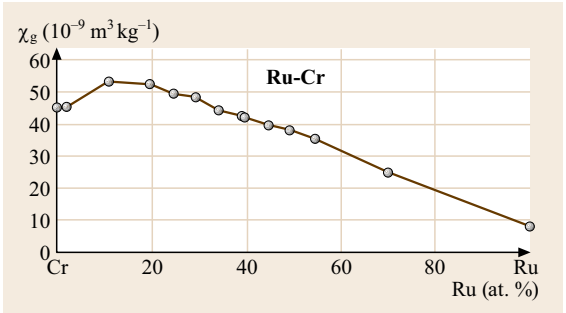


**Fig. 14.146** Temperature dependence of the mass susceptibility $\chi_g$ of Ru/Cr alloy (after [14.2])

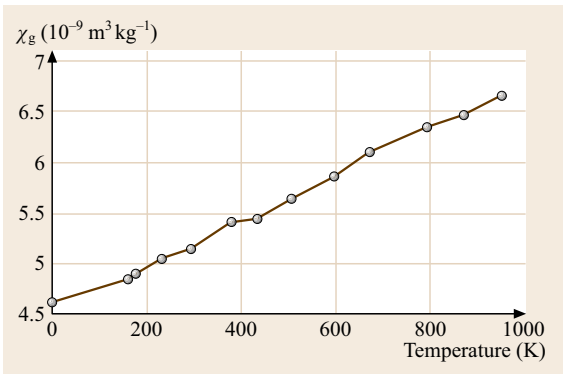


**Fig. 14.147** Temperature dependence of the mass susceptibility $\chi_g$ of Ru (after [14.2])

**Table 14.151** Thermal expansion coefficients of Ru and Os at different temperatures (after [14.2])

| Temperature (°C) | $\alpha$ ($10^{-6}$ K$^{-1}$) | | | | | |
|---|---|---|---|---|---|---|
| | Ru[a] | Ru[b] | Ru[c] | Os[a] | Os[b] | Os[c] |
| 323 | 5.9 | 8.8 | 6.9 | 4.0 | 5.8 | 4.8 |
| 423 | 6.1 | 9.3 | 7.2 | 4.3 | 6.2 | 5.0 |
| 623 | 6.8 | 10.5 | 8.0 | 4.0 | 7.1 | 5.7 |
| 723 | 7.2 | 11.0 | 8.4 | 5.3 | 7.6 | 6.2 |
| 823 | 7.6 | 11.7 | 8.8 | 5.8 | 8.3 | 6.9 |

[a] Vertical to the crystal $c$ axis, [b] Parallel to the crystal $c$ axis, [c] Polycrystalline

### Chemical Properties

Ruthenium is not attacked by acids or alkali even under oxidizing conditions (aqua regia). By heating in air above 800 °C Ru forms the oxides RuO and $RuO_2$;

**Table 14.150** Thermal electromotive force of Ru at different temperatures (after [14.2])

| $T$ (°C) | +100 | +200 | +300 | +500 | +800 | +1000 | +1200 |
|---|---|---|---|---|---|---|---|
| $E_{Ru/Pt}$ (mV) | 0.684 | 1.600 | 2.673 | 5.119 | 9.519 | 13.003 | 16.864 |

**Table 14.152** Thermodynamic data of Os (after [14.2])

| $T$ (K) | $c_p$ (J/(K mol)) | $S$ (J/(K mol)) | $H$ (J/mol) | $G$ (J/mol) | $p$ (at) |
|---|---|---|---|---|---|
| 298.15 | 24.707 | 32.635 | 0 | −9.73 | |
| 400 | 25.094 | 39.95 | 2.536 | −13.444 | $2.95\times10^{-95}$ |
| 800 | 26.618 | 57.811 | 12.879 | −33.371 | $6.31\times10^{-44}$ |
| 1400 | 28.903 | 73.287 | 29.535 | −73.067 | $5.81\times10^{-22}$ |

$T$ = temperature, $c_p$ = specific heat capacity, $S$ = entropy, $H$ = enthalpy, $G$ = free enthalpy, $p$ = partial pressure of the pure elements

above 1100 °C Ru forms $RuO_3$ which vaporizes. Detailed survey about the chemical properties is given in [14.3].

Complex organic Ru compounds are catalysts for the enantioselective hydrogenation of unsaturated carboxylic acids, used in pharmaceutical, agrochemical, flavors and fine chemicals (Fig. 14.148) [14.69].

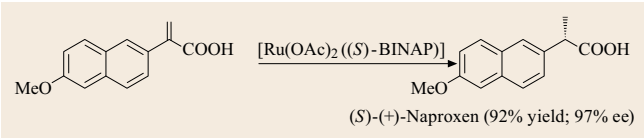


**Fig. 14.148** Synthesis of (*S*)-(+)-naproxen catalysed by Ru-cplx compound (after [14.11])

## 14.3.6 Osmium and Osmium Alloys

Osmium is used as a component in hard, wear- and corrosion-resistant alloys, as surface coatings of W-based filaments of electric bulbs, cathodes of electron tubes, and thermo-ionic sources. Osmium itself, Os alloys, and Os compounds are strong and selective oxidation catalysts. Commercial grades available are powder in 99.6% and 99.95% purity, $OsO_4$, and chemical compounds.

### Production

The production of Os starts from the mineral osmiridium via soluble compounds and the reduction to metal powder followed by powder-metallurgical compacting.

### Phases and Phase Equilibria

Selected phase diagrams are shown in Figs. 14.149–14.152 [14.1]. Continuous series of solid solution are formed with Re and Ru. Miscibility gaps exist with Ir, Pd, and Pt. The solid solubility in the Os-W system are 48.5 at.% for W and ≈ 5 at.% for Os. Osmium alloyed to Fe lowers the $\gamma \rightarrow \alpha$ transition temperature considerably (Fig. 14.153 [14.2]). Thermodynamic data are given in Table 14.152 [14.1] and molar heat capacities in Table 14.75. Table 14.153 gives structures and lattice parameters of intermediate compounds with Ir, Ru, Pt, and W [14.1].

### Mechanical Properties

Osmium is very hard and brittle. The hardness is, as in the case of Ru, strongly anisotropic. Characterisitic properties for hardness of the element at different temperatures, as well as work hardening and hardness of Os-Pt alloys are given in Tables 14.154 and 14.155 [14.1, 2] and Fig. 14.75. Osmium exhibits

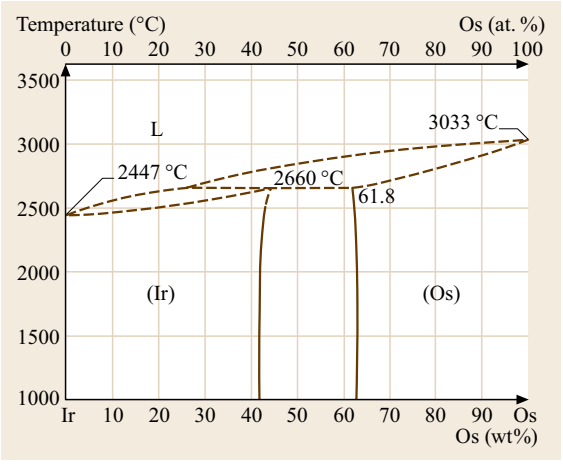


**Fig. 14.149** Phase diagram of Os-Ir (after [14.2])

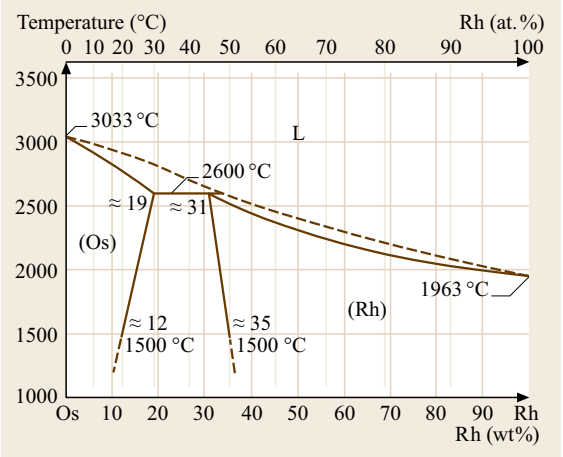


**Fig. 14.150** Phase diagram of Os-Rh (after [14.2])

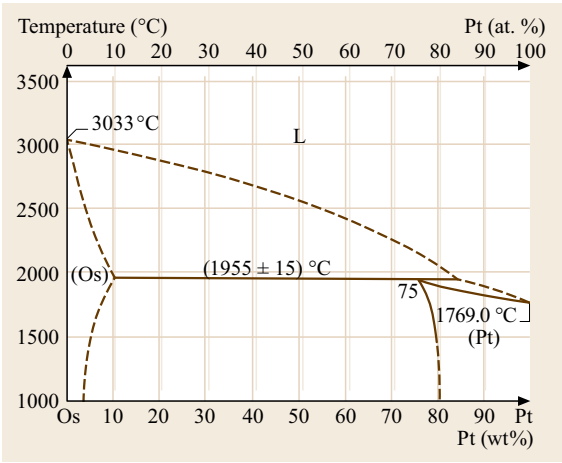


**Fig. 14.151** Phase diagram of Os-Pt (after [14.2])

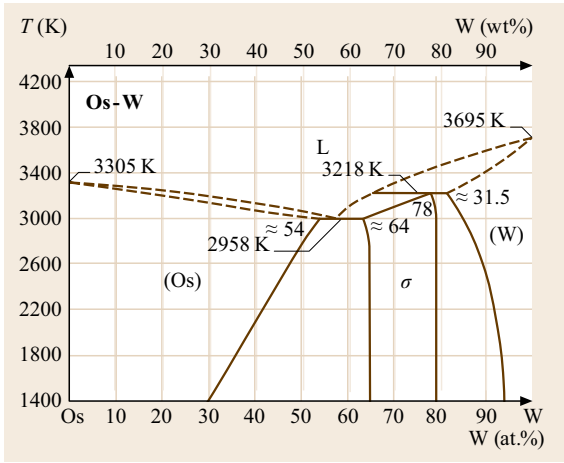


**Fig. 14.152** Phase diagram of Os-W (after [14.4])

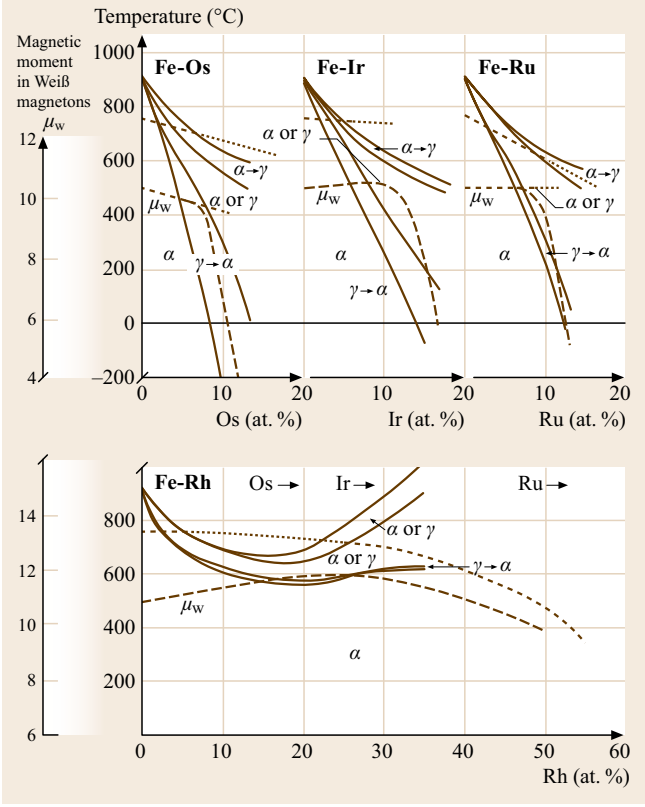


**Fig. 14.153** Temperature dependence of atomic moments, $\gamma \rightarrow \alpha$ transition and magnetic transition of iron alloys (after [14.5])

a Young's modulus of 570 GPa, a modulus of rigidity of 220 GPa, and the Poisson's ratio is 0.25.

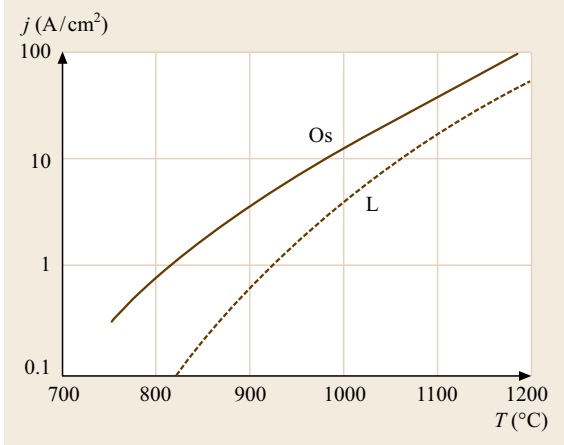


**Fig. 14.154** Current density $j$ as a function of cathodic temperature for a normal cathode (*dashed curve*) and a cathode with a 5 µm thick Os coating

### Electrical Properties

The residual electrical resistivity ratio (273.2 K/4.2 K) is 400 [14.1] (Table 14.89). Table 14.156 [14.1] gives the specific electrical resistivity of Os at different temperatures. The increase of atomic resistivity is shown in Table 14.148. Osmium coatings on W-based dispenser cathodes lower its work function (source Ba – Ca aluminate). It enhances the secondary electron emission (Fig. 14.154) and enables the operation at higher current densities in high power klystron and magnetron valves. Osmium shows superconductivity below 0.71 K and Table 14.157 gives some examples of superconducting Os alloys [14.3].

**Table 14.153** Structure and lattice parameter of selected Os alloy phases (after [14.2])

| Phase | Pearson symbol | $a$ (nm) | $c$ (nm) | Remarks | Concentration $x$ $A_{1-x}B_x$ |
|---|---|---|---|---|---|
| Os | *hP*2 | 0.27353 | 0.43191 | 293 K | |
| Os-Ir | *hP*2 | 0.27361 | 0.43417 | | 0.35 |
| Os-Ir | *cF*4 | 0.38358 | | | 0.8 |
| Os-Pt | *hP*2 | 0.27361 | 0.43247 | | 0.1 |
| Os-Pt | *cF*4 | 0.39094 | | | 0.8 |
| Os-Ru | *hP*2 | 0.27193 | 0.4394 | | 0.5 |
| $Os_3W_7$ | *tP*30 | 0.9650 | 0.4990 | | 0.78 |

**Table 14.154** Hardness of Os at different temperatures (after [14.1])

| $T$ (°C) | HV[a] |
|---|---|
| 20 | 300–680 |
| 200 | 260–580 |
| 600 | 200–410 |
| 1200 | 130–400 |

[a] All values depending on crystal orientation

**Table 14.155** Hardness of Os-Pt alloys (after [14.2])

| Pt content (wt%) | HV |
|---|---|
| 0 | 560 |
| 20 | 578 |
| 40 | 555 |

**Table 14.156** Specific electrical resistivity $\rho_i(T)$ of Os at different temperatures ($\rho(T) = \rho_0 + \rho_i(T)$) (after [14.1])

| $T$ (K) | $\rho_i$ (μΩ cm) |
|---|---|
| 25 | 0.012 |
| 100 | 1.90 |
| 273 | 8.30 |
| 900 | 26.0 |
| 1300 | 38.0 |

$\rho_0 = 0.09\,\mu\Omega$ cm at $T < 273$ K; $\rho_0 = 0.8\,\mu\Omega$ cm at $T > 273$ K

### Thermoelectric Properties

Figure 14.80 shows a comparison of the thermoelectric power of the different noble metals of the platinum group as a function of temperature.

### Magnetic Properties

Figures 14.82 and 14.155–14.157 [14.1] give a survey and present selected data of the magnetic mass susceptibility for the element and for Os-Cr alloys.

**Table 14.157** Superconducting Os-alloys (after [14.3])

| Alloy | $T_c$ (K) |
|---|---|
| Ce3Os4Ge13 | 6.1 |
| Pr3Os4Ge13 | 16 |
| Nd3Os4Ge13 | 1.9 |
| Eu3Os4Ge13 | 10.1 |
| Tb3Os4Ge13 | 14.1 |
| Dy3Os4Ge13 | 2.1 |
| Er3Os4Ge13 | 1.9 |
| ZrOsAs | 8 |
| HfOsAs | 3.2 |
| Y3Os4Ge13 | 3.9–3.7 |
| Lu3Os4Ge13 | 3.6–3.1 |
| Y5Os4Ge10 | 8.68–8.41 |
| TiOsP | < 1.2 |
| ZrOsP | 7.44–7.1 |
| HfOsP | 6.10–4.96 |

This alloy system exhibits antiferromagnetism in compositions from 0.3 to 2.2 at.% Os in the temperature range on the left-hand side of the bold vertical bars in Fig. 14.157. In Fe-Os alloys the temperature of the magnetic transition and the atomic magnetic moment decrease with increasing Os content (Fig. 14.153).

### Thermal Properties

Data for the thermal expansion coefficient at different temperatures are given in Table 14.151.

### Chemical Properties

Osmium is resistant against HCl but is attacked by $HNO_3$ and aqua regia. The element oxidizes in powder form readily at room temperature, forming $OsO_4$ which vaporizes above 130 °C. A detailed survey about chemical properties is given in [14.1]. The oxide $OsO_4$ serves as a catalyst for the synthesis of asymmetric organic compounds. Figure 14.158 shows an example for a ligand-supported chiral dihydroxylation [14.11].

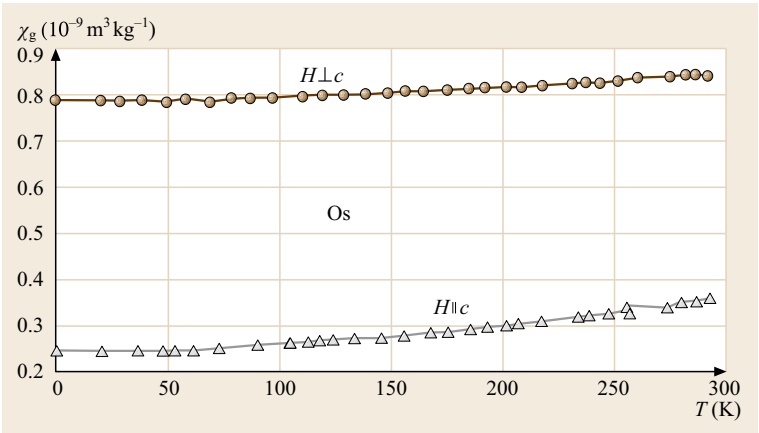


**Fig. 14.155** Temperature dependence of the mass susceptibility $\chi_g$ of Os single crystal at applied magnetic field of 795−700 A/m (after [14.2])

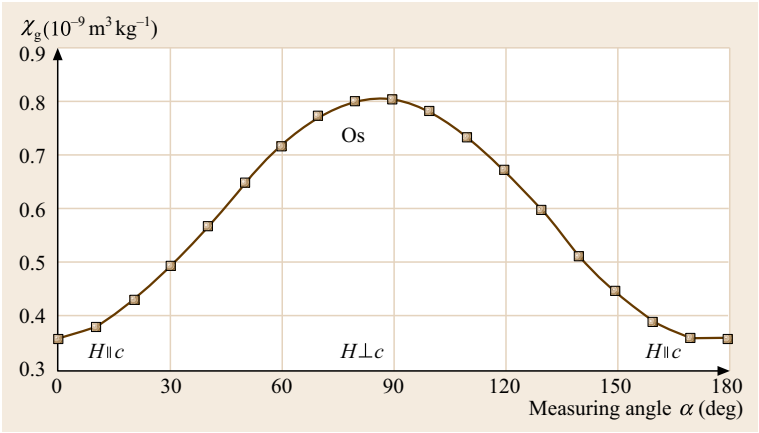


**Fig. 14.156** Mass susceptibility $\chi_g$ of an Os single crystal at room temperature as a function of measuring angle $\alpha$ (after [14.2])

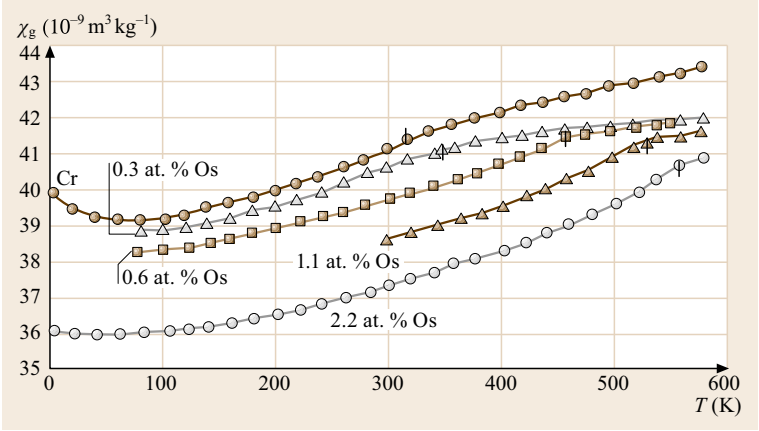


**Fig. 14.157** Temperature dependence of the mass susceptibilty $\chi_g$ of Os-Cr alloys. *Small marks* indicate the Neel temperature $T_N$ (after [14.2])

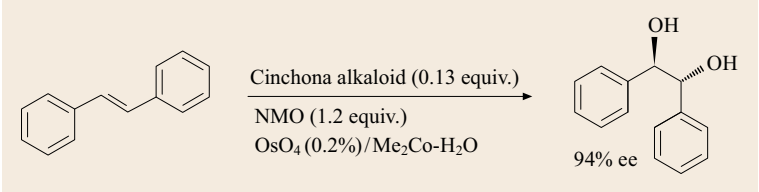


**Fig. 14.158** Chiral dihydroxylation using $OsO_4$ as catalyst component (after [14.69])

## References


14.1 A.G. Degussa: *Edelmetall-Taschenbuch* (Degussa, Frankfurt 1967)
14.2 A.G. Degussa: *Edelmetall-Taschenbuch*, 2nd edn. (Hüthig, Heidelberg 1995)
14.3 L.S. Benner, T. Suzuki, K. Meguro, S. Tanaka (Eds.): *Precious Metals, Science, Technology* (International Precious Metals Institute, Allentown 1991)
14.4 B. Predel (ed.): *Phase Equilibria, Crystallographic, Thermodynamic Data of Binary Alloys*, Landolt–Börnstein, New Series, Vol. IV/5 (Springer, Berlin, Heidelberg 1991–1998)
14.5 E. Raub: *Die Edelmetalle und ihre Legierungen* (Springer, Berlin, Heidelberg 1940)
14.6 P.J. Spencer, K. Hack: The solution of materials problems using the thermochemical databank system THERDAS, Swiss Mater. **2**, 69–73 (1990)
14.7 C.J. Smithells, E.A. Brandes: *Metals Reference Book*, 5th edn. (Butterworth, London 1977)
14.8 P. Villars, L.D. Calvert: *Pearson's Handbook of Crystallographic Data for Intermetallic Phases, Vols. 2 & 3* (American Society for Metals, Metals Park 1985)
14.9 Landolt–Börnstein: *Technik*, Landolt–Börnstein, New Series, Vol. IV/4, 6th edn. (Springer, Berlin, Heidelberg 1967)
14.10 W. Hume-Rothery, G.V. Raynor: *The Structure of Metals and Alloys* (Institute of Metals, London 1956)
14.11 *Gmelin Handbuch der Anorganischen Chemie*, Vol. 61 (Springer, Berlin, Heidelberg 1970–1975)
14.12 V. Behrens, K.H. Schröder: *Werkstoffe für elektrische Kontakte und ihre Anwendungen*, Kontakt und Studium, Vol. 366 (Expert, Ehningen 1992)
14.13 W.H. Cubberly, H. Baker, D. Benjamin (Eds.): *Metals Handbook*, Vol. 2, 9th edn. (American Society for Metals, Metals Park 1979) pp. 671–678
14.14 E.M. Savitskii, A. Prince: *Handbook of Precious Metals* (Hemisphere, New York 1989) pp. 117–128
14.15 K.-H. Hellwege, A.M. Hellwege (Eds.): *Elastics, Piezolelectric, Pyroelectric, Electrooptic Constants, Nonlinear Dielectric Susceptibilities of Crystals*, Landolt–Börnstein, New Series, Vol. III/18 (Springer, Berlin, Heidelberg 1984) p. 66
14.16 Doduco: *Datenbuch, Handbuch für Techniker*, 2nd edn. (Doduco, Pforzheim 1977)
14.17 H. Spengler: Metall **18**, 36 (1964)
14.18 K.-H. Hellwege, J.L. Olsen: *Metals – Electronic Transport Phenomena*, Landolt–Börnstein, New Series, Vol. III/15 (Springer, Berlin, Heidelberg 1982) p. 167
14.19 D.D. Pollok: Trans. Metall. Soc. AIME **230**, 753 (1964)
14.20 H. Flükiger, W. Klose (Eds.): *Superconductors Ac–Na*, Landolt–Börnstein, New Series, Vol. III/21 (Springer, Berlin, Heidelberg 1990)
14.21 C. Raub: Z. Metallkd. **55**, 195 (1964)
14.22 R.E. Hummel: *Optische Eigenschaften von Metallen und Legierungen* (Springer, Berlin, Heidelberg 1971) pp. 158–178
14.23 H. Mehrer (Ed.): *Diffusion in Solid Metals and Alloys*, Landolt–Börnstein, New Series, Vol. III/26 (Springer, Berlin, Heidelberg 1990)
14.24 G. Schlamp: Mater. Sci. Technol. **8**, 471–587 (1996)
14.25 D. Lee: In: *Modern Chlor-Alkali Technology*, Vol. 2, ed. by C. Jackson (Horwood, Chichester 1983)
14.26 S.U. Falk, A.J. Salkind: *Alkaline Storage Batteries* (Wiley, New York 1971)
14.27 A. Fleischer, J.J. Lander: *Zinc-Silver-Oxide Batteries* (Wiley, New York 1971)
14.28 H. Renner: *Ullmann's Encyclopedia of Industrial Chemistry* (Wiley-VCH, Weinheim 2002)
14.29 D.Z. Stöckel: Composites for electrical contact applications, Z. Werkstofftech. **10**, 238 (1979)
14.30 H. Renner: *Ullmann's Encyclopedia of Industrial Chemistry*, 6th edn. (Wiley-VCH, Weinheim 2001)
14.31 R. Ferro, A. Saccone, D. Macciò, S. Delfino: A survey of gold intermetallic chemistry, Gold Bull. **36**(2), 39–58 (2003)
14.32 N. Yuantao: Alloying and strengthening of gold via rare earth metal additions, Gold Bull. **34**(3), 77–87 (2001)
14.33 H. Ahlborn, G. Wassermann: Z. Metallkd. **55**, 685 (1964)
14.34 E. Drost, J.H. Hausselt: Uses of gold in jewellery, Interdisc. Sci. Rev. **17**, 271–280 (1992)
14.35 B. Kempf, J. Hausselt: Gold, its alloys and their uses in dentistry, Interdisc. Sci. Rev. **17**, 251–260 (1992)
14.36 G. Humpston, D.M. Jacobson, S.P.S. Sangha: Diffusion soldering. A new low temperature process for joining carat gold jewellery, Gold Bull. **26**, 90 (1993)
14.37 C.J. Raub, D. Ott: Z. Metallkd. **25**(4), 629 (1992)
14.38 M. Du Toit, E. van der Lingen, L. Glaner, R. Süss: The development of a novel gold alloy with 995 fineness and increased hardness, Gold Bull. **35**, 49 (2002)
14.39 *Gmelin Handbuch der Anorganischen Chemie*, Vol. 62 (Springer, Berlin, Heidelberg 1996) p. 619
14.40 H.R. Khan, C.R. Raub: The superconductivity of gold alloys, Gold Bull. **8**, 114–118 (1975)
14.41 H.R. Khan: Superconducting gold alloys, Gold Bull. **17**, 94–100 (1984)
14.42 J. Kopp: Low temperature resistivity and thermopower anomalies in pure gold, Gold Bull. **9**, 55–57 (1976)
14.43 A.S. Darling: Electron concentration as a guide to alloying behaviour, Platin. Met. Rev. **13**, 53 (1969)
14.44 M. Hansen, K. Anderko: *Constitution of Binary Alloys*, 2nd edn. (McGraw-Hill, New York 1958), pp. 195, 221
14.45 E. Raub: *Die Edelmetalle und ihre Legierungen, Reine angewandte Metallkunde*, Vol. 5 (Springer, Berlin, Heidelberg 1955), pp. 53, 54, ed. by W. Köster
14.46 T. Shiraishi, K. Hisatsune, Y. Tanaka, E. Miura, Y. Takuma: Optical properties of Au-Pt and Au-Pt-In alloys, Gold Bull. **34**, 129–133 (2001)
14.47 W.S. Rapson, T. Groenewald: *Gold Usage* (Academic Press, New York 1978) p. 37
14.48 D. Compton, L. Cornish, E. van der Lingen: The third order nonlinear optical properties of gold nanoparticles in glasses, Part II, Gold Bull. **36**, 51–58

(2003)
14.49 G.C. Bond: Gold: A relatively new catalyst, Gold Bull. **34**, 117–119 (2001)
14.50 A.S.K. Hashmi: Homogeneous gold catalysts and alkynes: A successful liaison, Gold Bull. **36**, 3 (2003)
14.51 M. Gupta, A.K. Tripathi: The role of nanosized gold particles in adsorption and oxidation of carbon monoxide over $Au/Fe_2O_3$ catalyst, Gold Bull. **34**, 120–128 (2001)
14.52 C. Corti, R.J. Holliday, D.T. Thompson: Developing new industrial applications for gold: Gold nanotechnology, Gold Bull. **35**, 111–117 (2002)
14.53 R. Grisel, K.J. Weststrate, A. Gluhoi, B.E. Nieuwenhuys: Catalysis by gold nanoparticles, Gold Bull. **35**, 39–45 (2002)
14.54 H. Knosp, R.J. Holliday, C.W. Corti: Gold in dentistry: Alloys, uses and performance, Gold Bull. **36**, 93–102 (2003)
14.55 D.R. Olsen, H.M. Berg: Properties of die bond alloys relating to thermal fatigue. In: *Proc. 27th Electron. Compon. Conf* (IEEE, Piscataway 1977) p. 193
14.56 G. Petzow, G. Effenberg: *Ternary Alloys* (Verlag Chemie, Weinheim 1988)
14.57 W. Müller: *Metallische Lotwerkstoffe* (DVS, Düsseldorf 1990)
14.58 A.S. Darling: The search for alternatives to rhodium–platinum alloys, Platin. Metal. Rev. **17**(4), 130–136 (1973)
14.59 J.B. Hunter: A new hydrogen purification process, Platin. Met. Rev. **4**(4), 130 (1960)
14.60 A.G. Knapton: Palladium alloys for hydrogen diffusion membranes, Platin. Met. Rev. **21**(2), 44 (1977)
14.61 R.S. Irani: Ordering in platinum group metal alloys, Platin. Met. Rev. **17**(1), 21–25 (1973)
14.62 A. Kussmann, G. Gräfin von Rittberg: Über magnetische Eigenschaften von Platin–Eisen-Legierungen. II, Ann. Phys. **442**(3/4), 173–181 (1950)
14.63 A.S. Darling: Electron configuration and crystal structure of platinum metal alloys, Platin. Met. Rev. **11**, 138–140 (1967)
14.64 R.S. Irani, R.W. Cahn: Copper-platinum alloys, Platin. Met. Rev. **16**, 48–49 (1972)
14.65 H. Ocken, J.H.N. Van Vucht: Phase equilibria and superconductivity in the molybdenum-platinum system, J. Less-Common Met. **15**(2), 196–199 (1968)
14.66 I. Gurrappa: Platinum aluminide coatings for oxidation resistance of titanium alloys, Platin. Met. Rev. **45**(3), 124 (2001)
14.67 I.M. Wolff, P.J. Hill: Platinum metals-based intermetallics for high-temperature service, Platin. Met. Rev. **44**(4), 158–166 (2000)
14.68 J. Merker, D. Lupton, M. Töpfer, H. Knake: High temperature mechanical properties of the platinum group metals, Platin. Met. Rev. **45**, 74–82 (2001)
14.69 T.J. Colacot: 2001 Nobel Prize in Chemistry, Platin. Met. Rev. **46**(2), 82–83 (2002)
14.70 Y. Yamabe-Mitarai, Y.F. Gu, H. Harada: Two-phase iridium-based refractory superalloys, Platin. Met. Rev. **46**(2), 74–81 (2002)
14.71 J.H. Jones: The Cativa™ process for the manufacture of acetic acid, Platin. Met. Rev. **44**(3), 94–105 (2000)